

SYSTEM AND MATERIAL ASPECTS OF VOLUMETRIC
BIT-WISE OPTICAL DATA STORAGE

by

Yan Zhang

A Dissertation Submitted to the Faculty of the
COMMITTEE ON OPTICAL SCIENCE (GRADUATE)

In Partial Fulfillment of the Requirments
For the Degree of

DOCTOR OF PHILOSOPHY

In the Graduate College

THE UNIVERSITY OF ARIZONA

2004

UMI Number: 3132280

INFORMATION TO USERS

The quality of this reproduction is dependent upon the quality of the copy submitted. Broken or indistinct print, colored or poor quality illustrations and photographs, print bleed-through, substandard margins, and improper alignment can adversely affect reproduction.

In the unlikely event that the author did not send a complete manuscript and there are missing pages, these will be noted. Also, if unauthorized copyright material had to be removed, a note will indicate the deletion.

UMI[®]

UMI Microform 3132280

Copyright 2004 by ProQuest Information and Learning Company.

All rights reserved. This microform edition is protected against unauthorized copying under Title 17, United States Code.

ProQuest Information and Learning Company
300 North Zeeb Road
P.O. Box 1346
Ann Arbor, MI 48106-1346

THE UNIVERSITY OF ARIZONA ©
GRADUATE COLLEGE

As members of the Final Examination Committee, we certify that we have read the dissertation prepared by Yan Zhang

entitled System and Material Aspects of Volumetric

Bit-wise Optical Data Storage

and recommend that it be accepted as fulfilling the dissertation requirement for the Degree of Doctor of Philosophy

Thomas D. Milster
Thomas D. Milster

3/24/04
Date

Alan R. Kost
Alan R. Kost

3/24/04
Date

Dror Sarid
Dror Sarid

3/24/04
Date

Date

Date

Final approval and acceptance of this dissertation is contingent upon the candidate's submission of the final copy of the dissertation to the Graduate College.

I hereby certify that I have read this dissertation prepared under my direction and recommend that it be accepted as fulfilling the dissertation requirement.

Thomas D. Milster
Dissertation Director, Thomas D. Milster

3/24/04
Date

STATEMENT BY AUTHOR

This dissertation has been submitted in partial fulfillment of the requirements for an advanced degree at The University of Arizona and is deposited in the University Library to be made available to borrowers under rules of the Library

Brief quotations from this dissertation are allowable without special permission, provided that accurate acknowledgement of source is made. Request for permission for extended quotation from or reproduction of this manuscript in whole or in part may be granted by the head of the major department or the Dean of the Graduate College when in his or her judgment the proposed use of the material is in the interests of scholarships. In all other instances, however, permission must be obtained from the author.

SIGNED: 

ACKNOWLEDGEMENTS

I would like to express my heartily gratitude for Professor Tom Milster for his patience to instruct me on this research. He is not only a research adviser but also a true educator to me. Under his guidance, I built up my confidence and found my true interest. The gratitude is also given to our group member Sanki Park, Joshua Joe, and Dr. Kim for their ideas and advice. Special thanks to John Butz, Warren Bletscher, and Kevin Erwin for their professional supports in the mechanical and electronic design. In the last, I want to thank all my friends in Tucson, Arizona during all these years. Without you, my life would be much harder in this desert!

DEDICATION

This dissertation is dedicated to my father, my mother, and my sister,
for their constant love and faith on me.

TABLE OF CONTENTS

LIST OF ILLUSTRATIONS.....	8
LIST OF TABLES.....	13
ABSTRACT.....	15
1. INTRODUCTION.....	16
1.1 Basic Description of the optical data storage technology.....	16
1.2 Introduction to the SIL, volumetric storage optics and volumetric Storage media.....	20
1.3 Motivation for this study.....	22
1.4 Outline of dissertation.....	23
2.BACKGROUND.....	25
2.1 History of holographic volumetric data storage.....	25
2.2 History of bit-wise volumetric optical data storage.....	26
2.2.1 Refractive-index-change material.....	27
2.2.2 Fluorescent material.....	30
2.2.3 Super-Rens material.....	35
3. INTER-LAYER CROSSTALK	38
3.1 Introduction to inter-layer crosstalk and three simulation methods.....	38
3.2 Simulation of inter-layer crosstalk for an optical system using fluorescent material.....	41
3.2.1 Simulation using 3D OTF.....	45
3.2.2 Simulation using OPTISCAN.....	57
3.2.3 Comparing simulation results	63
3.3 Simulation of inter-layer crosstalk in an optical system using Super-Rens material.....	64
3.4 Summary.....	67
4. LENS DESIGN.....	68
4.1 Far-field system with proper spherical aberration compensator.....	68
4.2 Near-field system with proper spherical aberration compensator.....	74
4.3 Far-field system versus Near-field system.....	84
4.4 Summary.....	84

TABLE OF CONTENTS-*Continued*

5. EFFECTIVE SURFACE DENSITY	86
5.1 Maximum storage density of a far-field system.....	86
5.2 Maximum storage density of a near-field system.....	88
5.3 Summary of effective surface density calculations for media with low absorption.....	92
5.4 Effective surface density for media with significant absorption.....	95
5.5 Summary.....	98
6. DYNAMIC TEST STAND FOR FLUORESCENT MATERIAL (ARTS-1).....	99
6.1 Test stand description.....	99
6.2 Introduction to space environment.....	103
6.3 Test results of the fluorescent medium under temperature cycles.....	103
6.4 Test results of the fluorescent medium under heavy ion radiation.....	109
6.5 Test results of the fluorescent medium under proton radiation.....	111
6.6 Summary.....	113
7. DYNAMIC TEST STAND FOR SUPER-RENS MATERIAL (ARTS-2).....	114
7.1 Test stand description.....	114
7.2 Experiment results.....	120
7.3 Summary.....	122
8. CONCLUSIONS, SUMMARY AND FUTURE WORK.....	124
8.1 Summary.....	124
8.2 Future work.....	126
9. REFERENCES.....	128

LIST OF ILLUSTRATIONS

Figure 1.1 The process of recording data onto an optical disk starts with the user input data stream converted to a current drive signal for the laser diode. Intense pulses from the laser cause physical changes in the surface of the recording medium as the disk spins, which result in spiral tracks of data marks.	18
Figure 1.2 A constant, low power laser beam scans a data track to readout data from the disk. Reflected light is modulated by the data-mark pattern. The reflected light is directed to servo and data detectors with a beam splitter, which convert the light modulation in a current signal that is then decoded.	19
Figure 1.3 A typical near-field system using SIL.	20
Figure 1.4 A schematic drawing of the volumetric bit-wise optical data storage system.	24
Figure 2.1 A sandwiched structure for refractive-index-change material.	29
Figure 2.2 A physical description of two-photon absorption. (a) Energy-level diagram and molecular structure of unwritten and written forms, showing fluorescence (b) absorption spectra and fluorescence spectrum of the unwritten and written forms of the material.	32
Figure 2.3 A two-fluorescent-spots servo technique for the fluorescent material.	33
Figure 2.4 A schematic drawing of the optical system using master slave servo technique.	35
Figure 2.5 The concept of Super-Rens structure.	36
Figure 3.1 The crosstalk ratio $20 \log_{10} (I_B/I_A)$ is measured via a two-step process. (a) The readout signal modulation from scanning layer 1 is measured (I_A); (b) The readout signal modulation from scanning layer 2 is measured (I_B).	39
Figure 3.2 Illustration of Yee cells used in the FDTD method.	42
Figure 3.3 A far-field system used in the crosstalk study.	43

LIST OF ILLUSTRATIONS-*Continued*

Figure 3.4 The coordinate system used in the simulation.	44
Figure 3.5 Calculation of $OTF1(f_x, f_y, f_z)$	50
Figure 3.6 Profiles of 3D OTF of a confocal system and a non-confocal system in the f_z axis. The dashed line represents the confocal system. The solid line represents the non-confocal system.	53
Figure 3.7 The data mark pattern used in the inter-layer crosstalk simulation.	54
Figure 3.8 A data mark is decomposed into N layers.	58
Figure 3.9 Illustration of step 3 for calculating the readout signal from fluorescent marks with OPTISCAN.	59
Figure 3.10 Contours of inter-layer crosstalk level X versus ΔL and Δb from Fig. 3.7 for (a) non-confocal systems and (b) confocal systems. The shaded area is the acceptable region of operation based on a -30 dB crosstalk criterion. The confocal system has the largest acceptable operating region.	60
Figure 3.11 Simulation results from OPTISCAN when $Tz=4.4 \mu\text{m}$. The solid line is CNR versus ν_d , the dashed line is inter-layer crosstalk versus ν_d . Black dots are simulation results from the 3D OTF model.	62
Figure 3.12 A near-field system used in the crosstalk study, which has a solid immersion lens (SIL) in proximity to the data layers. The radius of the SIL is 1.0 mm.	62
Figure 3.13 A single piece of thin film with Super-Rens structure.	64
Figure 3.14 (a) The data mark pattern used in inter-layer crosstalk study for a Super-Rens material. (b) A detailed view of the data mark.	66
Figure 4.1 A typical fluorescent volumetric read out system. The incident laser beam is focused by an objective lens onto a bit plane of interest at depth d_{layer} below the top surface. The distance between marks in the same bit plane is T_ξ , while the distance between two planes of data marks is T_z	69

LIST OF ILLUSTRATIONS-Continued

Figure 4.2 Layout of a far-field system designed for optimum compensation through volumetric media. The lens elements extend over a track length of only 13mm. d_{focus} is adjusted to change data layers, and d_{comp} is changed to adjust for spherical aberration.	71
Figure 4.3 The relations of d_{focus} and d_{comp} versus d_{layer} for far-field system.	73
Figure 4.4 Spherical aberration SA of a focused beam inside a SIL. A and B are aplanatic points. C and A are stable points versus focus . Point O corresponds to the objective lens reflecting from the SIL vertex. Point A is the hemi-spherical condition, and point B is the hyper-spherical aplanatic condition.	75
Figure 4.5 Layout of Near-Field System I.	76
Figure 4.6 Layout of Near-Field System II.	77
Figure 4.7 Layout of Near-Field System III.	78
Figure 4.8 The spherical aberration compensation range for Near-Field System I, Near-Field System II and Near-Field System III.	82
Figure 5.1 Effective surface density Π of a far-field read-out system versus medium refractive index when (a) $\lambda=0.633 \mu\text{m}$, $(\Delta W_{040})_{\text{max}} = 20$ waves; (b) $\lambda=0.633 \mu\text{m}$, $(\Delta W_{040})_{\text{max}} = 10$ waves; (c) $\lambda=0.633 \mu\text{m}$, $(\Delta W_{040})_{\text{max}} = 2$ waves; and (d) $\lambda=0.405 \mu\text{m}$, $(\Delta W_{040})_{\text{max}} = 20$ waves. At the design point, $\lambda=0.633 \mu\text{m}$, $NA=0.6$ and $(\Delta W_{040})_{\text{max}} = 36$ waves.	88
Figure 5.2 Contour map of Π of Near-field System I versus sine of the marginal ray angle $\sin\theta$ and medium refractive index n	90
Figure 5.3 Effective surface density Π of Near-field System II versus medium refractive index n when $\lambda=0.633 \mu\text{m}$ and $\lambda=0.405 \mu\text{m}$	91

LIST OF ILLUSTRATIONS-Continued

- Figure 5.4 Effective surface density Π of Near-Field System III (optimum near-field system) versus NA when (a) $\lambda=0.405 \mu\text{m}$, $n=1.5$; (b) $\lambda=0.405 \mu\text{m}$, $n=2.0$; (c) $\lambda=0.633 \mu\text{m}$, $n=1.5$; (d) $\lambda=0.633 \mu\text{m}$, $n=2.0$. In the simulation, $(\Delta W_{040}|_{c^-} - \Delta W_{040}|_c)/\lambda = -5.1$, $(\Delta W_{040}|_{c^+} - \Delta W_{040}|_c)/\lambda = -2.5$. Focus range is $(\Delta t_z)_{\text{max}} = |l_{c^+} - l_c| + |l_{c^-} - l_c|$. At the design point, $\lambda=0.633 \mu\text{m}$, $NA=1.2$ and $\Pi=470 \text{ Gb-in}^{-2}$93
- Figure 5.5 (a) N versus τ for both far-field system and near-field system at $\lambda=0.405 \mu\text{m}$; (b) Π versus τ for both far-field system and near-field system at $\lambda=0.405 \mu\text{m}$97
- Figure 6.1 The schematic description of the Arizona Readout Test Stand 1 (ARTS-1) dynamic test stand. The optical components are mounted on a semi-kinematic rail structure. A knife-edge prism is used to split the fluorescence and the difference between the two signals is used as a track error signal (TES).100
- Figure 6.2 The photo of ARTS-1.101
- Figure 6.3 The read out signal from ARTS displayed on a oscilloscope.102
- Figure 6.4 The read out signal from ARTS displayed on a spectrum analyzer. The resolution bandwidth is 3 kHz, the video bandwidth is 300 Hz and the CNR is 37 dB.102
- Figure 6.5 The vacuum oven used in the temperature cycle experiment.104
- Figure 6.6 (a) CCD image of fluorescent bits before heating. (b) CCD image of fluorescent bits after heating. No apparent change is observed compared to (a).106
- Figure 6.7 (a) Time domain readout signal before heating exhibits a straight baseline and large signal amplitude. (b) Time domain readout signal after heating exhibits a strongly curved baseline, without a significant reduction in signal amplitude.108

LIST OF ILLUSTRATIONS-*Continued*

Figure 6.8 (a) Ronchi test interferogram of the disk front surface before heating. Straight lines indicate a relatively flat surface. (b) Ronchi test interferogram of the disk surface after heating. Complex line patterns indicate a deformed surface.	109
Figure 7.1 Schematic layout of the test stand.	115
Figure 7.2 (a) Schematic diagram of the combination of the rotating head and the coupon sample. (b) Picture taken in the experiment about the rotating head and coupon sample mount.	116
Figure 7.3 Spot sizes on the detector vary at various focus position.	117
Figure 7.4 Data marks written on a coupon sample made from Super-Rens material at 1 m/s focus spot speed , 125 KHz data rate and 12 mW laser power.	122

LIST OF TABLES

Table 3.1 The inter-layer crosstalk X versus T_z for both confocal and non-confocal systems at $\Delta L = 0.45 \mu\text{m}$	55
Table 3.2. CNR versus v_d when the laser beam scans through data marks in layer 2 at $\Delta L = 0.45 \mu\text{m}$ and $T_z = 3.4 \mu\text{m}$	56
Table 4.1 Optical design parameters of the far-field system in Fig. 4.2 that operates at $\lambda=0.633 \mu\text{m}$ at $\Delta t_z = 4.1\text{mm}$	72
Table 4.2 Optical design parameters of Near-Field System I in Fig. 4.5 that operates at $\lambda=0.633 \mu\text{m}$	79
Table 4.3 Optical design parameters of Near-Field System II in Fig. 4.6 that operates at $\lambda=0.633 \mu\text{m}$	80
Table 4.4 Optical design parameters of Near-Field System III in Fig. 4.6 that operates at $\lambda=0.633 \mu\text{m}$	81
Table 4.5 Important parameters: NA, $(\Delta t_z)_{\text{max}}$, $(\Delta W_{040})_{\text{max}}/\lambda$, d_{focus} range, d_{comp} range and d_{layer} range for far-field system, Near-Field System I, Near-Field System II and Near-Field System III.	83
Table 5.1 Important parameters: NA, N , Π , and $(\Delta t_z)_{\text{max}}$ for far-field system, Near-Field System I, Near-Field System II and Near-Field System III at $\lambda = 0.633 \mu\text{m}$ under the assumption of low medium absorption.	94
Table 5.2 $(\Delta t_z)_{\text{max}}$ and effective surface density in closed form for the far-field system, Near-Field System I, Near-Field System II under the assumption of low media absorption. $(\Delta t_z)_{\text{max}}$ and effective surface density of the Near-Field System III can only be calculated numerically. $\gamma = 1.35$ for all calculations.	95
Table 6.1 The percentage of disks failed versus temperature and heating period.	105
Table 6.2 Test results of the photo-chromic disks after they are exposed to heavy ion radiation.	110

LIST OF TABLES-*Continued*

Table 6.3 Test results of the photo-chromic disks after they are exposed to proton radiation.	112
Table 6.4 Minimum thickness for shielding metal when the proton energy is 60 Mev.	113
Table 7.1 d_{comp} , d_{focus} and corresponding system Strehl ratio simulated by Zemax.	119
Table 7.2 Focus spot speed versus data rate versus P_{min} and I_{th} for Super-Rens material.	121

ABSTRACT

There are several primary factors that limit the data capacity of a volumetric bit-wise optical data storage system. Firstly, the data density in each layer is limited by the spot size formed at the focus of the objective lens. The spherical aberration induced by the medium also limits the maximum depth that an optical system can reach with diffraction limited focus. A second primary factor is the undesired detection of data from layers other than the layer at the laser focus, which is an effect called inter-layer crosstalk. In the last, the transmission and the reflection rate of the medium sets the limit of the number of the data layers for a given laser diode.

In the modeling, the inter-layer crosstalk of volumetric bit-wise storage systems is simulated by using three methods. Several far-field and near-field systems with spherical aberration compensators are presented. In addition, the maximum surface densities of these systems are discussed.

A dynamic test stand equipped with a tracking servo is built for testing the fluorescent material performance in a simulated space environment. Coupon samples made of Super-Rens material are tested in another dynamic test stand equipped with a focus servo. Controls of writing conditions for Super-Rens material are investigated with respect to the focus spot speed and data rate.

Overall, this dissertation provides a description of volumetric bit-wise optical data storage technology, in terms of the system and material aspects, through simulation and experiments.

Chapter 1

INTRODUCTION

With the rapid advancement of internet and computer technology, the demand of massive and inexpensive data storage tools has increased dramatically. For the last twenty years, optical disks, in particular read-only compact disks (CDs) and digital versatile disks (DVDs) have enabled us to replicate massive amount of data in an inexpensive removable format. Optical disks are also popular as recording devices in the formats of compact-disc-recordable (CD-R) and compact-disk-rewritable (CD-RW). Other formats, such as DVD-R and DVD-RW, are just emerging into the market of massive data storage. As the optical data storage technology evolves, the capacity of a optical disk increases [Tieke *et al.* 1999]. For example, the data capacity of a single-layer DVD (4.7 GB) is a factor of 7.3 more than that of a CD (0.64 GB). The CD and DVD devices use the mechanism of far-field single-layer recording. A more advanced technology, which uses multiple layers on a single disk, is called volumetric bit-wise optical data storage. This new technology is expected to extend the capacity of optical disks orders of magnitude beyond what is found in CD and DVD. This dissertation presents the characterization of optical systems that can be used for volumetric bit-wise optical data storage and experimental characterization of two kinds of material that are promising in this field.

1.1 Basic Description of the optical data storage technology

There are two primary aspects associated with optical data storage technology, which are storage of data and retrieval of data. The process for storing data marks on a recordable optical disk is shown in Fig. 1.1, where an input stream of digital information is converted with an encoder and modulator into a drive signal for a laser source. The laser source emits an intense light beam that is directed and focused onto the surface with illumination optics. As the surface moves under the scanning spot, energy from the intense scan spot is absorbed, and a small, localized region heats up. The surface, under the influence of heat beyond a critical writing threshold, changes its reflective properties. Modulation of the intense light beam is synchronous with the rotation, so a circular track of data marks is formed as the surface rotates. The scan spot is moved slightly as the surface rotates to allow another track to be written on new media during the next revolution. The size of the data mark is nearly the size of the focused laser spot. Due to the physics of diffraction, the spot size s cannot be made arbitrarily small. Instead, it is a function of the wavelength of the laser λ , the focusing properties of the objective lens, system aberrations and the thin-film structure used as the recording layer [Milster *et al.* 1999]. A simple relationship that is used to estimate the full-width-at $1/e^2$ spot size for conventional Gaussian illumination [Haskal 1979] is $s = \lambda/NA = \lambda/n \sin \theta$, where λ is the wavelength in the air, NA is the system's numerical aperture, n is the refractive index of the medium and θ is the marginal ray angle.

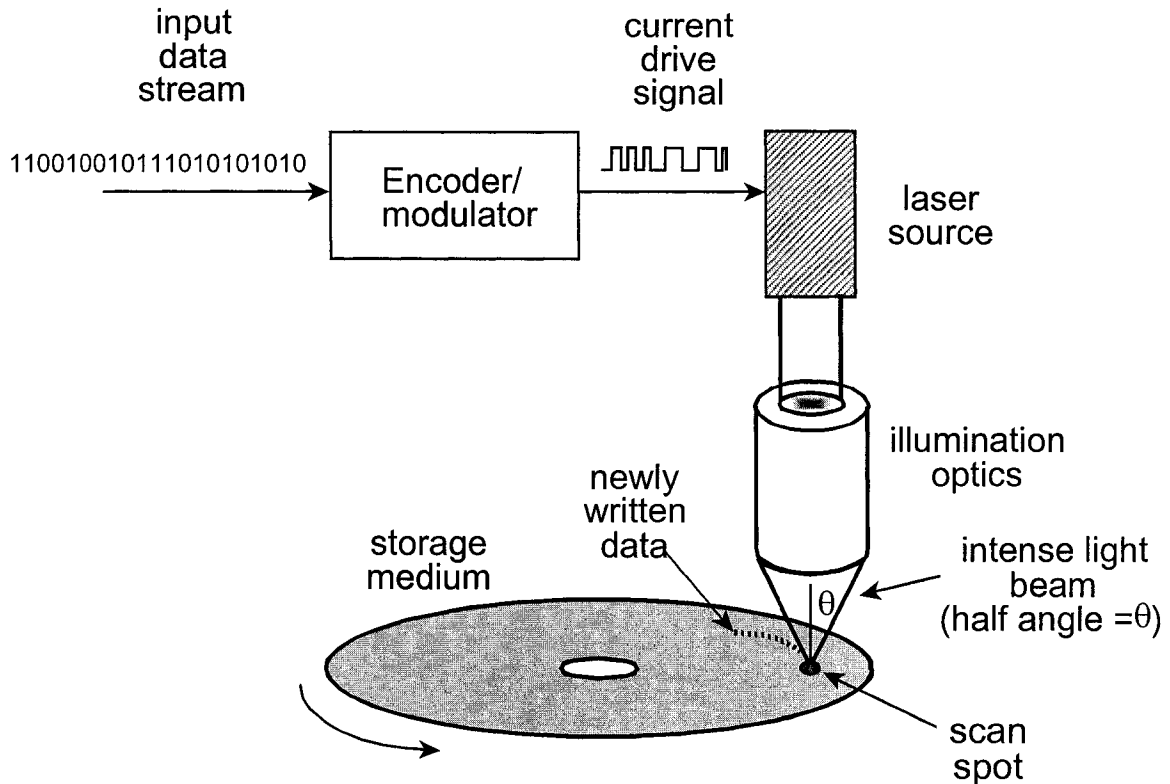


Figure 1.1 The process of recording data onto an optical disk starts with the user input data stream converted to a current drive signal for the laser diode. Intense pulses from the laser cause physical changes in the surface of the recording medium as the disk spins, which result in spiral tracks of data marks.

Retrieval of data marks on the disk is illustrated in Fig. 1.2, where the laser is used at a constant output power level that does not heat the data surface beyond its thermal writing threshold. The laser beam is directed through a beam splitter into the illumination optics, where the beam is focused onto the surface. As the data marks to be read pass under the scan spot, the reflected light is modulated. Modulated light is collected by illumination optics and directed by the beam splitter to servo and data optics,

which converge the light onto detectors. The detectors change light modulation into current modulation that is amplified and decoded to produce the output data stream.

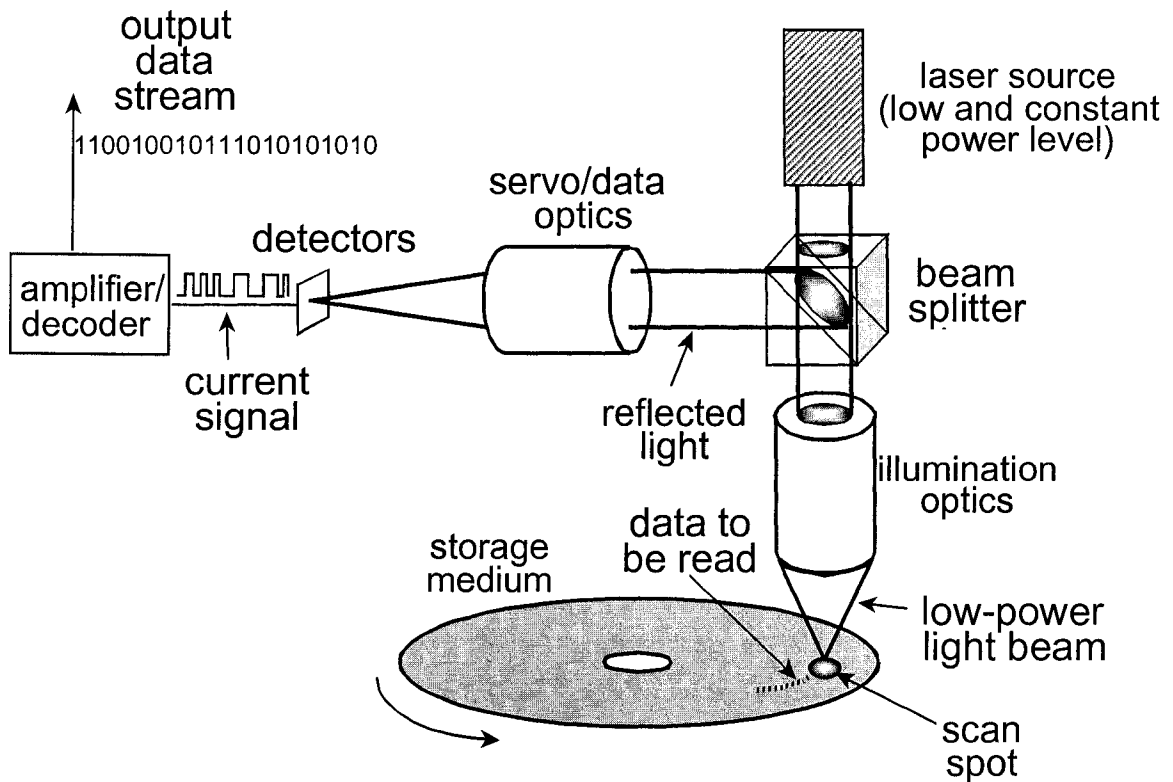


Figure 1.2 A constant, low power laser beam scans a data track to readout data from the disk. Reflected light is modulated by the data-mark pattern. The reflected light is directed to servo and data detectors with a beam splitter, which convert the light modulation in a current signal that is then decoded.

It is natural to conclude that the data capacity of an optical disk is proportional to $1/s^2$. Hence, to increase the data capacity, we can reduce λ , increase NA or simply introduce multiple layers of data marks. Multiple layers increase the data capacity by N , where N is the number of layers.

1.2 Introduction to the SIL, volumetric storage optics and volumetric storage media

The solid immersion lens (SIL) is currently being developed as a near-field data storage technique [Mizuno et al. 2001], which utilizes evanescent energy to greatly increase NA and produce extremely small optical spots. A typical arrangement for the SIL system is shown in Fig. 1.3. A SIL, which is an image-centric hemispherical lens with high refractive index, is placed in near contact with the recording medium. Light from a laser passes through the beam splitter and is focused near the bottom of the SIL by an objective lens. The size of the light spot is smaller than the laser wavelength. The evanescent field generated from the bottom of the SIL couples into the recording medium, which leads to a small data mark. Hence, the data capacity is greatly increased on each layer.

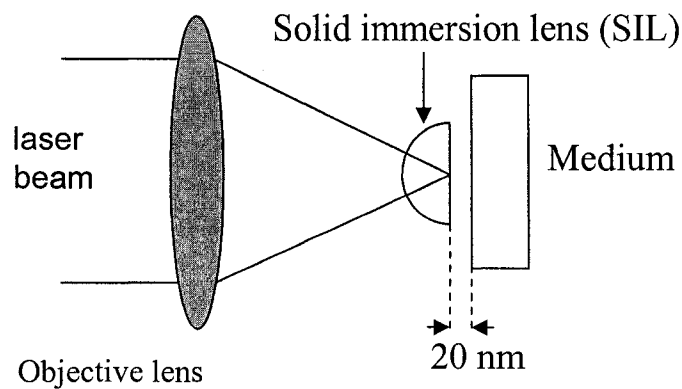


Figure 1.3 A typical near-field system using SIL.

A second way to increase the data capacity is to use volumetric optical data storage technology, as mentioned in Section 1.1. Currently, volumetric technology is divided in two research areas, which are holographic optical data storage and volumetric bit-wise optical data storage.

Since the invention of holography by Gabor in 1948 [Gabor 1948], people have tried tirelessly to develop optical memory based on the holographic optical interference technique. Chen *et al.* [Chen *et al.* 1968] first proposed to use LiNbO₃ as the holographic storage medium. In holographic storage, data sets are transferred to and from storage material as 2-D images composed of thousands of pixels, with each pixel representing a single bit of information. However, no one location in the medium is responsible for storing that one bit; each bit is distributed throughout the recorded interference fringes. Since an entire page of data can be retrieved by a two-dimensional (2D) photo detector at the same time, rather than bit-by-bit, holographic technology promises fast readout rates as well as high density. However, research into holographic data storage all but died out in the mid-70s, mostly because of the lack of suitable devices for the input and output of 2D information. In the early 90s, interest in volume-holographic data storage revived due to the availability of devices that could display and detect 2D data, including the CCD, CMOS detector chips and compact LCD display systems [Heanue *et al.* 1994]. With these new components in hand, researchers have begun to demonstrate the potential of holographic storage technology in the laboratory. However, there are two serious drawbacks of volume holographic data storage technology. The first one is the bulk equipment that is needed. The second one is that the signal noise ratio (SNR) in a

holographic storage system is only 20 dB, which is extremely low compared to the SNR of CD player that is usually between 60 and 70 dB.

The idea of volumetric bit-wise data storage is the natural extension of CD and DVD. It has been demonstrated by using two-photon fluorescence [Zhang *et al.* 2000], refractive index changes in photochromic [Suzuki *et al.* 1994], photopolymer [Strickler *et al.* 1993], photorefractive [Hisaka *et al.* 2000] materials and Super-Rens material [Wu *et al.* 2002]. The principle of this technology is illustrated in Fig. 1.4. There is a powerful laser beam focused into the desired point inside the medium, which induces some physical change, like a molecular structure change, refractive index change *etc*, if the irradiance at that focal point exceeds a threshold level. Hence, a data bit is written. As the read beam scans through the data bit, the reflected beam shows modulation in the phase or irradiance, which is then detected by an electronic detector. Therefore, the system recognizes the existence of the data bit. A confocal system is often used to reduce the inter-layer crosstalk [Toriumi *et al.* 1998].

1.3 Motivation for this study

Research into volumetric bit-wise optical data storage technology started in the mid of 1990s. Since then, two kinds of material, two-photon fluorescence and Super-Rens material, have surfaced as the ideal candidates for volumetric bit-wise optical data storage technology. A fundamental question is: *How much data storage capacity can a volumetric storage device have?* In this study, we set out to answer two aspects of this question. The first aspect is to calculate the limitation on data storage capacity set by the

optical system. It is obvious that an optical system can not read and write an infinite number of layers of data marks. Several optical systems are designed in this dissertation to meet the challenges posed by volumetric storage and their corresponding maximum data storage capacities are calculated. The second aspect is to find the limitation on the data capacity set by the material itself. One example is the Super-Rens material. The transmission rate and non-linear coefficient of one layer of Super-Rens material limits the number of layers that can be stacked in a disk, since the power of the laser available is finite. The combination of the two aspects ultimately determines the data capacity limit for a volumetric system.

1.4 Outline of dissertation

The dissertation is organized as follows. Chapter 2 provides background of volumetric optical data storage technology, which includes bit-wise and holographic storage. Two kinds of material that are promising for the bit-wise storage are also introduced in Chapter 2. Chapter 3 presents three methods that are used to simulate the inter-layer crosstalk of volumetric bit-wise storage systems. The results from different simulation methods are also compared and discussed. Chapter 4 discusses several far-field and near-field optical system designs that are suitable for volumetric storage with proper spherical aberration compensation. Chapter 5 defines effective surface density and calculates maximum storage densities of the far-field and near-field systems based on conclusions drawn from Chapter 3 and Chapter 4. Chapter 6 presents experimental results of testing fluorescent material in a simulated space environment using a custom test

stand. The experimental results of testing Super-Rens material with a custom test stand are described in Chapter 7. Chapter 8 concludes the evaluation of potential for volumetric bit-wise data storage, as well as suggestions for future work.

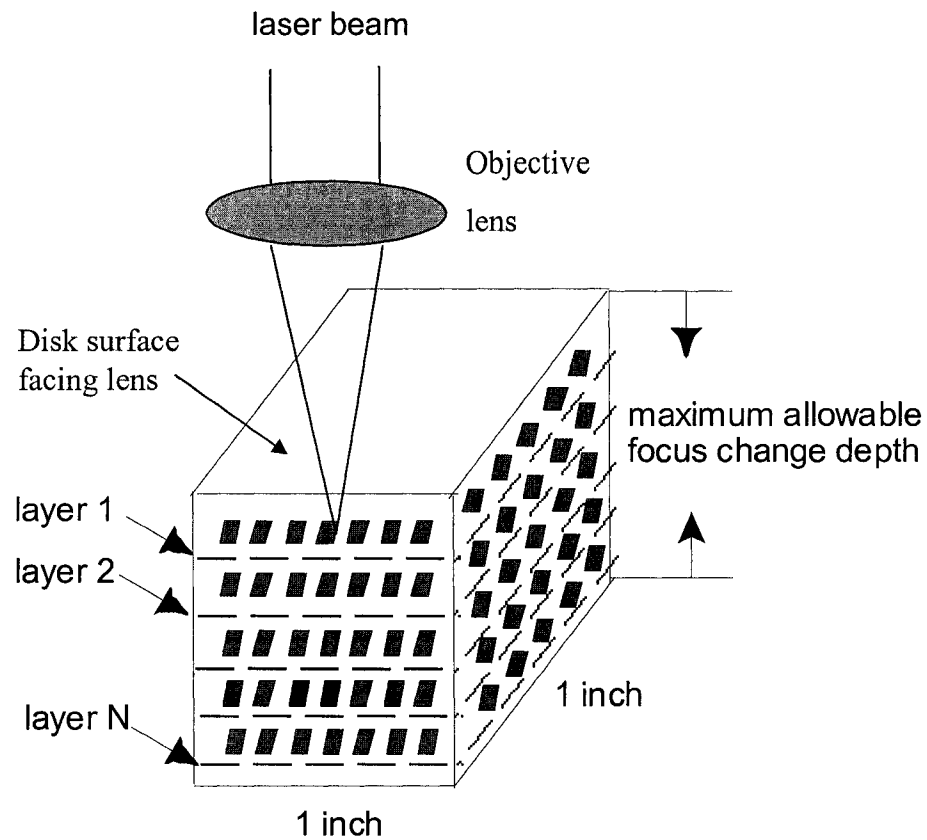


Figure 1.4 A schematic drawing of the volumetric bit-wise optical data storage system

Chapter 2

BACKGROUND

This chapter introduces the history of volumetric optical data storage technology and two kinds of material that are promising for bit-wise storage. A brief review of holographic storage is followed by a detailed review of bit-wise volumetric technology.

2.1 History of holographic volumetric data storage

Chen *et al.* [Chen *et al.* 1968] proposed to use LiNbO₃ as a holographic storage medium. The LiNbO₃ material shows optically-induced refractive index inhomogeneities at the focal point of a high power laser beam, which makes it an attractive candidate in holographic storage. Chen exposed a 1cm thick poled single crystal of LiNbO₃ to a 0.488 μm light beam and read out with laser beam at 0.633 μm . Diffraction efficiencies up to 40% were observed at recorded spatial frequencies of as high as 1600 lines/mm. Chen demonstrated storage and reconstruction of one photo in such a crystal.

Staebler [Staebler *et al.* 1975] first developed angular multiplexing technology that is used to store multiple holograms sequentially in a Fe-doped LiNbO₃ crystal. Staebler's idea was to rotate the crystal by 0.1 degree after each recording. One hundred holograms were stored in this way and the diffraction efficiency in the readout process was higher than 2.5%. The drawback of this technology is that the sample needs to be rotated precisely after each recording, which introduces vibration and requires high precision alignment. To overcome this difficulty, Rakuljic [Rakuljic, *et al.* 1992] introduced the wavelength multiplexing method, which uses different wavelength to

write each hologram. He demonstrated recording ten holograms in a 2 mm thick LiNbO₃ crystal. Heanue [Heanue *et al.* 1994] presented the phase-code multiplexing method, which permits fixed position of the crystal and fixed wavelength. He suggested storing M images with M different reference waves, which were generated by an amplitude spatial light modulator and a phase spatial light modulator. He demonstrated storage of four 308-page stacks with 1592 bits per page in a 0.1 cm³ LiNbO₃ crystal, which corresponds to 2×10^7 bits-cm⁻³. However, the signal-to-noise ratio is only 20 dB. The recent trend [Orlov *et al.* 2003] is to make the recording material into a cylinder shape, which is similar to a CD. The reference beam is a spherical wave produced by a lens of high numerical aperture. The information to be stored on the disk is imprinted on a plane wave that illuminates a spatial light modulator. The nonplanar phase front of the reference beam allows one to multiplex and retrieve holograms selectively by rotating the disk. This technology is called shift multiplexing. However the low signal-to-noise ratio (SNR < 20 dB) and bulky equipments prevents volumetric holographic storage to be commercialized at this time.

2.2 History of bit-wise volumetric optical data storage

There are three categories of material that have been used in bit-wise volumetric optical data storage technology. The first category is refractive-index-change material, which consists of photopolymer, photorefractive, and photochromic material. The second category is fluorescent material. The third category is material with Super-Rens structure.

2.2.1 Refractive-index-change material

Wilson [Wilson et al 1996] first pointed out, using three dimensional optical transfer function (3D OTF) theory, that a reflective type microscope with $NA < 1$ does not have enough bandwidth in Fourier space to read data marks if a refractive-index-change material is used as the storage medium. The 3D OTF of a reflection type microscope has a missing cone in the low frequency region, where the Fourier spectrum of the three-dimensional data mark pattern $O(f_x, f_y, f_z)$ is. In a microscope with $NA < 1$, there is no overlap between the 3D OTF and $O(f_x, f_y, f_z)$. Wilson further suggested that by carefully selecting the writing and reading laser wavelengths and using an extremely high NA objective lens to stretch the 3D OTF far enough so that there is an overlap, a reflection type microscope may be able to read data marks in a refractive-index-change medium. Note that all commercial optical data storage devices are reflection-type microscopes, because it requires less optical components compared to a transmission type microscope.

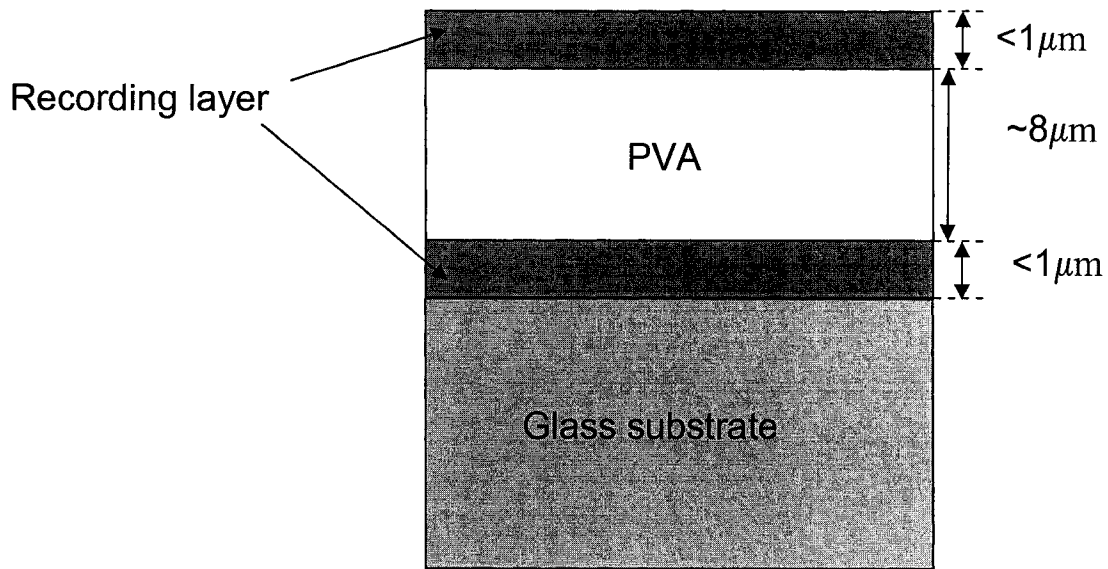
The first experiment to demonstrate the storage ability of the refractive-index-change material was done by using photopolymer. It is a class of material that increases its refractive index when it's illuminated by a high power laser. Two-photon photopolymerization occurred at the focal point of the laser beam, which leads to a density increase of the polymer medium and a slightly permanent local refractive index change. Hence, photopolymer is used as a read only material (ROM). Strickler [Strickler et al 1993] demonstrated multiple layer bit-wise optical data storage in a 100 μm thick

photopolymer Cibatoool film by using a transmission type microscope. The film was irradiated through a high NA objective lens (NA=1.4) with 100-fs pulses of a 0.62 μm laser beam. Twenty-five layers of data patterns were written in such a photopolymer film. A differential interference contrast microscope was used to read the data pattern.

Researchers in Japan continued developing photopolymers that were suitable for a reflection-type microscope. Ishikawa [Ishikawa *et al.* 1998] proposed to use a sandwiched structure, in which photopolymer thin films and nonphotosensitive transparent films were stacked alternately. Such a structure is shown conceptually in Fig. 2.1. By using this kind of sandwich structure, the 3D OTF of a confocal reflection microscope, which was used in his experiment, had adequate overlap with the Fourier spectrum of the data marks, which lead to the successful readout of the data bits. Ishikawa demonstrated recording and reading two layers of data marks.

Photorefractive crystals also change their refractive index under the application of an intense laser spot. However, unlike photopolymers, the refractive index change is reversible, which makes the photorefractive crystal an erasable material. Kawata [Kawata *et al* 1995] recorded three layers of data in a Fe-doped LiNbO₃ photorefractive crystal. A transmission type confocal laser scanning microscope with a phase-contrast objective lens was used in Kawata's experiment.

Photochromic material uses two isomers, A and B, with different absorption spectra. In the writing process, the material is changed from A to B at the focus spot. Note that B is changed to A if illuminated by laser with another wavelength. There is a small difference in the refractive index between the two isomers. Therefore, data mark



Recording layer: photopolymer thin film.

PVA: non-photosensitive transparent film.

Figure 2.1 A sandwiched structure for refractive-index-change material.

patterns are generated and then detected. Toriumi [Toriumi *et al.* 1998] first demonstrated recording and reading 26 layers of data bits in a homogeneous photochromic medium by using a reflection confocal microscope. He carefully selected the numerical aperture of the objective lens and the wavelength of the writing and reading laser beams. In the writing process, λ was 760 nm and NA was 1.4. In the reading process, λ was 0.633 μm and NA was 0.75.

The above experiments using refractive-index-change materials are all static tests. There has been no report of dynamic tests on this kind of medium.

In general, there are three major obstacles in using the refractive index change material as a volumetric bit-wise data storage medium. The first obstacle is that the refractive index change is on the order of 10^{-2} , which leads to a great difficulty to detect the data bits. The second obstacle is that the reflection-type microscope, which is the most common system used in data storage technology, can not read the data bits inside a homogeneous refractive index change medium if the NA of the objective lens is less than 1. The third obstacle is that the thin film in a sandwiched structure needs to be carefully designed so that sufficient laser power reaches the bottom layer. Until now, there are reports of recording and reading only 2 layers of data marks in such a structure.

2.2.2 Fluorescent material

The second category for volumetric bit-wise media is fluorescent material, which was first proposed as a volumetric bit-wise data storage medium by Parthenopoulos [Parthenopoulos *et al.* 1989]. He presented the principles for a three dimensional bit-wise optical memory device by using two forms of spirobenzopyran, which is a photochromic dye, embedded in PMMA. This photochromic molecule, initially in the spiropyran form, absorbs two photons at the same time via a two-photon excitation when illuminated by a tightly focused laser beam with $\lambda=0.55 \mu\text{m}$ and yields the merocyanine form via heterolytic cleavage. Thus, the molecular structure is changed into a new 'written' form, and a data bit is generated. The advantage of a 2-photon absorption process is based upon its ability to selectively excite molecules inside a volume without populating molecules on the surface of the device. This selection may be achieved because the laser photons

have less energy than the energy gap between the ground state and first allowed electronic level. Therefore, photons propagate through the medium without being absorbed by a one-photon process. However, in the vicinity of the laser beam focus, the intensity is high enough so that two photons can combine to excite carriers across the energy gap. The transition probability of a 2-photon absorption process partly depends upon the writing beam irradiance and carrier diffusion, so lasers producing high irradiance in short pulses, *i.e.* picosecond and sub-picosecond pulses, must be used.

The merocyanine form absorbs in the red region of the visible spectrum and emits red-shifted fluorescence. Figure 2.2 illustrates the principle of the fluorescent medium. The presence or absence of this fluorescence is detected and classified as a physical '1' or '0' for the stored data mark. Since the decay lifetime is ~ 5 nanoseconds and the concentration of molecules is high, it is possible to excite the written molecules many times in a single read cycle and increase the total light collected at the detector.

The first static test on fluorescent media was performed by Wang [Wang *et al.* 1997]. He demonstrated recording and reading out 100 layers of 100×100 random bits inside a $1\text{cm} \times 1\text{cm} \times 1\text{cm}$ cube made of the fluorescent medium. A frequency-doubled Nd:YAG laser (35-ps pulses, 100mJ/pulses, 10Hz) was used in the writing process. In the readout process, a 0.3 mW He-Ne laser was used to induce the fluorescence.

Three years later, Walker [Walker *et al.* 2000] built a dynamic test stand with closed-loop focus and tracking servo for the fluorescent medium. Two fluorescent

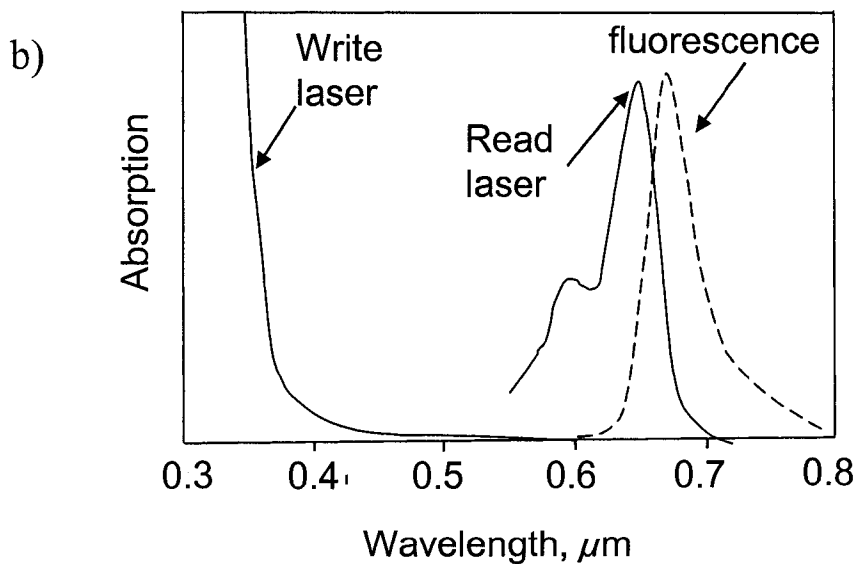
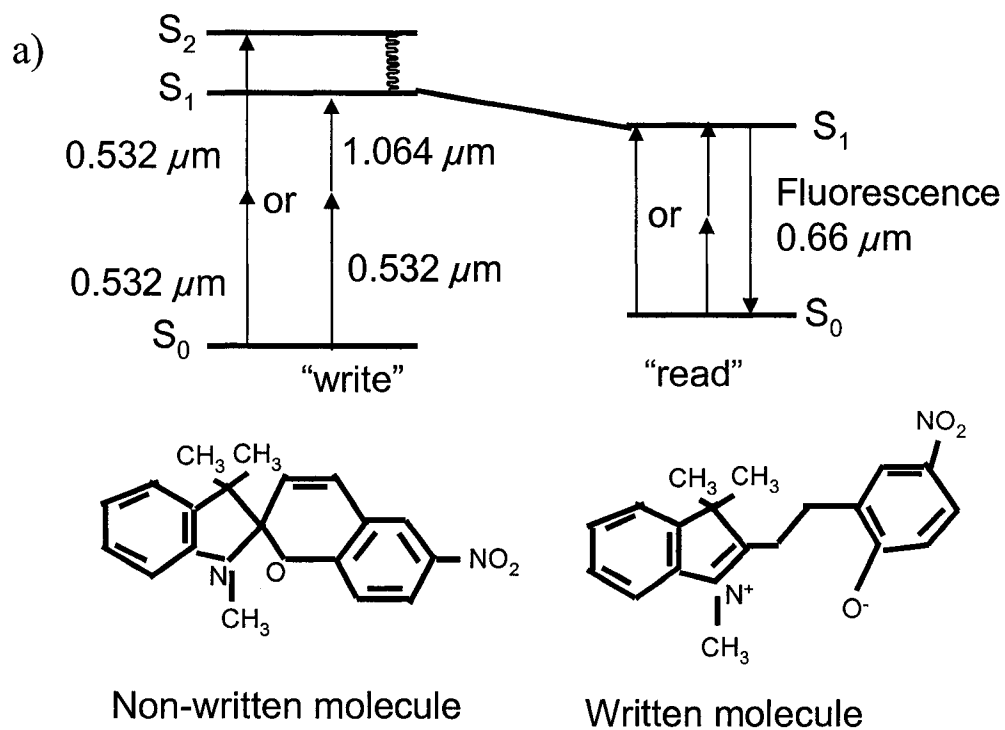


Figure 2.2 A physical description of two-photon absorption. (a) Energy-level diagram and molecular structure of unwritten and written forms, showing fluorescence (b) absorption spectra and fluorescence spectrum of the unwritten and written forms of the material

spots, slightly defocused from each other and straddling the middle of the recorded mark as shown in Fig. 2.3, were used to generate the focus error signal (FES) and tracking error signal (TES). When the lens was in focus, the same amount of fluorescent power was incident upon both detector 1 and detector 2. When the lens was inside focus, the fluorescent power on detector 1 was reduced relative to the fluorescent power level on detector 2, and the situation was reversed when the lens was outside focus. A similar approach was used for TES generation, where the left and right halves of the bi-cell detector were subtracted. A 35 dB carrier-to-noise-ratio (CNR) was achieved in his test stand.

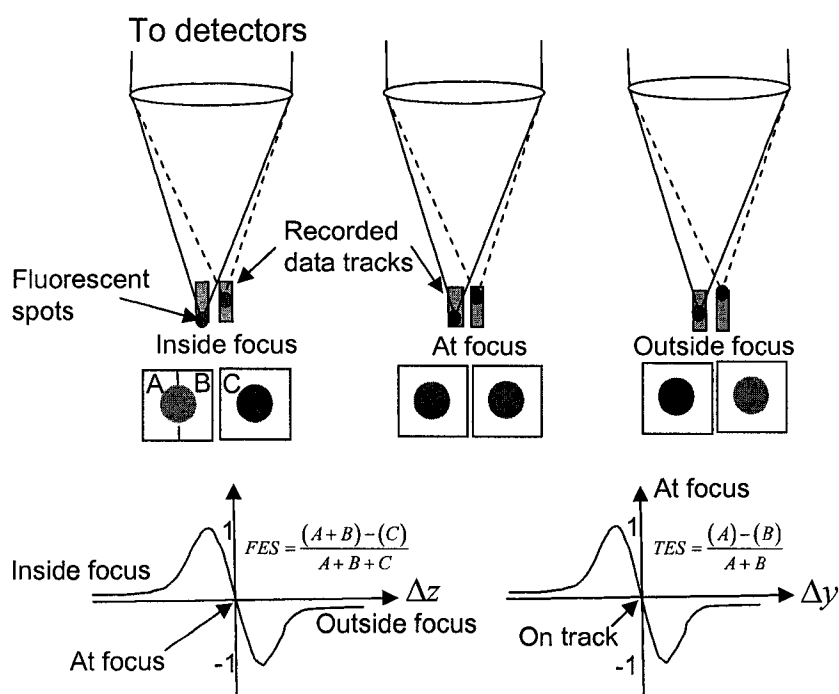


Figure 2.3 A two-fluorescent-spots servo technique for the fluorescent material.

Miller [Miller *et al.* 2003] continued developing a robust servo system for fluorescent media. He proposed to mount the disk made from the fluorescent medium to a standard grooved disk, e.g. a commercial CD, so that they rotated together on a common axis. A closed-loop servo system was coupled to the CD, which was also called the “master disk”, and a particular track was followed. When track lock was achieved by the master actuator, the driver signal output from the servo was also coupled to a “slave” system. The slave signal drove the positioning coils in the slave actuator head used to read and write to the fluorescent medium. The read/write beam thus traced a path inside the medium that replicated the track followed by the master servo loop. Figure 2.4 illustrates the design concept of the “master-slave-servo”. Miller demonstrated recording and reading multiple tracks of random bits in a disk made from the fluorescent medium.

Since shot noise is the dominant noise in a system using fluorescence, the data rate is limited. To overcome this problem, Walker [Walker *et al.* 2002] presented the concept of 3-D parallel readout, which is simultaneous readout of multiple-tracks across multiple layers, and realized the concept by utilizing a depth-transfer optical system to image a tilted object plane of 64 digital data channels in a 4 (layer) by 16 (tracks/layer) to a tilted image-detector plane. Hence, the data rate was increased 64 times compared to a single data channel.

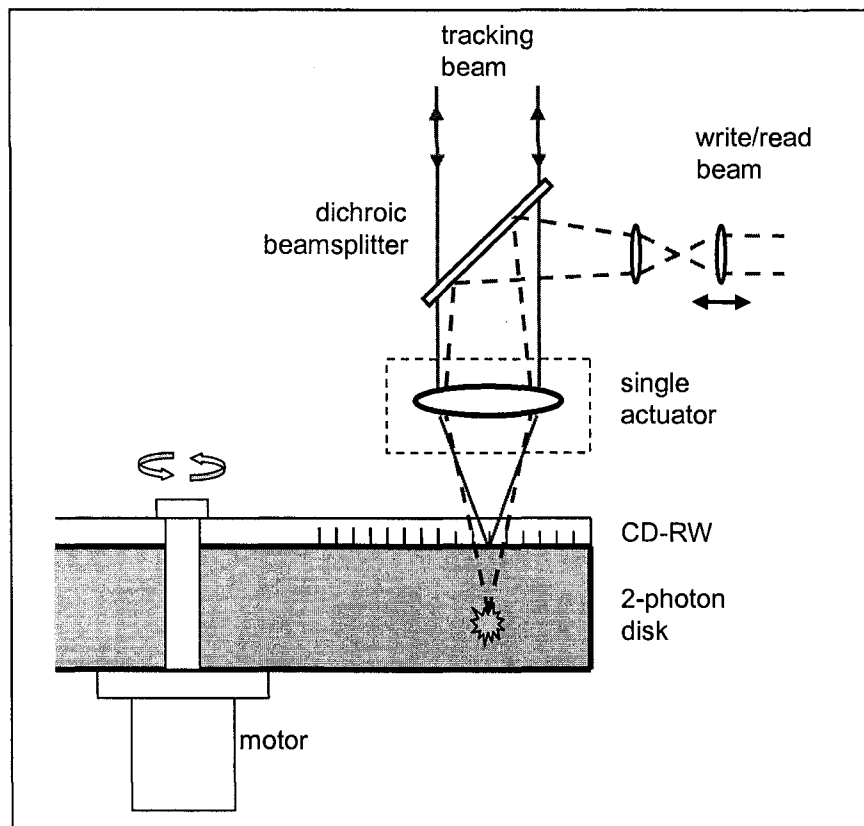


Figure 2.4 A schematic drawing of the optical system using master slave servo technique.

2.2.3 Super-Rens material

The third category is the super-resolution near-field structure (Super-Rens) medium, which was first proposed by Tominaga [Tominaga *et al.* 1998]. Figure 2.5 shows the cross section of the Super-Rens structure. It is made of three layers, in which one AgO_x layer is sandwiched by two ZnS-SiO_2 layers. AgO_x rapidly decomposes into Ag and oxygen in a small area heated above the threshold temperature by a focused laser beam. After the laser beam is removed, Ag and oxygen form the AgO_x again. Small marks of less than 100nm were recorded in recent experiment [Fuji *et al.* 2000].

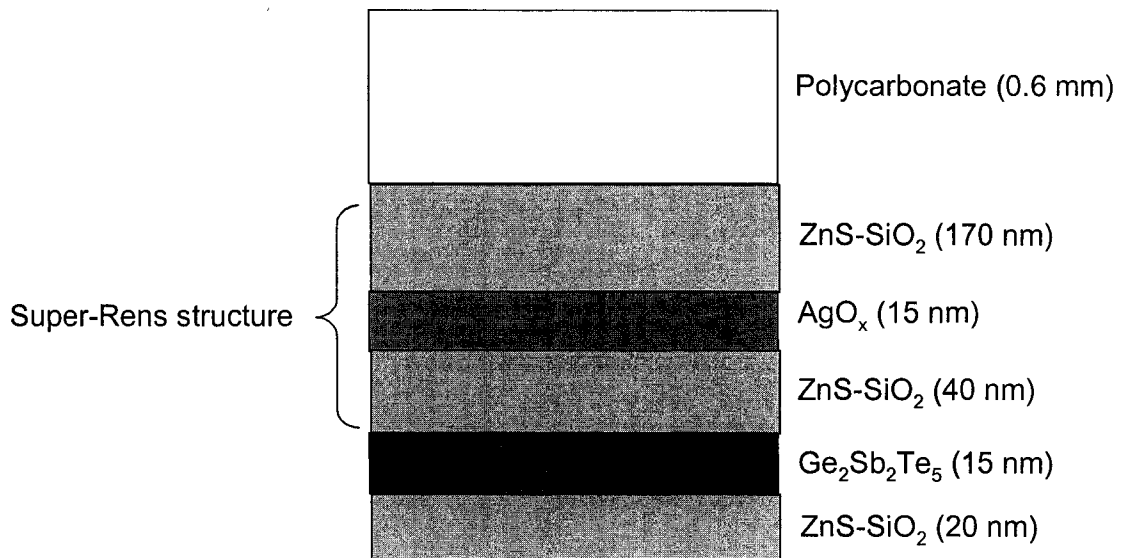


Figure 2.5 The concept of Super-Rens structure.

Wu [Wu *et al.* 2003] used the Z-scan method to measure the nonlinear coefficient of a triple layer silver oxide structure versus the oxygen content. What he found is that the character of the nonlinearity changes from nonreversible increased transmission at low oxygen content to positive, reversible and power-dependent second order non-linear coefficient at medium oxygen content to a nonreversible increased transmission at high oxygen content. Later, he demonstrated recording and reading data bits on an optimized multiple layer silver oxide structure [Wu *et al.* 2003].

The high transmission rate of a single layer Super-Rens structure makes it possible to provide enough laser energy reaching the bottom layer for an adequate signal-

to-noise ratio (SNR) in a ten-layer Super-Rens optical disk. The large nonlinear coefficient means that data marks can be written on each layer by using a commercially available laser diode. Hence, the high transmission rate and large nonlinear coefficient makes Super-Rens medium a very attractive candidate for volumetric bit-wise data storage

The remainder of this dissertation focuses on characterizing the system and material aspects of a fluorescent medium and a Super-Rens medium.

Chapter 3

INTER-LAYER CROSSTALK

This chapter presents inter-layer crosstalk simulation results for optical systems that use fluorescent material and Super-Rens material. Comparisons of the results from different simulation methods are discussed.

3.1 Introduction to inter-layer crosstalk and three simulation methods

Inter-layer crosstalk, which is the amount of signal from an adjacent layer that is detected while scanning a layer of interest, is the most important factor that limits layer spacing. Crosstalk is modeled with the geometry shown in Fig. 3.1, where the incident laser beam is focused into data layer 1, which is also the layer of interest. As the laser beam scans through the data mark pattern, two readout signals are generated and detected by the detector. The readout signal modulation for data layers 1 and 2 are I_A and I_B , respectively. The inter-layer crosstalk is

$$X = 20 \log_{10} \frac{I_B}{I_A}. \quad (3.1)$$

The simulation procedure to calculate X is a two-step process, where I_A and I_B are calculated separately.

It's well known that a small detector in a confocal read out system reduces the inter-layer crosstalk, but the small detector also limits the detected signal and leads to carrier-to-noise-ratio (CNR) reduction [Dereniak et al., 1996]. The impact of detector size on X and CNR in an optical system using fluorescent and Super-Rens material is

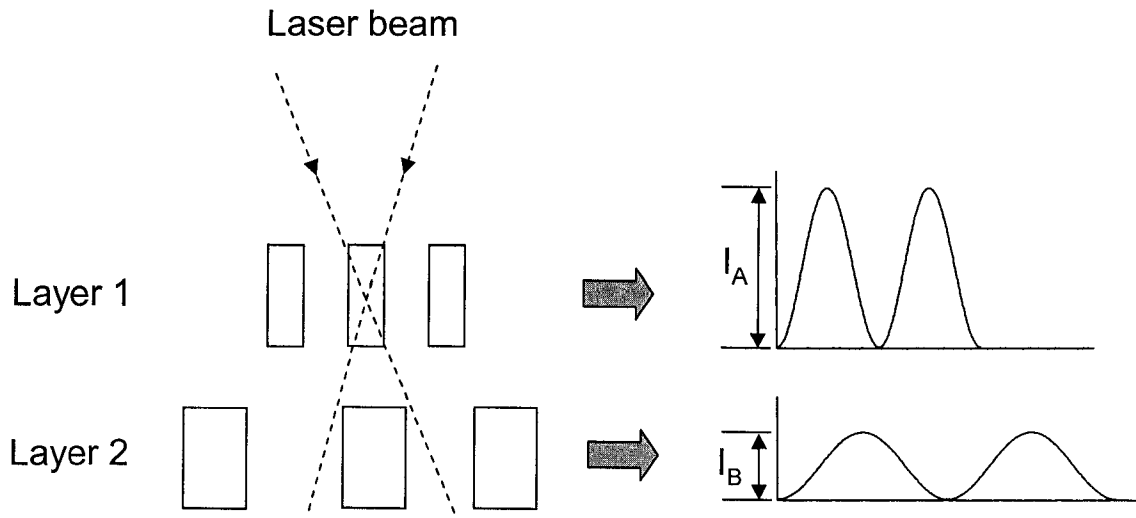


Figure 3.1 The crosstalk ratio $20\log_{10}(I_B/I_A)$ is measured via a two-step process. (a) The readout signal modulation from scanning layer 1 is measured (I_A); (b) The readout signal modulation from scanning layer 2 is measured (I_B).

discussed in this chapter by calculating X and CNR with three different methods, which are (1) the three-dimensional optical transfer function (3D OTF) [Gauderon *et al.* 1999]; (2) a physical-optics-based software program called OPTISCAN [Milster *et al.* 2002]; and (3) finite difference time domain (FDTD) [Taflove *et al.* 2000].

3D OTF has been used to characterize the lateral and axial resolution of a fluorescence microscope [Gu *et al.* 1991]. An optical read out system that uses fluorescent material is basically a fast scanning fluorescence microscope, so a similar analysis is used in this work. Section 3.2.1 presents the detailed calculation of 3D OTF and the associated inter-layer crosstalk.

OPTISCAN is a physical-optics based quasi-vector diffraction software program that operates in the MatlabTM language. The ability to perform quasi-vector diffraction calculation for high NA imaging system is important, since most objective lenses used in optical data storage have NA higher than 0.6. Another unique aspect of OPTISCAN is its graphical user interface (GUI). The methodology and simulation results with OPTISCAN are illustrated in detail in Section 3.2.2.

A finite difference time domain (FDTD) simulation tool, which provides a rigorous vector EM treatment, is used to investigate the interaction between the focused laser beam and data mark in the Super-Rens material and design considerations for the layer spacing. 3D OTF and quasi-vector analysis can not be used for Super-Rens material, because the data layer in this material can not be simply modeled as a homogeneous structure. Hence, a rigorous vector EM treatment is needed.

The general idea of the FDTD algorithm is to apply finite difference analysis to Maxwell's equations to obtain electric and magnetic fields in a given structure [Taflove, *et al.* 2000]. Finite difference analysis is used to solve Maxwell's equations by replacing the derivative terms with finite discrete terms. Temporal and spatial domains are discretized into Yee cells (~20 nm per side for these calculations) for solving Maxwell's equations with initial conditions and boundary conditions, as shown in Fig. 3.2, For example, Eq. (3.2) is the expression of E_x and H_x in the form of discretized Maxwell's equations,

$$\begin{aligned}
H_x^{n+1/2}(i, j+1/2, k+1/2) &= H_x^{n-1/2}(i, j+1/2, k+1/2) + \frac{\delta t}{\mu(i, j+1/2, k+1/2)\delta} \\
&\quad \times \left[E_y^n(i, j+1/2, k+1) - E_y^n(i, j+1/2, k) \right. \\
&\quad \left. + E_z^n(i, j, k+1/2) - E_z^n(i, j+1, k+1/2) \right] \\
E_x^{n+1}(i+1/2, j, k) &= \left(1 - \frac{\sigma(i+1/2, j, k)\delta t}{\varepsilon(i+1/2, j, k)} \right) E_x^n(i+1/2, j, k) \\
&\quad + \frac{\delta t}{\varepsilon(i+1/2, j, k)\delta} \left[H_z^{n+1/2}(i+1/2, j+1/2, k) \right. \\
&\quad \left. - H_z^{n+1/2}(i+1/2, j-1/2, k) + H_y^{n+1/2}(i+1/2, j, k-1/2) \right. \\
&\quad \left. - H_y^{n+1/2}(i+1/2, j, k+1/2) \right] , \tag{3.2}
\end{aligned}$$

where i, j, k are the coordinates in the Yee cell, δt is the time step, n is the number of time steps and δ is the size of Yee cell, as shown in Fig. 3.2. For each time step, the fields and their derivatives are evaluated over the three-dimensional sampling matrix. A large number of time steps results in a convergence to a steady-state condition. Section 3.3 discusses the inter-layer crosstalk of an optical system using Super-Rens material analyzed with FDTD. The particular FDTD program used in these simulations is developed within our research group [Olkkonen *et al.* 2003].

3.2 Simulation of inter-layer crosstalk for an optical system using fluorescent material

This section presents simulation results of inter-layer crosstalk for an optical system using fluorescent material by using 3D OTF and OPTISCAN simulation tools.

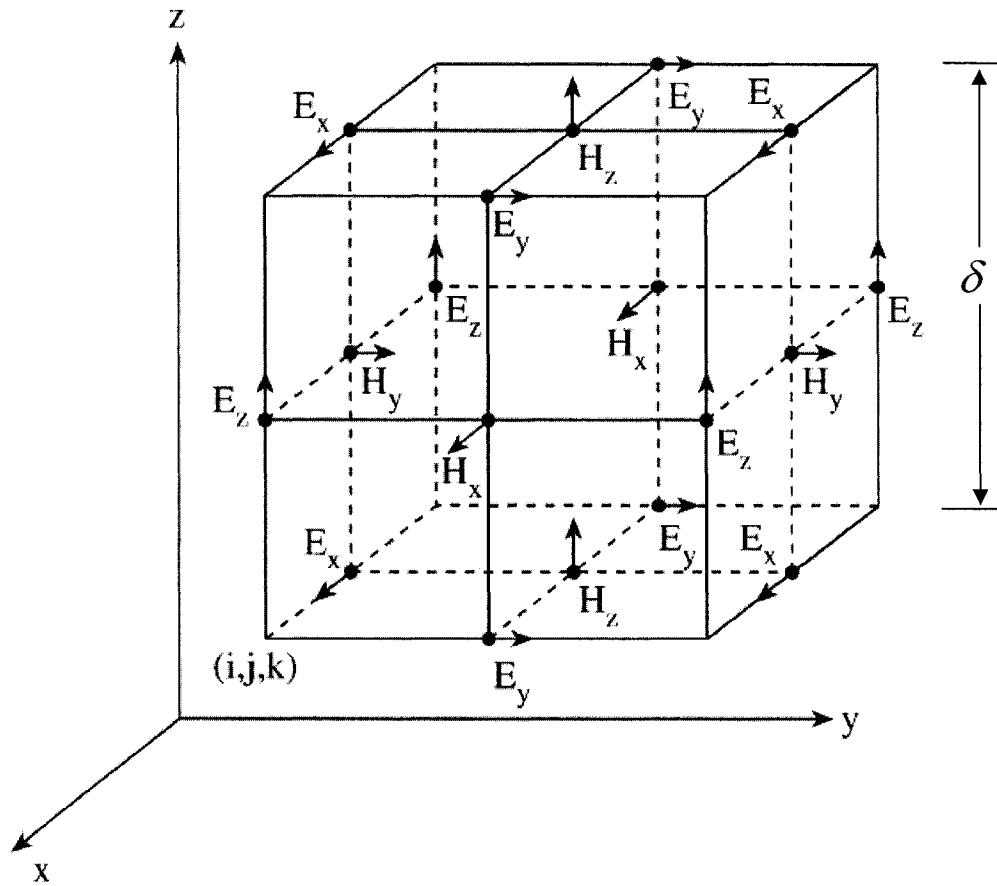


Figure 3.2 Illustration of Yee cells used in the FDTD method.

A schematic diagram of a read-out system for volumetric data storage technology is shown in Fig. 3.3. The illumination laser light, with $\lambda_L = 0.633 \mu\text{m}$ from a diode laser, is focused by an aspherical objective lens with $f_o = 3.89 \text{ mm}$ into the storage medium. The system stop is at the objective lens. Pupil function $p(x, y)$ is

$$\begin{aligned}
 p(x, y) &= 1 \text{ if } \sqrt{x^2 + y^2} \leq r_p \\
 &= 0 \text{ if } \sqrt{x^2 + y^2} > r_p,
 \end{aligned} \tag{3.3}$$

where r_p is 2.92 mm, so that the numerical aperture (NA) of the objective lens is 0.6. The beam splitter is used to reflect the illumination laser beam 90 degrees and is a long-wave pass optical filter. The filter passes the fluorescent light from the data marks, where the center of the fluorescence wavelength λ_f is $0.660 \mu\text{m}$.

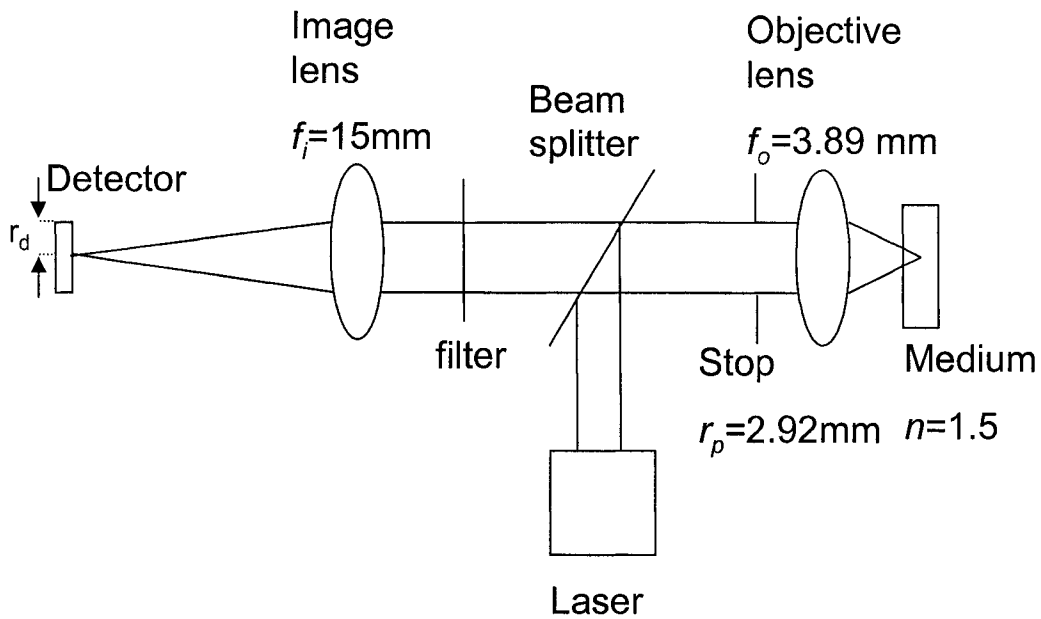


Figure 3.3 A far-field system used in the crosstalk study.

The center of the coordinate space (ξ, η, z) of the fluorescent medium is set at the paraxial focus of the objective lens, as shown in Fig. 3.4. The data mark pattern is described by function $\bar{m}(\xi - \xi_s, \eta - \eta_s, z - z_s)$, where (ξ_s, η_s, z_s) are the coordinates of the center point of the data mark pattern in the medium. The marks absorb photons and emit fluorescence. The emitted fluorescent light is focused by an imaging lens with

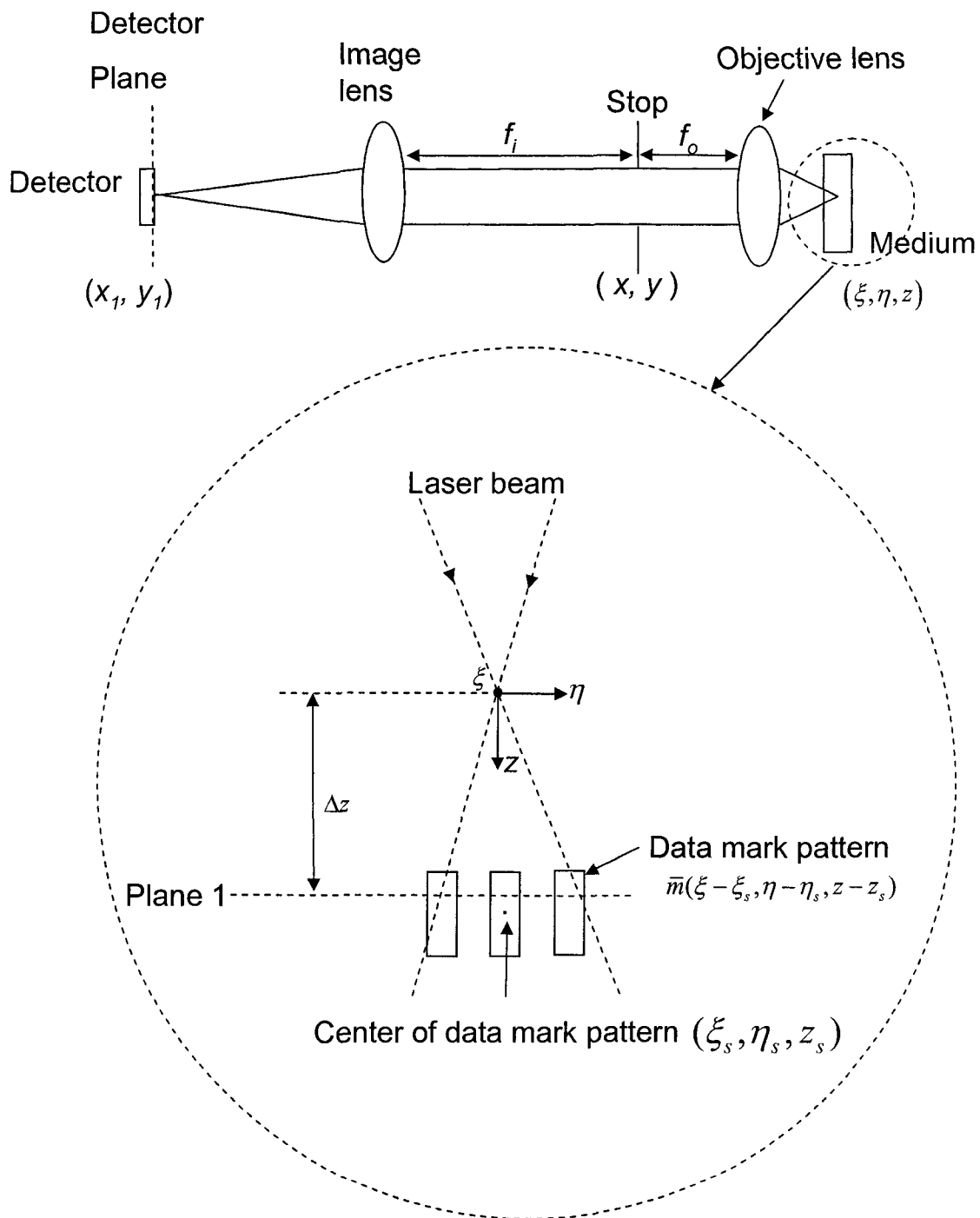


Figure 3.4 The coordinate system used in the simulation.

$f_i = 15$ mm onto a finite-sized detector (x_1, y_1) defined by a pinhole. The distance between the objective lens and the imaging lens is $L_{o \rightarrow i} = f_o + f_i = 18.89$ mm .

All three simulation tools calculate crosstalk X by first calculating the response of the detector to the scan layer (layer 1), without surrounding layers present, to estimate I_A . Then, the response of the detector to surrounding layers without the scan layer is calculated to estimate I_B . X is then calculated with Eq. (3.1).

3.2.1 Simulation using 3D OTF

Considering a collimated laser beam with uniform amplitude distribution incident on the objective lens, the electrical field distribution at Plane 1, which is Δz away from the paraxial focal plane, as shown in Fig. 3.4, is

$$E_1(\xi, \eta, \Delta z) = C \iint P(x, y) \exp\left(\frac{jk_1(\Delta z/n)}{2f_o^2}(x^2 + y^2)\right) \exp\left(\frac{jk_1}{f_o}(x\xi + y\eta)\right) dx dy, \quad (3.4)$$

where C is a constant, $k_1 = \frac{2\pi}{\lambda_L}$ and $n=1.5$ is the refractive index of the fluorescent medium. The fluorescent irradiance I_f emitted from the data marks is proportional to the irradiance of the incident laser beam I_L , that is,

$$I_L = |E_1(\xi, \eta, \Delta z)|^2. \quad (3.5)$$

The fluorescence irradiance from the data mark pattern is

$$I_f(\xi, \eta, \Delta z) = I_L(\xi, \eta, \Delta z) \times \bar{m}(\xi - \xi_s, \eta - \eta_s, \Delta z - z_s). \quad (3.6.a)$$

Without losing generality, if the data mark pattern is symmetric in the direction transverse to its center,

$$I_f(\xi, \eta, \Delta z) = I_L(\xi, \eta, \Delta z) \times \bar{m}(\xi_s - \xi, \eta_s - \eta, z_s - \Delta z). \quad (3.6.b)$$

In order to calculate the detector response to scanning the mark pattern, the fluorescence in Eq. (3.6.b) is treated as a collection of incoherent point sources. The optical system is linear and shift-invariant. A single point source at $(\xi = 0, \eta = 0, \Delta z)$ produces an electric field distribution $E(x, y)$ at stop given by

$$E(x, y) = p(x, y) \exp\left(-j \frac{k_2 (\Delta z/n)}{2f_o^2} (x^2 + y^2)\right), \quad (3.7)$$

where $k_2 = \frac{2\pi}{\lambda_f}$. Hence, the image field of this single point source on the detector plane

(x_1, y_1) is

$$\begin{aligned} E_{ps}(x_1, y_1; 0, 0, \Delta z) = & \iint p(x, y) \exp\left(-j \frac{k_2 (\Delta z/n)}{2f_o^2} (x^2 + y^2)\right) \\ & \times \exp\left(-j \frac{2\pi}{\lambda_2 f_i} (xx_1 + yy_1)\right) dx dy. \end{aligned} \quad (3.8)$$

Therefore, the irradiance $I_d(x_1, y_1)$ of the image formed by the fluorescence I_f at the detector due to the mark pattern is

$$\begin{aligned} I_d(x_1, y_1) = & \int I_f\left(\frac{x_1}{M}, \frac{y_1}{M}, \Delta z\right) ** |E_{ps}(x_1, y_1; 0, 0, \Delta z)|^2 d\Delta z \\ = & \iiint I_f\left(\frac{\alpha}{M}, \frac{\beta}{M}, \Delta z\right) |E_{ps}(\alpha - x_1, \beta - y_1; 0, 0, \Delta z)|^2 d\alpha d\beta d\Delta z, \end{aligned} \quad (3.9)$$

where $M = \frac{f_i}{f_o}$ is the transverse magnification of the optical system and ** denotes two-

dimensional convolution. Let the following variables be introduced:

$$\xi = \frac{\alpha}{M} \quad \eta = \frac{\beta}{M} \quad ,$$

in which case Eq. (3.9) becomes

$$I_d(x_1, y_1) = M^2 \iiint I_f(\xi, \eta, \Delta z) \left| E_{ps}(M\xi - x_1, M\eta - y_1; 0, 0, \Delta z) \right|^2 d\xi d\eta d\Delta z . \quad (3.10)$$

By substitution of Eq. (3.8) into Eq. (3.10), the irradiance $I_d(x_1, y_1)$ becomes

$$\begin{aligned} I_d(x_1, y_1) = M^2 \iiint I_f(\xi, \eta, \Delta z) \\ \times \left| \iint p(x, y) \exp\left(-j \frac{k_2(\Delta z/n)}{2f_o^2}(x^2 + y^2)\right) \right. \\ \left. \times \exp\left(-j \frac{2\pi}{\lambda_2 f_i} \{x(M\xi - x_1) + y(M\eta - y_1)\}\right) dx dy \right|^2 d\xi d\eta d\Delta z . \end{aligned} \quad (3.11)$$

The detector function $D(x_1, y_1)$ is defined as

$$\begin{aligned} D(x_1, y_1) = 1 \text{ if } \sqrt{x^2 + y^2} \leq r_d \\ = 0 \text{ if } \sqrt{x^2 + y^2} > r_d . \end{aligned} \quad (3.12)$$

The irradiance $I_d(x_1, y_1)$ is also a function of the scan position (ξ_s, η_s, z_s) , because mark pattern function \bar{m} is contained in the calculation of $I_f(\xi, \eta, \Delta z)$ in Eq. (3.6). If a detector is used that produces a signal directly proportional to the integrated irradiance illuminating it, the signal i_q generated by the detector versus (ξ_s, η_s, z_s) is

$$i_q(\xi_s, \eta_s, z_s) = \iint D(x_1, y_1) I_d(x_1, y_1; \xi_s, \eta_s, z_s) dx_1 dy_1 . \quad (3.13)$$

By substitution of Eqs. (3.4), (3.6.b), and (3.11) into Eq. (3.13), the signal i_q becomes

$$\begin{aligned}
i_q(\xi_s, \eta_s, z_s) &= C^2 M^2 \iint D(x_1, y_1) \left\{ \iiint \bar{m}(\xi_s - \xi, \eta_s - \eta, z_s - \Delta z) \right. \\
&\quad \times \left| \iint p(x, y) \exp\left(\frac{jk_1(\Delta z/n)}{2f_o^2}(x^2 + y^2)\right) \exp\left(\frac{jk_1}{f_o}(x\xi + y\eta)\right) dx dy \right|^2 \\
&\quad \times \left| \iint p(x, y) \exp\left(-j\frac{k_2(\Delta z/n)}{2f_o^2}(x^2 + y^2)\right) \right. \\
&\quad \times \exp\left(-j\frac{2\pi}{\lambda_2 f_i} \{x(M\xi - x_1) + y(M\eta - y_1)\}\right) dx dy \left. \right|^2 d\xi d\eta d\Delta z \left. \right\} \\
&\quad dx_1 dy_1 .
\end{aligned} \tag{3.14}$$

Equation (3.14) is rewritten as

$$i_q(\xi_s, \eta_s, z_s) = C^2 \iiint \bar{m}(\xi_s - \xi, \eta_s - \eta, z_s - \Delta z) PSF(\xi, \eta; \Delta z) d\xi d\eta d\Delta z, \tag{3.15}$$

where

$$\begin{aligned}
PSF(\xi, \eta; \Delta z) &= \iint D(x_1, y_1) \\
&\quad \times \left| \iint p(x, y) \exp\left(\frac{jk_1(\Delta z/n)}{2f_o^2}(x^2 + y^2)\right) \exp\left(\frac{jk_1}{f_o}(x\xi + y\eta)\right) dx dy \right|^2 \\
&\quad \times \left| \iint p(x, y) \exp\left(-j\frac{k_2(\Delta z/n)}{2f_o^2}(x^2 + y^2)\right) \right. \\
&\quad \times \exp\left(-j\frac{2\pi}{\lambda_2 f_i} \{x(M\xi - x_1) + y(M\eta - y_1)\}\right) dx dy \left. \right|^2 dx_1 dy_1 .
\end{aligned} \tag{3.16}$$

Equation (3.15) shows that i_q is the convolution of the data mark pattern and the two-dimensional PSF of the optical system as a function of Δz . Thus,

$$\begin{aligned}
i_q(\xi_s, \eta_s, z_s) &= \iiint O(f_x, f_y, f_z) OTF(f_x, f_y; f_z) \\
&\quad \times \exp(-j2\pi(f_x \xi_s + f_y \eta_s + f_z z_s)) df_x df_y df_z ,
\end{aligned} \tag{3.17}$$

where $O(f_x, f_y, f_z)$ and $OTF(f_x, f_y; f_z)$ are the Fourier transformations of $\bar{m}(\xi, \eta, \Delta z)$ and $PSF(\xi, \eta; \Delta z)$, respectively. Equation (3-16) can be written in a form such that $OTF(f_x, f_y; f_z)$ is the convolution of $OTF1(f_x, f_y; f_z)$ and $OTF2(f_x, f_y; f_z)$, where

$$\begin{aligned}
 OTF1(f_x, f_y; f_z) = & \iiint \left| \iint p(x, y) \exp \left(\frac{jk_1 (\Delta z/n)}{2f_o^2} (x^2 + y^2) \right) \right. \\
 & \times \exp \left(\frac{jk_1}{f_o} (x\xi + y\eta) \right) dx dy \Big|^2 \\
 & \times \exp \left(-j2\pi (f_x \xi + f_y \eta + f_z \Delta z) \right) d\xi d\eta d\Delta z ,
 \end{aligned} \tag{3.18}$$

and

$$\begin{aligned}
 OTF2(f_x, f_y; f_z) = & \iiint \left\{ \iint D(x_1, y_1) \right. \\
 & \times \left| \iint p(x, y) \exp \left(-j \frac{k_2 (\Delta z/n)}{2f_o^2} (x^2 + y^2) \right) \right. \\
 & \times \exp \left(-j \frac{2\pi}{\lambda_2 f_i} \{ x(M\xi - x_1) + y(M\eta - y_1) \} \right) dx dy \Big|^2 \\
 & \times dx_1 dy_1 \Big\} \exp \left(-j2\pi (f_x \xi + f_y \eta + f_z \Delta z) \right) d\xi d\eta d\Delta z .
 \end{aligned} \tag{3.19}$$

After lengthy mathematical manipulation, $OTF1(f_x, f_y; f_z)$ is found to be

$$\begin{aligned}
 OTF1(f_x, f_y; f_z) = & \iint p(x, y) p \left(x - f_x \lambda_L f_o, y - f_y \lambda_L f \right) \\
 & \times \delta \left(-f_x x - f_y y + f_o \left[f_z n + \frac{\lambda_L (f_x^2 + f_y^2)}{2} \right] \right) dx dy ,
 \end{aligned} \tag{3.20}$$

which is the length of a straight line in the overlap region of $p(x, y)$ and $p(x - f_x \lambda_L f_o, y - f_y \lambda_L f)$, as shown in Fig. 3.5. Likewise, $OTF2(f_x, f_y; f_z)$ is found to be

$$\begin{aligned}
 OTF2(f_x, f_y; f_z) = & \iint D(x_1, y_1) \exp\left(-j2\pi \frac{1}{M} [-f_x x_1 - f_y y_1]\right) dx_1 dy_1 \\
 & \times \left[\iint p(x, y) p(x - f_x \lambda_f f_o, y - f_y \lambda_f f_o) \right. \\
 & \left. \times \delta\left(-f_x x - f_y y + f_o \left[f_z n + \frac{\lambda_f (f_x^2 + f_y^2)}{2}\right]\right) dx dy \right]. \quad (3.21)
 \end{aligned}$$

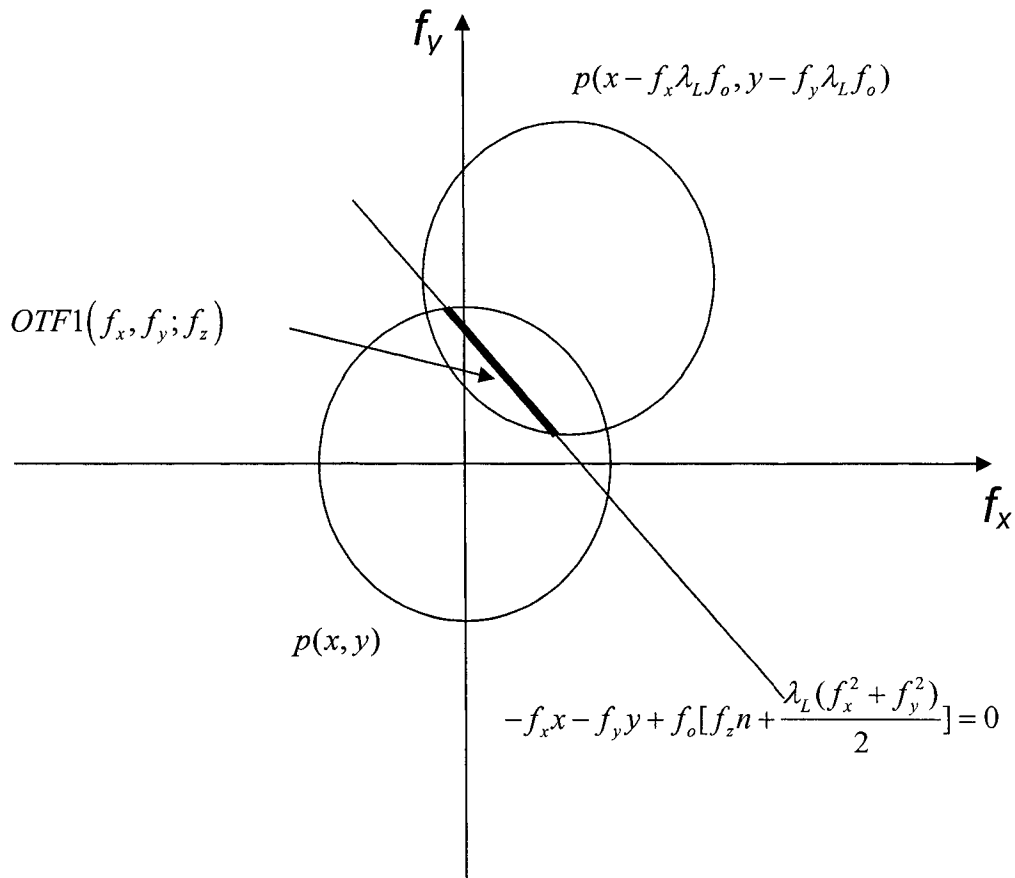


Figure 3.5 Calculation of $OTF1(f_x, f_y; f_z)$

Notice that there is an extra detector factor in *OTF2* compared to *OTF1*. Another interesting point is that the wavelengths used in *OTF1* and *OTF2* are λ_L and λ_f , respectively. MatlabTM is used to calculate the 3D OTF numerically. First, *OTF1* and *OTF2* are calculated. The results are two three-dimensional matrixes in Fourier space (f_x, f_y, f_z) . The convolution product of these two matrixes is the 3D OTF. (Note that a single calculation of the convolution process for two three-dimensional $(71 \times 71 \times 71)$ matrixes in Matlab takes up to five hours on a Pentium 4 type computer.) The cutoff frequency of the 3D OTF is

$$\begin{aligned} f_x &\in \left[\frac{-4NA}{\lambda_{eff}}, \frac{4NA}{\lambda_{eff}} \right] \\ f_y &\in \left[\frac{-4NA}{\lambda_{eff}}, \frac{4NA}{\lambda_{eff}} \right] \\ f_z &\in \left[\frac{-NA^2}{n\lambda_{eff}}, \frac{NA^2}{n\lambda_{eff}} \right], \end{aligned} \quad (3.22)$$

where $\lambda_{eff} = \frac{2\lambda_L\lambda_f}{\lambda_L + \lambda_f}$. Notice that the z-dimension cutoff frequency is the inverse of the

laser beam depth-of-focus $Z_f = \frac{\lambda n}{NA^2}$.

To better characterize the impact of r_d on 3D OTF, a normalized detector radius is defined as

$$v_d = \frac{2\pi r_d}{M(\lambda_{eff}/NA)}. \quad (3.23)$$

If v_d is smaller than 1, the system is confocal. If v_d is bigger than 6, the system is non-confocal [Sheppard *et al.* 1990]. The physical radius of the detector in the simulation is set to $r_d = 0.6 \mu\text{m}$ and $5.4 \mu\text{m}$ ¹, which correspond to $v_d = 0.9$ and 8, respectively, for both the confocal and non-confocal configurations. Figure 3.6 shows the profile of 3D OTF in the f_z direction, in which the dashed line indicates the confocal configuration and the solid line is for the non-confocal configuration. The confocal system clearly has wider frequency response compared to the non-confocal system. However, the cut-off frequency of both systems is the same, which means that, in the absence of noise, reducing detector size does not enable the instrument to detect smaller objects in the z direction. However, it can increase the image contrast. To enhance the system's resolution ability in the axial direction, an objective lens with higher NA or a laser with shorter wavelength should be used.

Figure 3.7 shows mark patterns used to simulate inter-layer crosstalk. Rectangular marks in layers 1 and 3 have $L_\xi = L_\eta = 1 \mu\text{m}$ with 50% duty cycle ($T_\xi = T_\eta = 2 \mu\text{m}$). The mark sizes in layers 1 and 3 are chosen to equal the full-width-at $1/e^2$ of the diffraction limited laser spot at focus expressed as $s = \lambda_L / NA$. Marks in layer 2 have $L_\xi = L_\eta = \frac{1}{2}s$ with 50% duty cycle ($T_\xi = T_\eta = 1 \mu\text{m}$). For all layers, $L_z = 0.9 \mu\text{m}$. ΔL is the depth between the focus point and the top of the data mark in layer 2. This particular

¹ The choice for a confocal detector radius is not practical in real experiments. The detector radius for a confocal system is set for simulation only and used to illustrate the effect of the confocal system. By increasing the focal length of the imaging lens, a realistic pinhole size can be designed for an experimental confocal system.

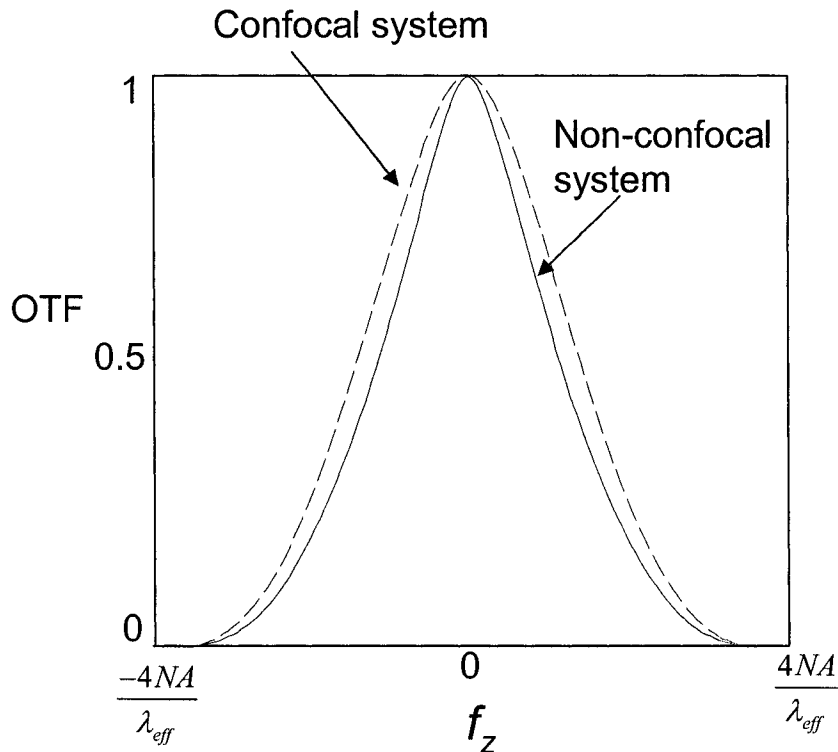


Figure 3.6 Profiles of 3D OTF of a confocal system and a non-confocal system in the f_z axis. The dashed line represents the confocal system. The solid line represents the non-confocal system.

combination of a high-frequency pattern sandwiched between two lower-frequency patterns is analogous to the worst-case crosstalk condition in a single layer, where a high-frequency track lies between two low-frequency tracks. Signal levels from the low-frequency data are large compared to the smaller signals from the high-frequency pattern in the scan track [Upton *et al.* 2001]. Both confocal ($v_d=0.9$) and non-confocal ($v_d=8$) systems are considered.

additional spacing factor γ is defined as T_z/Z_f for acceptable crosstalk performance.

This simulation shows that the $X = -30$ dB and $X = -13$ dB when $T_z = 3.4 \mu\text{m}$ ($\gamma = 1.3$) for a confocal and non-confocal systems, respectively. X is less than -30 dB when $T_z = 5.4 \mu\text{m}$ ($\gamma = 2.1$) in a non-confocal system.

Table 3.1. The inter-layer crosstalk X versus T_z for both confocal and non-confocal systems at $\Delta L = 0.45 \mu\text{m}$.

T_z (μm)	Δb (μm)	γ	Detector	X(dB)
3.4	2.5	1.3	confocal	-30.0
			non-confocal	-13.0
3.9	3.0	1.5	confocal	-35.4
			non-confocal	-17.1
4.4	3.5	1.7	confocal	-39.1
			non-confocal	-22.4
4.9	4.0	1.9	confocal	-45.0
			non-confocal	-26.7
5.4	4.5	2.1	confocal	-49.1
			non-confocal	-30.3

Although a confocal system tends to reduce inter-layer crosstalk X , it also limits the amount of light collected by the detector, which leads to a small carrier noise ratio (CNR). The CNR of a fluorescent medium, which is shot-noise limited, is $\text{CNR} = D + 10 \log_{10}(i_d)$, where i_d is the signal derived from the simulation, and D is a constant. All data mark patterns exhibit the same constant D . Experimental results indicate that a

similar non-confocal system achieves $\text{CNR} = 42 \text{ dB}$ when the mark size is $1\mu\text{m} \times 1\mu\text{m} \times 10\mu\text{m}$ [McCormick *et al.* 2000]. Therefore, CNR of a specific mark pattern is $\text{CNR} = 42 + 10 \log_{10}(i_q/i_o)$, where i_q is the simulation result of the signal of a specific data mark pattern and i_o is the simulation result for a mark pattern with mark size $1\mu\text{m} \times 1\mu\text{m} \times 10\mu\text{m}$ and $v_d = 8$. Table 3.2 shows CNR versus v_d when the laser beam scans through data marks in layer 2 at $\Delta L = 0.45 \mu\text{m}$ and $T_z = 3.4 \mu\text{m}$. The simulation shows that the confocal system ($v_d = 0.9$) reduces CNR by 5.2 dB compared to a non-confocal system ($v_d = 8$).

Table 3.2. CNR versus v_d when the laser beam scans through data marks in layer 2 at $\Delta L = 0.45 \mu\text{m}$ and $T_z = 3.4 \mu\text{m}$.

v_d	CNR (dB)
1	28.5
2	31.9
4	33.1
6	33.6
8	33.7

3.2.2 Simulation using OPTISCAN

It takes four steps in OPTISCAN to calculate the readout signal for a given data mark pattern with the optical system described in Section 3.2.1.

Step 1: Figure 3.8 illustrates the basic idea for step 1. A data mark with the size $L_\xi \times L_\eta \times L_z$, where ξ and η are transverse coordinates and z is the depth dimension, is modeled as a collection of N sub-layers. The rule of thumb for determining N is that

$L_z/N \leq \left(\frac{\lambda n}{NA^2} \right) / 10$. This rule of thumb is based on the fact that the electrical field

distribution changes very slowly within the depth of $\left(\frac{\lambda n}{NA^2} \right) / 10$. By modeling the data

mark in this way, a complicated 3D imaging problem is decomposed into multiple 2D imaging problems. The interference of each layer is ignored, due to the fact that the fluorescent light is incoherent in nature and there are no thin film interference layers in the fluorescent medium. The electric field distribution $\vec{E}_j(\xi, \eta, \Delta z)$ illuminating the data marks, where $j = 1, 2, \dots, N$ refers to the surfaces 1 to N shown in Fig. 3.8 as the surfaces associated with each sub-layer, are calculated with the quasi-vector diffraction program OPTISCAN.

Step 2: The purpose of this step is to calculate the fluorescent radiance $L_f(\xi, \eta, \Delta z)$

emitted from each surface. The assumptions used in step 2 are that $\left| \vec{E}_j(\xi, \eta, \Delta z) \right|^2$ is well

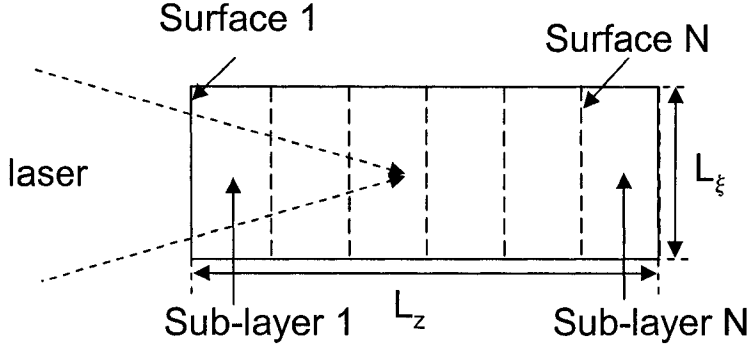


Figure 3.8 A data mark is decomposed into N layers.

below the saturation level of the fluorine and $L_f(\xi, \eta, \Delta z)$ is proportional to

$|\vec{E}_j(\xi, \eta, \Delta z)|^2 \times \bar{m}(\xi - \xi_s, \eta - \eta_s, \Delta z - z_s)$. Furthermore,

$$\frac{L_f(\xi, \eta, \Delta z)}{|\vec{E}_{i,j}(\xi, \eta, \Delta z)|^2 \times \bar{m}(\xi - \xi_s, \eta - \eta_s, \Delta z - z_s)} = 1. \quad (3.24)$$

Step 3: The purpose of this step is to image each surface back into the detector plane. The data mark pattern in each surface is discretised into $\varphi = 2000$ independent point sources, which implies that the total number of point sources sampled is φN . There are two sets of calculations conducted in step 3. The first set is to derive the coordinates (x_l, y_l) and the irradiance $(I_d)_{l,j}$ of each point source's image on the detector plane, where $1 < l < \varphi$.

The geometry is shown in Fig. 3.9. The second set is to calculate the point spread function (PSF_j) of each surface.

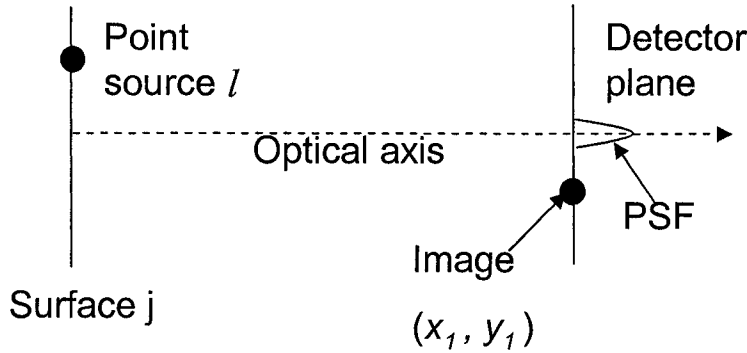


Figure 3.9 Illustration of step 3 for calculating the readout signal from fluorescent marks with OPTISCAN.

Step 4: The final step is to calculate the readout signal from the detector, where

$$i_q = \iint \left(\sum_{j=1}^N \left(\sum_{l=1}^{\phi} \left\{ (I_d)_{l,j} \delta(x_1 - x_{1,l,j}, y_1 - y_{1,l,j}) \right\} ** PSF_j \right) \right) D(x_1, y_1) dx_1 dy_1, \quad (3.25)$$

where l and j are the indices of the point sources and the surfaces, respectively.

Figures 3.10 (a) and (b) show contours of inter-layer crosstalk level versus ΔL and Δb for non-confocal and confocal systems, respectively. The shaded area in Fig. 3.10(b) indicates a relatively large region of operation. Figure 3.10(a) does not exhibit acceptable crosstalk levels until $\Delta b = 4.5 \mu\text{m}$ ($T_z = 5.4 \mu\text{m}$) at $\Delta L = 0.45 \mu\text{m}$. Figures 3.10(a) and 3.10(b) show that the confocal system significantly reduces the inter-layer crosstalk level as compared to the non-confocal system. For example, when the laser beam is focused to the center of the marks in layer 2 ($\Delta L = 0.45 \mu\text{m}$) and the layer-to-layer distance Δb is $\Delta b = 2.5 \mu\text{m}$ ($T_z = 3.4 \mu\text{m}$), the interlayer crosstalk level is -30 dB

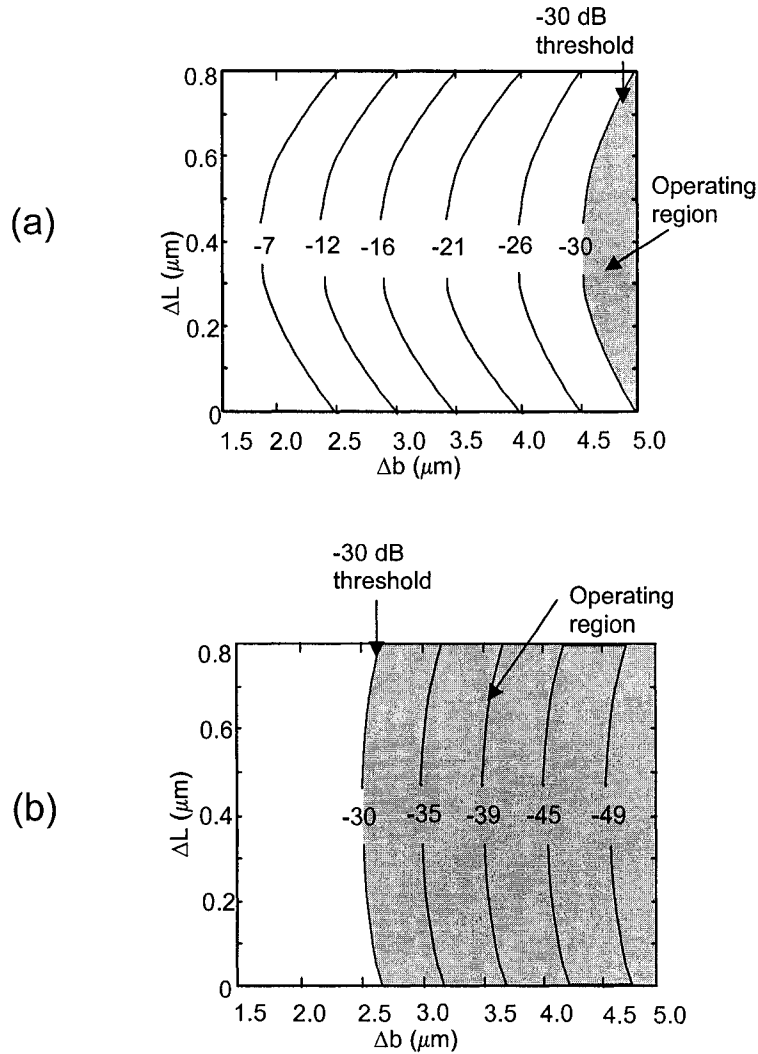


Figure 3.10 Contours of inter-layer crosstalk level X versus ΔL and Δb from Fig. 3.7 for (a) non-confocal systems and (b) confocal systems. The shaded area is the acceptable region of operation based on a -30 dB crosstalk criterion. The confocal system has the largest acceptable operating region.

for the confocal system, while the crosstalk level in a non-confocal system is -13 dB.

These simulations suggest that a confocal system can control the interlayer crosstalk level

to an acceptable level (-30 dB) when the layer-to-layer distance Δb is larger than $2.5 \mu\text{m}$ for the worst-case crosstalk condition.

Although the confocal system shows good crosstalk rejection, a compromise system with slightly higher v_d gives good crosstalk rejection and high CNR. Figure 3.11 shows the crosstalk level and CNR versus v_d when $\Delta L = 0.45 \mu\text{m}$ and $\Delta b = 3.5 \mu\text{m}$ ($T_z = 4.4 \mu\text{m}$, $\gamma = 1.66$). The crosstalk level, which is represented by a dashed line, increases as pinhole size increases, which is as expected. The CNR, which is represented by the solid line, increases dramatically as v_d increases from 1 to 3 and becomes saturated with further increase of v_d . The optimum value is $v_d = 3.5$, where CNR is just before saturation and crosstalk is -30 dB. A slight 0.8 dB reduction of CNR is realized with the optimum v_d . The black dots are the simulation results from 3D OTF model. Note that if data mark pattern with $\Delta b = 2.5 \mu\text{m}$ ($T_z = 3.4 \mu\text{m}$) is used, the optimum $v_d = 3.5$ can no longer limit the interlayer crosstalk X to be under -30 dB.

Inter-layer crosstalk level is also calculated for a near-field system using a hemispherical solid immersion lens (SIL) lens, as shown in Fig. 3.12. The refractive index of the SIL is $n_{SIL} = 2$, which exhibits $NA_{SIL} = 1.2$ when combined with a $NA = 0.6$ far-field system. For the purpose of this calculation, refractive index of the storage layer is set to equal to n_{SIL} . Rectangular marks in layers 1 and 3 have $L_\xi = L_\eta = 0.5 \mu\text{m}$ with 50% duty cycle ($T_\xi = T_\eta = 1 \mu\text{m}$). Marks in layer 2 have $L_\xi = L_\eta = 0.25 \mu\text{m}$ with 50% duty cycle ($T_\xi = T_\eta = 0.5 \mu\text{m}$). For all layers, $L_z = 0.44 \mu\text{m}$. The laser beam is focused to the

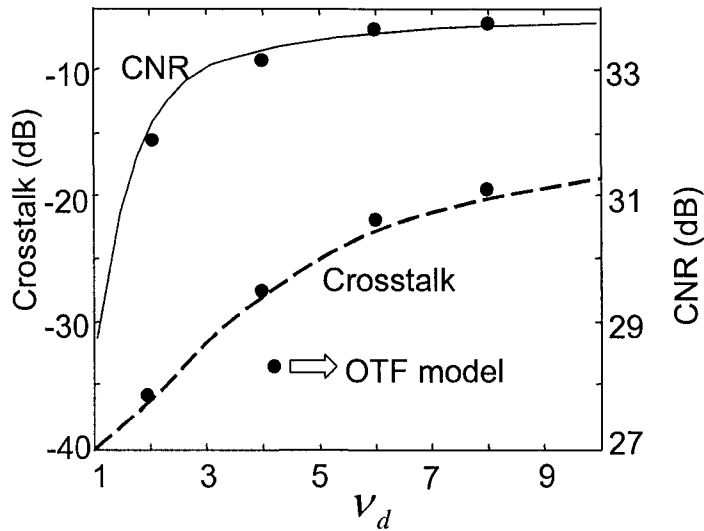


Figure 3.11 Simulation results from OPTISCAN when $T_z = 4.4 \mu\text{m}$. The solid line is CNR versus ν_d , the dashed line is inter-layer crosstalk versus ν_d . Black dots are simulation results from the 3D OTF model.

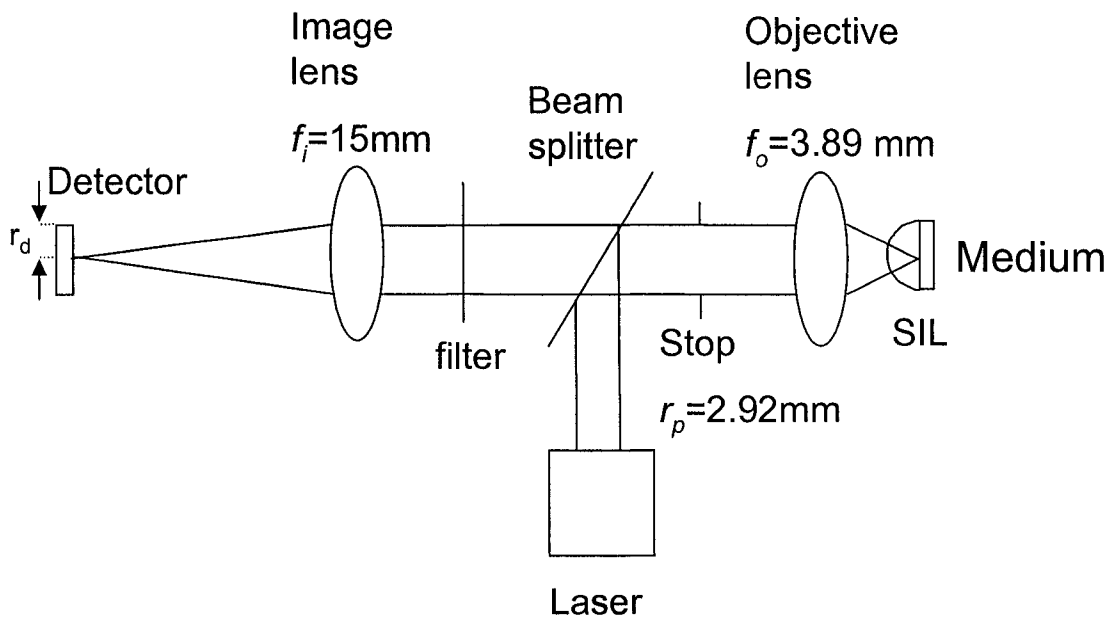


Figure 3.12 A near-field system used in the crosstalk study, which has a solid immersion lens (SIL) in proximity to the data layers. The radius of the SIL is 1.0 mm.

center of the bits in layer 2 ($\Delta L = 0.22 \mu\text{m}$). For the confocal system ($\nu_d = 0.9$), results indicate that the crosstalk level is lower than -30 dB when $T_z = 1.19 \mu\text{m}$. For a non-confocal system ($\nu_d = 8$), results indicate that acceptable crosstalk levels are achieved when $T_z = 2.20 \mu\text{m}$.

3.2.3 Comparing simulation results

Both 3D OTF and OPTISCAN techniques predict that the spacing between data layers must be increased beyond the depth of focus in order to limit crosstalk to under -30 dB. In a far-field system with $\text{NA}=0.6$, both simulation tools suggest that a confocal microscope reduces the worst case inter-layer crosstalk X to -30 dB when $\gamma=1.3$. On the other hand, the crosstalk in a non-confocal system achieves $X = -30$ dB when $\gamma = 2.1$. The inter-layer crosstalk is also calculated in a $\text{NA}=1.2$ near-field system with OPTISCAN. Results indicate that $X < -30$ dB when $\gamma = 1.35$ in a confocal system and $\gamma = 2.14$ in a non-confocal system.

Overall, 3D OTF and OPTISCAN provide similar simulation results over interlayer crosstalk and CNR of a far-field system. However, 3D OTF can not be applied to a near-field system because of its vector nature. Another advantage of OPTISCAN is that the simulation time is much shorter than with 3D OTF. To calculate a particular optical system with a specific data mark structure, it takes up to 6 hours with 3D OTF. In OPTISCAN it only takes 20 minutes. Hence, OPTISCAN is a more efficient method to simulate a fluorescent volumetric bit-wise optical system.

3.3 Simulation of inter-layer crosstalk in an optical system using Super-Rens material

Super-Rens material is made of a thin-film stack. A single piece of material has four layers, as shown in Fig. 3.13. The first layer and the third layer are ZnS-SiO₂ with $n = 2.1$ and the second layer is AgO_x with $n = 2.92 + 1.27i$ at $\lambda = 0.638\mu\text{m}$. The substrate layer is plastic with $n = 1.6$. The transmission of this material is calculated by OPTISCAN and optimized towards the highest transmission possible (78%) by varying the thickness of each layer. The optimum thicknesses of the 1st, 2nd, 3rd layers are 70 nm, 10 nm, and 80 nm, respectively. High transmission means that an optical disk made of Super-Rens material can have more data layers, because power can penetrate deeper.

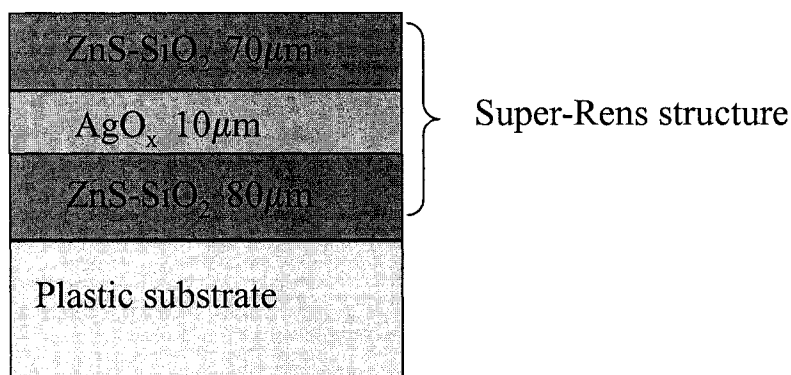


Figure 3.13 A single piece of thin film with Super-Rens structure.

It takes three steps to calculate the readout signal for a given data mark pattern in an optical system using Super-Rens material.

Step 1: OPTISCAN is used to calculate the electrical field distribution on a “source” plane that is 150 nm above the data mark.

Step 2: An FDTD program is used to simulate the interaction between the laser beam and the data marks. The electrical field distribution derived in step 1 is used as the source. The purpose of this step is to simulate the electrical distribution of the reflected beam by the data mark pattern on the source plane.

Step 3: OPTISCAN is used to propagate the reflected beam back to the imaging plane and calculate the readout signal. The optical system used in this section is the same as the system used in Fig. 3.3.

Figure 3.14 (a) shows mark patterns used to simulate inter-layer crosstalk. Rectangular marks in layers 1 and 3 have $L_{\xi} = L_{\eta} = 1\mu\text{m}$, with 50% duty cycle ($T_{\xi} = T_{\eta} = 2\mu\text{m}$). Marks in layer 2 have $L_{\xi} = L_{\eta} = 0.5\mu\text{m}$ with 50% duty cycle ($T_{\xi} = T_{\eta} = 1\mu\text{m}$). The enlarged view of a data mark is shown in Fig. 3.14 (b). Notice that there is an air bubble formed in the medium, which is due to the melting effect of the plastic substrate. As the laser beam is focused on the Super-Rens thin film, the AgOx layer is decomposed into Ag and oxygen molecules, which absorb photons, generate a large amount of heat and increase the local temperature to over 400 C. Hence, the substrate layer is melted and forms an air bubble [Kikukawa *et al.* 2003]. The depth of each mark is 100 nm.

Simulation results show that inter-layer crosstalk is -33 dB when $T_z = 3.9\mu\text{m}$ ($\gamma = 1.37$) for a confocal system. The inter-layer crosstalk increases to -10 dB for a

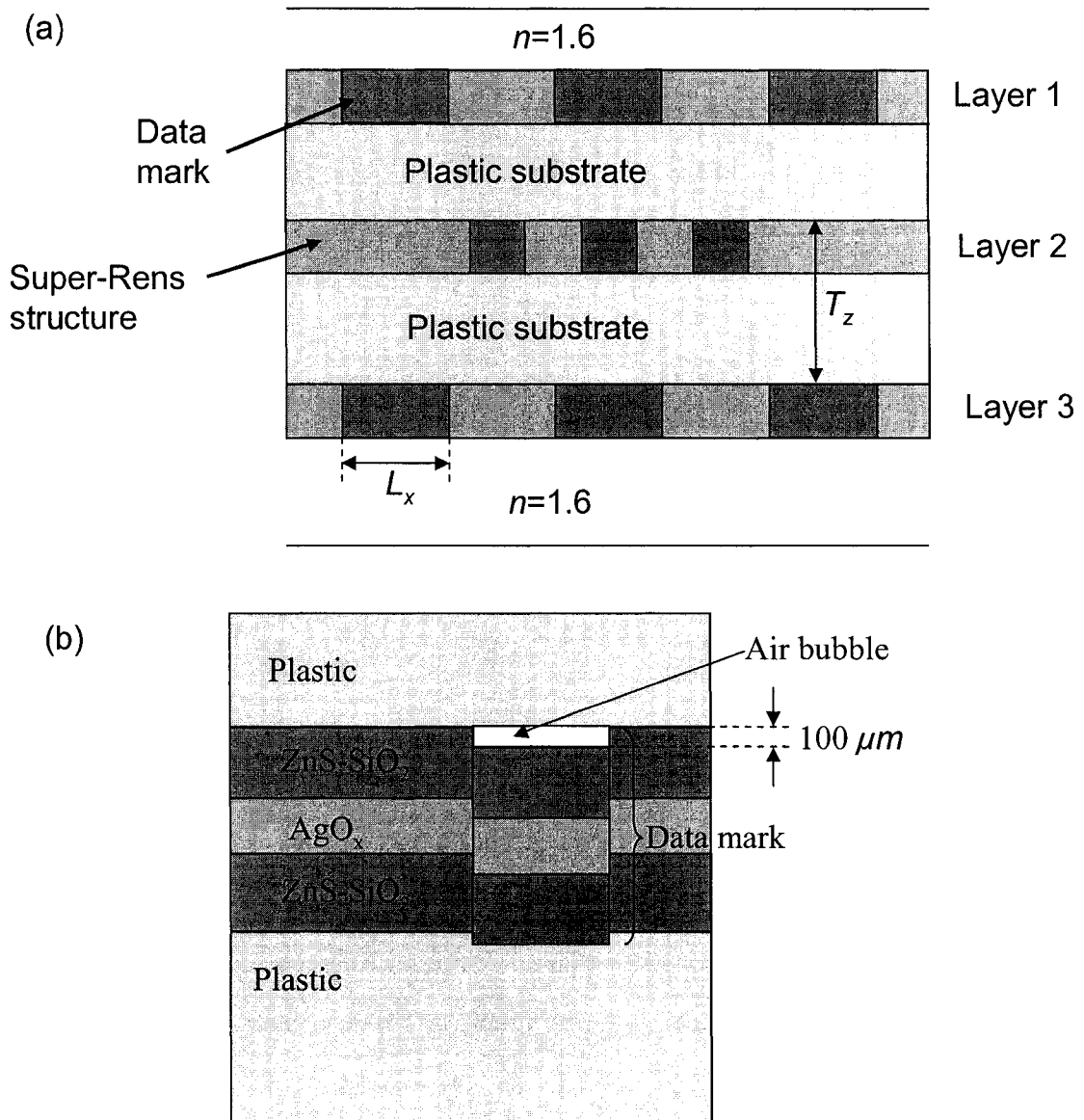


Figure 3.14 (a) The data mark pattern used in inter-layer crosstalk study for a Super-Rens material. (b) A detailed view of the data mark.

non-confocal system at the same T_z . The simulation time for each T_z is 24 hours, due to the extraordinary large three dimensional matrix ($300 \times 300 \times 500$) used in the FDTD program. The computer memory limits precluded using T_z larger than $3.9 \mu\text{m}$. As a result, the T_z could not be derived for an non-confocal system where $X < -30 \text{ dB}$. Therefore, only one data set is derived for this study.

3.4 Summary

The simulations in this chapter suggest that a confocal system reduces inter-layer crosstalk to under -30 dB for both far-field and near-field systems that use fluorescent or Super-Rens materials if $\gamma \sim 1.35$. This specific value of γ is significant, because it is used to evaluate the maximum storage capability of far-field and near-field systems in Chapter 5. For non-confocal systems, $\gamma \sim 2.1$ leads to similar crosstalk performance. OPTISCAN also predicts that the optimum design point for a far-field system is $\nu_d = 3.5$ and $\gamma = 1.66$, where the inter-layer crosstalk is below -30 dB and the penalty on the CNR is less than 1 dB .

Chapter 4

LENS DESIGN

This chapter presents far-field and near-field optical systems with proper spherical aberration compensation for volumetric bit-wise optical data storage.

4.1 Far-field system with proper spherical aberration compensator

The configuration of an optical system for volumetric bit-wise optical data storage technology is similar to conventional disk systems, in that a spinning disk is illuminated by a laser beam that is focused into the disk by an objective lens. Data are recorded and read out as mark patterns in spiral tracks. The objective lens moves on an actuator that responds to servo signals in order to keep the focused beam aligned correctly on the data. A significant difference between conventional recording and bit-wise volumetric recording is that many more layers are accessed in volumetric systems. Especially in a system using a fluorescent medium, the number of possible data layers is in the hundreds. As shown in Fig. 4.1, a laser beam focuses through the substrate to access different data layers. A basic requirement of an optical system used in volumetric storage is that the focused laser spot size on each layer must be as small as possible to maximize data capacity.

The typical simple aspheric lens used for single-layer optical data storage systems forms a focus spot with diffraction limited size in a data layer at one pre-designed depth. These lenses are convenient, because they are inexpensive and can be used with conventional actuators. If this type of lens is used for bit-wise volumetric recording,

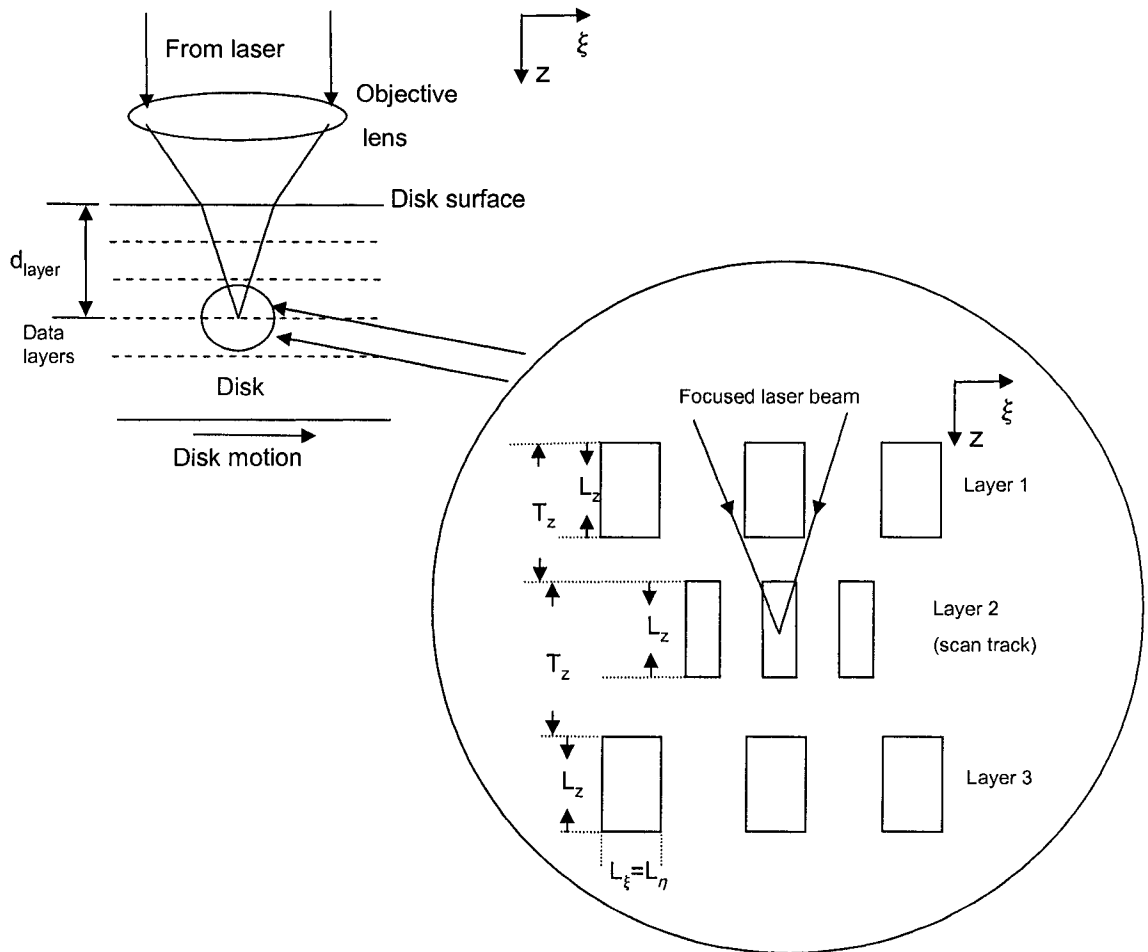


Figure 4.1 A typical fluorescent volumetric read out system. The incident laser beam is focused by an objective lens onto a bit plane of interest at depth d_{layer} below the top surface. The distance between marks in the same bit plane is T_ξ , while the distance between two planes of data marks is T_z .

spherical aberration is generated as the focus moves through different layers inside the recording medium. Since multiple layers in the medium are treated as stacked plane

parallel plates, shifting focus from one layer to another induces spherical aberration ΔW_{040} in the form

$$\Delta W_{040} = -\frac{1}{8} \times \left[\frac{n^2 - 1}{n^3} \right] \times NA^4 \times \Delta t_z, \quad (4.1)$$

where n is the refractive index of the medium, NA is the numerical aperture in the medium and Δt_z is the change in thickness from the compensated design depth. Spherical aberration increases the focused spot size, spreads energy out from the center of the focus spot and reduces read-out signal amplitude. Thus, a spherical-aberration compensator must be designed to work with the objective lens for reading multiple layers and maintaining a high NA over the entire multiple-layer thickness range $(\Delta t_z)_{\max}$.

Milster [Milster et al. 1999] first investigated a number of aberration compensation systems, which include an afocal variable plate, a Cook afocal triplet, a Keplerian telescope and a Galilean telescope, to use with volumetric optical data storage. He pointed out that a Burch-type objective lens in conjunction with a Galilean telescope is a compact, simple and effective optical system for spherical aberration compensation. Therefore, a Galilean telescope compensator combined with a custom designed Burch-type aspheric plastic objective lens is designed as an example far-field volumetric read-out system in this study. Figure 4.2 shows a layout of this system. Optical design parameters are shown in Table 4.1 for the system that operates at $\lambda=0.633 \mu\text{m}$. The length between the first surface of element 1 and the last surface of element 3 is less than 10 mm and maximum field angle is 0.5 degree with $NA=0.6$. After changing d_{focus} for moving focus d_{layer} through media layers, d_{comp} is adjusted for the purpose of spherical aberration

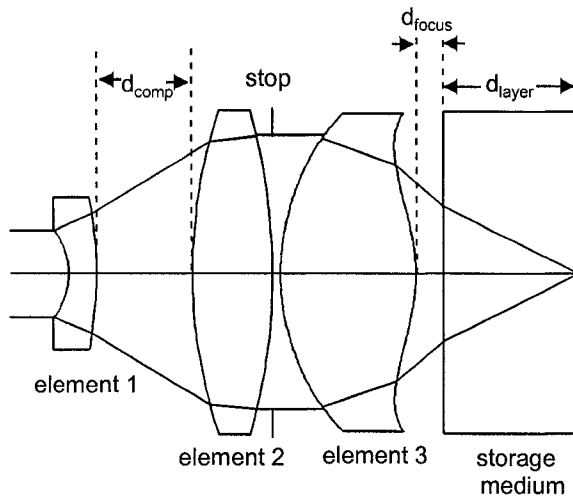


Figure 4.2 Layout of a far-field system designed for optimum compensation through volumetric media. The lens elements extend over a track length of only 13mm. d_{focus} is adjusted to change data layers, and d_{comp} is changed to adjust for spherical aberration.

compensation. For example, the laser beam is focused deeper into the disk by reducing d_{focus} and increasing d_{layer} . Increased spherical aberration ΔW_{040} with a “-” sign is introduced by focusing deeper in the medium.

Table 4.1 Optical design parameters of the far-field system in Fig. 4.2 that operates at $\lambda=0.633 \mu\text{m}$ at $\Delta t_z = 4.1\text{mm}$

Surface	Type	Radius	Thickness	Glass	Conic
OBJ	STANDARD	Infinity	Infinity		
1	STANDARD	Infinity	0.2		
2	STANDARD	-1.385551	0.7	SF10	
3	STANDARD	-7.957968	2.624683		
4	STANDARD	9.91889	2	SF57	
5	STANDARD	-11.7864	0		
STO	STANDARD	Infinity	0.2		
7	EVENASPH	4.501521	3.4	C0550	-0.1341
8	EVENASPH	-3.235285	0.07768		-4.7268
9	STANDARD	Infinity	4.1	PMMA	
IMA	STANDARD	Infinity			

Surface	r_4	r_6	r_8	r_{10}
7	-0.00099111714	3.0686849×10^{-5}	$-1.8866261 \times 10^{-6}$	3.8152078×10^{-7}
8	0.0054264972	-0.00037332693	3.9292464×10^{-5}	-5.794158×10^{-7}

To balance this excessive spherical aberration, d_{comp} is increased so that the object conjugate of the objective lens is changed. As a result, spherical aberration with a “+” sign from the second surface of the objective lens is increased significantly, so that the

overall system spherical aberration is maintained at the minimal level. The relations of d_{focus} and d_{comp} versus d_{layer} are shown in Fig.4.3. Note that d_{focus} decreases from left to right. This study indicates that there is 4.2 mm allowable $(\Delta t_z)_{\text{max}}$, which is calculated by $(\Delta t_z)_{\text{max}} = (d_{\text{layer}})_{\text{max}} - (d_{\text{layer}})_{\text{min}}$, with Strehl ratio higher than 90% and less than 0.05 wave rms wave-front aberration error. The theoretical calculation in Eq. (4.1), which is verified with a commercial lens design package, shows that this design compensates up to $(\Delta W_{040})_{\text{max}} = 36$ waves of spherical aberration. Further tolerance study shows that this design provides 4.2 mm allowable $(\Delta t_z)_{\text{max}}$ between $\lambda = 0.618 \mu\text{m}$ and $\lambda = 0.648 \mu\text{m}$.

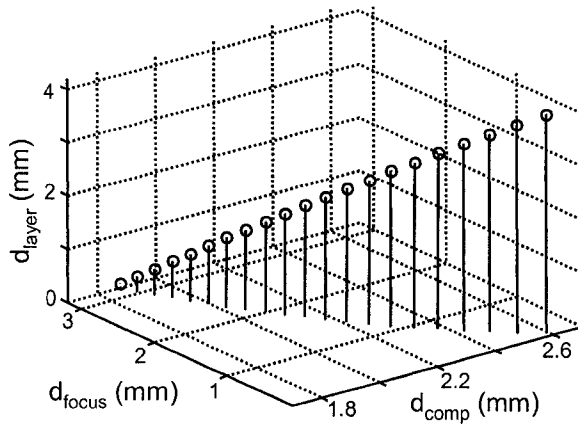


Figure 4.3 The relations of d_{focus} and d_{comp} versus d_{layer} for far-field system .

4.2 Near-field system with proper spherical aberration compensator

Ultra-high density near-field systems that use a solid immersion lens (SIL) are investigated in this section. A SIL uses a high refractive index element in proximity to the top surface of the disk substrate. Evanescent coupling between the element and the substrate allows for $NA = n \sin \theta$ to be greater than one [Mansfield *et al.* 1990]. The first surface of the SIL is usually spherical, and the second surface is flat. An objective lens focuses the laser beam into the SIL. The curved surface of the SIL can be used to introduce additional optical power into the focused beam and increase NA as the SIL moves closer to objective lens.

Figure 4.4 shows the spherical aberration contributed by the curved surface of a SIL with radius r versus the coordinate l of the axial intercept of a marginal ray focused from a fixed NA far-field objective lens, as the SIL vertex moves closer to the objective. The NA increases as l increases, because of the corresponding increase in the marginal ray angle θ . Several special characteristic points are indicated. Point O at $l_o = 0$ corresponds to the focus of the far-field objective lens reflecting from the SIL vertex. Point A corresponds to the condition of a hemispherical SIL, where $l_A - l_o = r$. Spherical aberration is zero when the marginal ray intersects the optical axis at points O, A and B. The spherical aberration is positive, i.e. overcorrected, when the marginal ray intersects the optical axis between point O and point B. The spherical aberration is negative, i.e. under corrected, when the marginal ray intersects the optical axis out of that range. Point A is the hemi-spherical aplanatic point, and point B is the hyper-spherical aplanatic point. Figure 4.4 suggests that point A is a stable point, because small focus shifts of l around

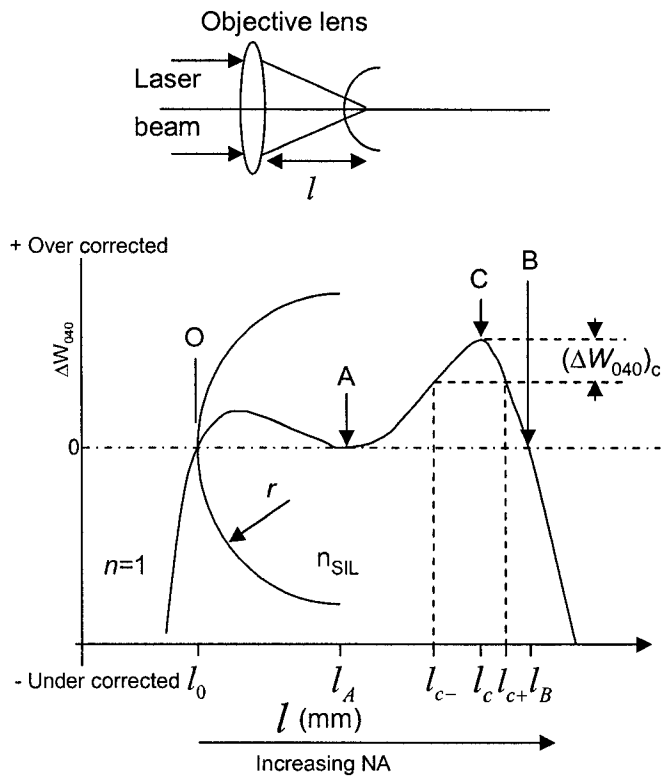


Figure 4.4 Spherical aberration SA of a focused beam inside a SIL. A and B are aplanatic points. C and A are stable points versus focus . Point O corresponds to the objective lens reflecting from the SIL vertex. Point A is the hemi-spherical condition, and point B is the hyper-spherical aplanatic condition.

point A generate only a small amount of ΔW_{040} . Point B is an unstable point, because small focus shifts around point B generate a large amount of ΔW_{040} . Point C is also an interesting point, because it's a stable point and has a relatively large NA. Three near-field system designs with compensation for ΔW_{040} at points A, B and C are discussed in the following paragraphs. The SIL refractive index n_{SIL} and the medium refractive index n are 1.5 in all three designs. The radius of the SIL is $r = 0.96\text{mm}$. All three near-field

systems are designed at $\lambda=0.633\mu\text{m}$ and they have the same spherical aberration compensation mechanism as the far-field system.

Near-Field System I, which is compensated at point A with $\text{NA}=1.0$, is shown in Fig. 4.5. Optical design parameters are shown in Table 4.2. The maximum field angle is 0.2 degree. Lens elements 1,2,3 and 4 have aspherical departures on both lens surfaces. Lens elements 2 and 4 are inversely symmetric. The system stop is set in front of lens element 1. The induced spherical aberration versus $\Delta t_z = d_{\text{layer}} - l_A$ is

$$\Delta W_{040} = -\frac{1}{8r} \times \frac{n_{\text{SIL}} - 1}{n_{\text{SIL}}^3} \text{NA}^4 \Delta t_z^2. \quad (4.2)$$

$(\Delta t_z)_{\text{max}}$ is 0.100mm with Strehl ratio higher than 90%, which corresponds to

$(\Delta W_{040})_{\text{max}} = 0.2$ wave between $\lambda=0.623\mu\text{m}$ and $\lambda=0.643\mu\text{m}$.

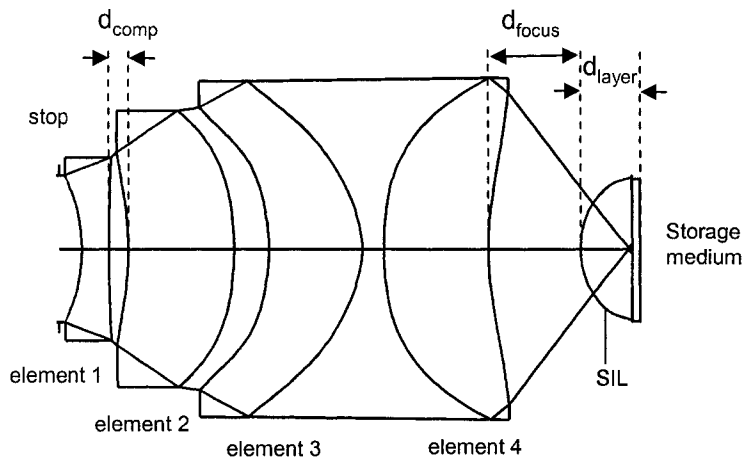


Figure 4.5 Layout of Near-Field System I.

Near-Field System II is shown in Fig. 4.6 and is compensated at point B in Fig. 4.4 with $NA=1.35$. The maximum field angle is 0.15 degree. Optical design parameters are shown in Table 4.3. The induced spherical aberration versus $\Delta t_z = d_{layer} - l_B$ is

$$\Delta W_{040} = -\frac{1}{8} \times (n_{SIL}^2 - 1) \frac{NA^4}{n_{SIL}^2} \Delta t_z. \quad (4.3)$$

$(\Delta t_z)_{\max}$ is 0.026 mm with Strehl ratio higher than 90%, which corresponds to

$(\Delta W_{040})_{\max} = 10.1$ wave between $\lambda=0.623 \mu\text{m}$ and $\lambda=0.643 \mu\text{m}$.

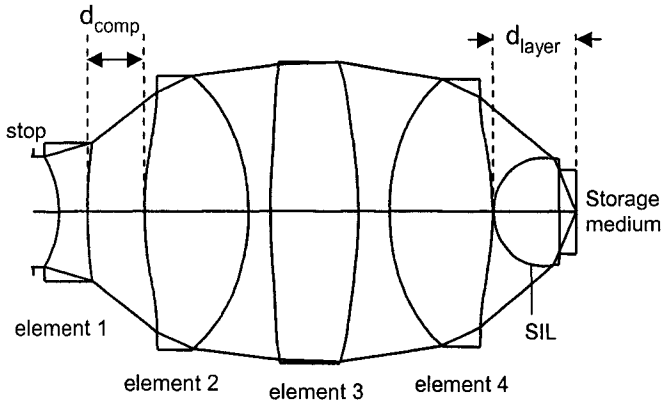


Figure 4.6 Layout of Near-Field System II.

Near-Field System III is shown in Fig 4.7 and is compensated at point C, which is a stable point in Fig. 6, with $NA=1.2$. Optical design parameters are shown in Table 4.4. Maximum off-axis field angle of this system is 0.2 degree. This design exhibits $(\Delta t_z)_{\max} = 0.170 \text{ mm}$ allowable focus depth with 90% or higher Strhel ratio between $\lambda=0.623 \mu\text{m}$ and $\lambda=0.643 \mu\text{m}$. The spherical aberration that this design compensates is

5.1 waves to the left side of point C and 2.5 waves to the right side of point C. Note that point C has relatively large NA compared to Near-Field System I.

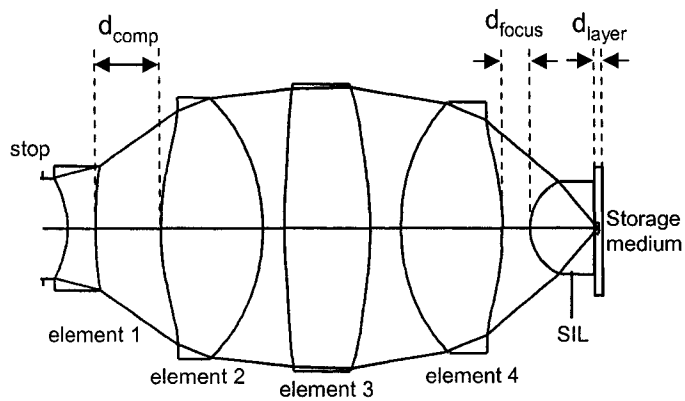


Figure 4.7 Layout of Near-Field System III.

Table 4.2 Optical design parameters of Near-Field System I in Fig. 4.5 that operates at $\lambda=0.633 \mu\text{m}$.

Surface	Type	Radius	Thickness	Glass	Conic
OBJ	STANDARD	Infinity	Infinity		
STO	STANDARD	Infinity	0.436621		
2	STANDARD	-1.724415	0.5	SF4	
3	STANDARD	17.0696	0.3615761		
4	EVENASPH	-3.117136	1.946706	PMMA	
5	EVENASPH	-3.507084	0.6442158		
6	EVENASPH	-1.639577	1.719748	PMMA	-20.15102
7	EVENASPH	-1.054532	0.4055705		2.583878
8	EVENASPH	3.507084	1.946706	PMMA	
9	EVENASPH	3.117136	1.724239		
10	STANDARD	0.96	0.95721	PMMA	
11	STANDARD	Infinity	-0.05	PMMA	
IMA	STANDARD	Infinity		PMMA	
Surface	r_4	r_6	r_8	r_{10}	
4	0.024768544	0.00088642318	-0.00049536305	4.3225412×10^{-5}	
5	-0.04144622	0.00031740088	0.00027738219	-3.998413×10^{-5}	
6	-0.059286857	-0.038141128	0.013879831	-0.001114246	
7	-0.03845067	0.0002128405	-0.0003948273	0.00012359609	
8	0.04144622	-0.00031740088	-0.00027738219	3.998413×10^{-5}	
9	-0.024768544	-0.00088642318	0.00049536305	$-4.3225412 \times 10^{-5}$	

Table 4.3 Optical design parameters of Near-Field System II in Fig. 4.6 that operates at $\lambda=0.633 \mu\text{m}$.

Surface	Type	Radius	Thickness	Glass	Conic
OBJ	STANDARD	Infinity	Infinity		
STO	STANDARD	Infinity	0.5		
2	STANDARD	-1.806746	0.5622477	SF4	
3	STANDARD	8.046298	1.097734		
4	EVENASPH	5.384343	2	PMMA	
5	EVENASPH	-3.868936	0.4182243		
6	EVENASPH	8.583436	1.7	PMMA	-4.458775
7	EVENASPH	-6.571748	0.6043733		2.656727
8	EVENASPH	3.868936	2	PMMA	
9	EVENASPH	-5.384343	0.020510716		
10	STANDARD	0.96	1.27	PMMA	
11	STANDARD	Infinity	0.3335	PMMA	
IMA	STANDARD	Infinity		PMMA	

Surface	r_4	r_6	r_8	r_{10}
4	0.0054396649	-0.007185179	0.0012059849	-7.690353×10^{-5}
5	-0.0064162015	0.00019737317	-0.00010005878	6.377195×10^{-6}
6	-0.012463713	0.0013251151	3.5573002×10^{-5}	-7.755043×10^{-6}
7	0.0099062859	-0.0002499100	-8.559538×10^{-5}	5.1057472×10^{-6}
8	0.0064162015	-0.0001973731	0.00010005878	-6.377195×10^{-6}
9	-0.0054396649	0.007185179	-0.0012059849	7.690353×10^{-5}

Table 4.4 Optical design parameters of Near-Field System III in Fig. 4.6 that operates at $\lambda=0.633 \mu\text{m}$.

Surface	Type	Radius	Thickness	Glass	Conic
OBJ	STANDARD	Infinity	Infinity		
STO	STANDARD	Infinity	0.5		
2	STANDARD	-1.810848	0.5622477	SF4	
3	STANDARD	7.994613	1.285547		
4	EVENASPH	5.384343	2	PMMA	
5	EVENASPH	-3.868936	0.4182243		
6	EVENASPH	8.583436	1.7	PMMA	-4.458775
7	EVENASPH	-6.571748	0.6043733		2.656727
8	EVENASPH	3.868936	2	PMMA	
9	EVENASPH	-5.384343	0.5459056		
10	STANDARD	0.96	1.27	PMMA	
11	STANDARD	Infinity	0.1	PMMA	
IMA	STANDARD	Infinity		PMMA	

Surface	r_4	r_6	r_8	r_{10}
4	0.010019999	-0.0067992243	0.0010274601	$-6.2771698 \times 10^{-5}$
5	-0.0046778397	0.00049029312	-9.382679×10^{-5}	6.0356394×10^{-6}
6	-0.012463713	0.0013251151	3.5573002×10^{-5}	-7.755043×10^{-6}
7	0.0099062859	-0.0002499100	-8.559538×10^{-5}	5.1057472×10^{-6}
8	0.0046778397	-0.0004902931	9.3826799×10^{-5}	$-6.0356394 \times 10^{-6}$
9	-0.010019999	0.0067992243	-0.0010274601	6.2771698×10^{-5}

Figure 4.8 shows the compensation range for all three near-field designs. The darkened curves are the compensation ranges for Near-Field Systems I, II and III. $(\Delta t_z)_{\max}$ of System I is 0.100 mm, however it only corresponds to $(\Delta W_{040})_{\max} = 0.2$ wave. System II has a very limited $(\Delta t_z)_{\max} = 0.026$ mm, which leads to a surprisingly large $(\Delta W_{040})_{\max} = 10.1$ waves. Only System III provides the largest $(\Delta t_z)_{\max} = 0.170$ mm with moderate spherical aberration changes.

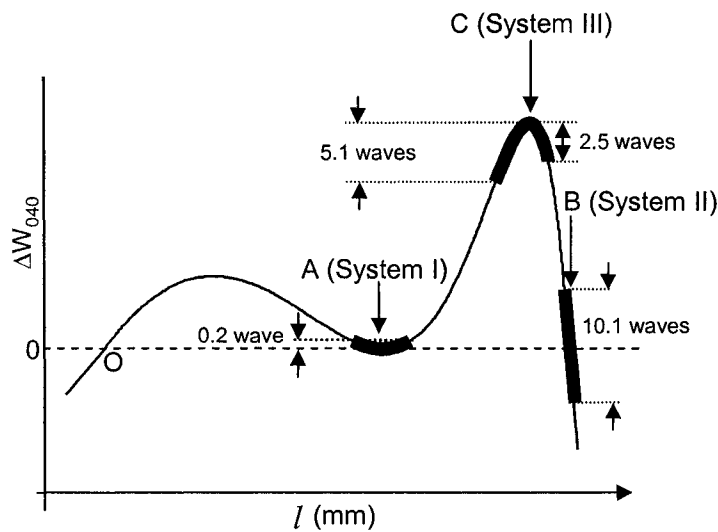


Figure 4.8 The spherical aberration compensation range for Near-Field System I, Near-Field System II and Near-Field System III.

Table 4.5 summarizes the important parameters of the far-field and near-field lens designs. There are several interesting observations that can be drawn from Table 4.5. The first one is that N is extremely large for the far-field system, which leads to its immense

storage capacity. The second one is that a very small $(\Delta t_z)_{\max} = 0.026 \text{ mm}$ in Near-Field System II leads to 10 waves of spherical aberration, which is a consequence of the unstable operating point. Finally, Near-Field System III has the largest $(\Delta t_z)_{\max}$ range among the three near-field designs and a relative large NA, hence it has the largest data capacity.

Table 4.5 Important parameters: NA, $(\Delta t_z)_{\max}$, $(\Delta W_{040})_{\max}/\lambda$, d_{focus} range, d_{comp} range and d_{layer} range for far-field system, Near-Field System I, Near-Field System II and Near-Field System III.

Optical System	NA	$(\Delta t_z)_{\max}$ (mm)	$(\Delta W_{040})_{\max}$ (wave)	d_{comp} range (mm)	d_{focus} range (mm)	d_{layer} range (mm)
Far-field system	0.6	4.2	36	0.7181	3.0184	4.200
Near-field System I	1	0.1	0.2	0.0337	0.1700	0.100
Near-field System II	1.35	0.026	10.1	0.1536	0.0323	0.026
Near-field System III	1.2	0.17	5	0.1548	0.5515	0.170

4.3 Far-field system versus Near-field system

The high NA of the near-field system gives it a significant advantage in the writing and reading process compared to the far-field system. Zhang [Zhang *et al.* 2004] demonstrated that the writing and reading efficiency is increased by 10 times and 5 times, respectively, when the NA is increased from 0.6 to 1.2. The peak power required in the writing process is reduced by 4 times if a near-field system is used. The increase in the writing and reading efficiency and the decrease of the peak power needed in the writing process are especially significant to the fluorescent medium, since the two-photon process associated with this material is slow in nature and needs a high power laser to write. Therefore, a much more compact and affordable laser may be used in the near-field system when the optical disk is made of a fluorescent medium.

4.4 Summary

Far-field and near-field systems that are designed for volumetric optical storage systems have different characteristics. The combination of a Galilean telescope spherical aberration compensator and a customized far-field aspherical objective lens achieves 4.2 mm compensation range in the recording material, which corresponds to 36 waves of spherical aberration. A practical lens design for this system is less than 13mm long. Three different designs for near-field systems are shown. The optimum design is achieved around point C in Fig. 4.4, which is between the hemispherical and hyper-spherical operating points. Overall, the optimum near-field system exhibits higher numerical

aperture and is more compact compared to the far-field system, except that compensation of ΔW_{040} is harder to achieve.

Chapter 5

EFFECTIVE SURFACE DENSITY

This chapter defines effective surface density and calculates maximum storage densities of the far-field and near-field systems. Sections 5.1 and 5.2 discuss maximum storage densities of far-field and near-field systems, respectively, under the assumption that there are no limitations in laser power focused through multiple layers. This assumption is accurate for fluorescent media, but may be inadequate for Super-Rens media. Section 5.3 summarizes these results. Section 5.4 discusses maximum storage densities with laser power constricts and absorption. Section 5.5 summaries overall results of this chapter.

5.1 Maximum storage density of a far-field system

A specific optical system operating over focus range $(\Delta t_z)_{\max}$ with layer spacing T_z has $N = (\Delta t_z)_{\max} / T_z$ layers that are processed throughout the volume. Since the optical system interfaces with the disk through the top surface, an effective surface density Π is defined as

$$\Pi = N / \text{mark surface area.} \quad (5.1)$$

Multiple layers in the medium are treated as stacked plane parallel plates. Hence, the induced spherical aberration ΔW_{040} by Δt_z is in the form

$$\Delta W_{040} = -\frac{1}{8} \times \left[\frac{n^2 - 1}{n^3} \right] \times NA^4 \times \Delta t_z, \quad (5.2)$$

where ΔW_{040} has unit of waves and Δt_z has unit of mm.

Assuming that the maximum spherical aberration that can be compensated is $(\Delta W_{040})_{\max}$,

$(\Delta t_z)_{\max}$ is given by

$$(\Delta t_z)_{\max} = N \times T_z = \frac{8(\Delta W_{040})_{\max} n^3}{(n^2 - 1)NA^4}. \quad (5.3)$$

Hence,

$$N = \frac{(\Delta t_z)_{\max}}{\gamma Z_f} = \frac{8(\Delta W_{040})_{\max} n^2}{\gamma \lambda (n^2 - 1) NA^2}, \quad (5.4)$$

where γ equals to 1.35 for both fluorescent material and Super-Rens material, as described in Chapter 3. Therefore, Π of a far-field read out system is

$$\Pi = \frac{1}{2L_x \times 2L_y} N = \frac{N}{s^2} = \frac{8(\Delta W_{040})_{\max} n^2}{\gamma \lambda^3 (n^2 - 1)} \text{ Gb/in}^2, \quad (5.5)$$

where λ has unit of μm . Notice that Eq. (5.5) is not a function of NA. That is, the effective surface density of a far-field volumetric system is, to first order, not a function of NA. Equation (5.5) assumes that there is no limitation to the laser power as it focuses through multiple layers. This assumption is accurate for media that exhibit low absorption, like fluorescent media.

Figure 5.1 shows the theoretical effective surface density of far-field read out systems versus refractive index of the storage medium, assuming that the system compensates 2, 10 and 20 waves of spherical aberration in Eq. (5.2). Surprisingly, media with higher refractive index exhibit less effective surface density. This result occurs

because Π in Eq. (5.2) is proportional to $\frac{n^2}{n^2 - 1}$, which decreases as n increases. The

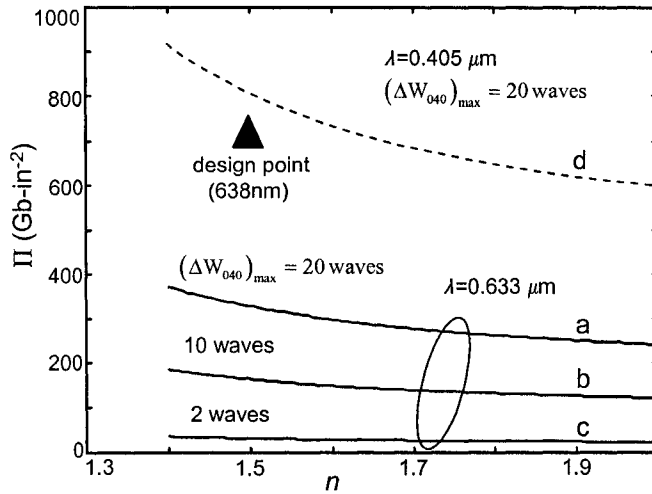


Figure 5.1 Effective surface density Π of a far-field read-out system versus medium refractive index when (a) $\lambda=0.633 \mu\text{m}$, $(\Delta W_{040})_{\text{max}} = 20$ waves; (b) $\lambda=0.633 \mu\text{m}$, $(\Delta W_{040})_{\text{max}} = 10$ waves; (c) $\lambda=0.633 \mu\text{m}$, $(\Delta W_{040})_{\text{max}} = 2$ waves; and (d) $\lambda=0.405 \mu\text{m}$, $(\Delta W_{040})_{\text{max}} = 20$ waves. At the design point, $\lambda=0.633 \mu\text{m}$, $NA=0.6$ and $(\Delta W_{040})_{\text{max}} = 36$ waves.

particular system design shown in Fig.4.2 ($\lambda=0.633 \mu\text{m}$ and $(\Delta W_{040})_{\text{max}} = 36$ waves) exhibits 718 Gb-in^{-2} with 1233 layers based on this calculation. Also, Fig. 5.1 shows theoretical results for $\lambda=0.405 \mu\text{m}$, which indicate maximum Π of 800 Gb-in^{-2} when $(\Delta W_{040})_{\text{max}} = 20$ waves and $n = 1.5$.

5.2 Maximum storage density of a near-field system

Near-Field System I is compensated at Point A in Fig. 4.4 with $NA=1.0$, as described in Chapter 4. The induced spherical aberration versus $\Delta t_z = d_{\text{layer}} - l_A$ is

$$\Delta W_{040} = -\frac{1}{8r} \times \frac{n_{SIL} - 1}{n_{SIL}^3} NA^4 \Delta t_z^2, \quad (5.6)$$

where $(\Delta t_z)_{\max} = 0.1$ mm with Strehl ratio higher than 90%, which corresponds to $(\Delta W_{040})_{\max} = 0.2$ wave between $\lambda = 0.623 \mu\text{m}$ and $\lambda = 0.643 \mu\text{m}$.

Following the same discussion as for the far-field system, the theoretical maximum surface density for Near-Field System I is

$$\Pi = \frac{N_{\max}}{s^2} = \frac{NA^2}{\gamma \lambda^3} \sqrt{8 \frac{n_{SIL} r}{n_{SIL} - 1} (\Delta W_{040})_{\max}}, \quad (5.7)$$

where r has unit of mm. Figure 5.2 shows a contour map of Π versus n and $\sin\theta$ for $(\Delta W_{040})_{\max} = 0.2$ wave at $\lambda = 0.623 \mu\text{m}$. Hence, for an ordinary SIL with refractive index of 2, System I achieves $\Pi = 100\text{-}300 \text{ Gb-in}^{-2}$. The particular system design shown in Fig. 4.5 exhibits 132 Gb-in^{-2} , based on this calculation at $\lambda = 0.633 \mu\text{m}$ with 81 layers. The surface density can be further increased to 400 Gb-in^{-2} if the system is redesigned for a $\lambda = 0.405 \mu\text{m}$ laser.

Near-Field System II is compensated at Point B in Fig. 4.4 with $NA = 1.35$, as described in Chapter 4. The induced spherical aberration versus $\Delta t_z = d_{\text{layer}} - l_B$ is

$$\Delta W_{040} = -\frac{1}{8} \times (n_{SIL}^2 - 1) \frac{NA^4}{n_{SIL}^2} \Delta t_z, \quad (5.8)$$

where $(\Delta t_z)_{\max} = 0.026$ mm with Strehl ratio higher than 90%, which corresponds to $(\Delta W_{040})_{\max} = 10.1$ waves between $\lambda = 0.623 \mu\text{m}$ and $\lambda = 0.643 \mu\text{m}$. The theoretical maximum surface density for System II is

$$\Pi = \frac{N_{\max}}{s^2} = \frac{8(\Delta W_{040})_{\max} n_{SIL}}{\gamma(n_{SIL}^2 - 1)\lambda^3}, \quad (5.9)$$

which, like the far-field system, is not a function of NA. Π versus n is shown in Fig. 5.3 for $(\Delta W_{040})_{\max} = 10.1$ waves. The particular system design shown in Fig. 4.6 exhibits 113 Gb-in⁻² based on this calculation at $\lambda = 0.633 \mu\text{m}$ with 39 layers. The surface density can be further increased to by 280 Gb-in⁻² if the system is redesigned for a $\lambda = 0.405 \mu\text{m}$ laser.

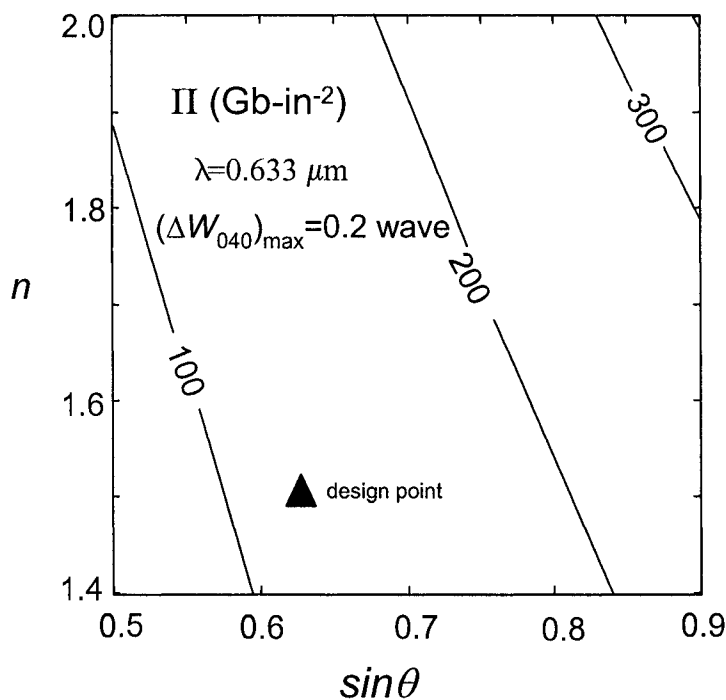


Figure 5.2 Contour map of Π of Near-field System I versus sine of the marginal ray angle $\sin\theta$ and medium refractive index n

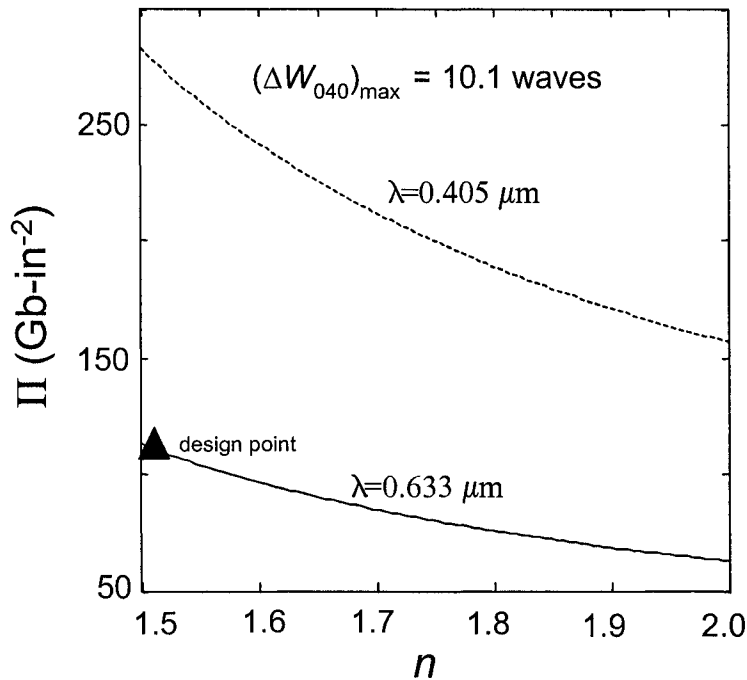


Figure 5.3 Effective surface density Π of Near-field System II versus medium refractive index n when $\lambda=0.633 \mu\text{m}$ and $\lambda=0.405 \mu\text{m}$.

Near-Field System III is compensated at Point C in Fig. 4.4 with $\text{NA}=1.2$, as described in Chapter 4. Numerical calculations are performed to determine Π of System III. The first step is to find the exact coordinates of Point C numerically, which is designated as l_c . The second step is to find the coordinates l_{c+} and l_{c-} as labeled on Fig. 4.4, where the change in ΔW_{040} from point l_c to l_{c+} is set to be 2.5 waves and from l_c to point l_{c-} is set to be 5.1 waves. These solutions are found numerically using the lens design associated with Fig. 4.7. $(\Delta t_z)_{\text{max}}$ of Near-Field System III is

$$(\Delta t_z)_{\max} = |l_{c+} - l_c| + |l_{c-} - l_c|. \quad (5.10)$$

The maximum surface density Π is calculated and presented in Fig. 5.4 for $n_{SIL} = 1.5$ or 2.0 and $\lambda = 0.633 \mu\text{m}$ or $0.405 \mu\text{m}$. When $\lambda = 0.633 \mu\text{m}$, the maximum surface density reaches 510 Gb-in^{-2} for $n_{SIL} = 1.5$ at $\text{NA} = 1.5$. If $n_{SIL} = 2$, Π reaches 1250 Gb-in^{-2} at $\text{NA} = 2$. However, optical systems for which $\text{NA} = 2$ require exceptional lens design. When $\lambda = 0.405 \mu\text{m}$, the maximum surface density can reach 1750 Gb-in^{-2} for $n_{SIL} = 1.5$ at $\text{NA} = 1.5$. If $n_{SIL} = 2$, Π reaches 3650 Gb-in^{-2} at $\text{NA} = 2$. For a moderately complex system, like $\text{NA} = 1.2$ and $n_{SIL} = 1.5$, Π is 1.65 Tb-in^{-2} ($1 \text{ Tb-in}^{-2} = 1000 \text{ Gb-in}^{-2}$) at $\lambda = 0.405 \mu\text{m}$. The design point for the system ($\lambda = 0.633 \mu\text{m}$ $\text{NA} = 1.2$) pictured in Fig. 4.7 is shown on Fig. 5.4 and exhibits $\Pi = 470 \text{ Gb-in}^{-2}$ with 200 layers. Notice that, in Fig. 5.4, the SIL with $n_{SIL} = 2$ reaches higher surface density, because it produces higher NA. The other interesting feature is that Π is dramatically increased by switching to a blue laser diode ($\lambda = 0.405 \mu\text{m}$).

5.3 Summary of effective surface density calculations for media with low absorption.

Table 5.1 summarizes the important parameters of the far-field and near-field systems in Sections 5.1 and 5.2. There are two interesting observations that can be drawn from Table 5.1. The first one is that N is extremely large for the far-field system, which leads to its immense storage capacity. Secondly, Near-Field System III has the largest $(\Delta t_z)_{\max}$ range among the three near-field designs and a relative large NA, hence it has

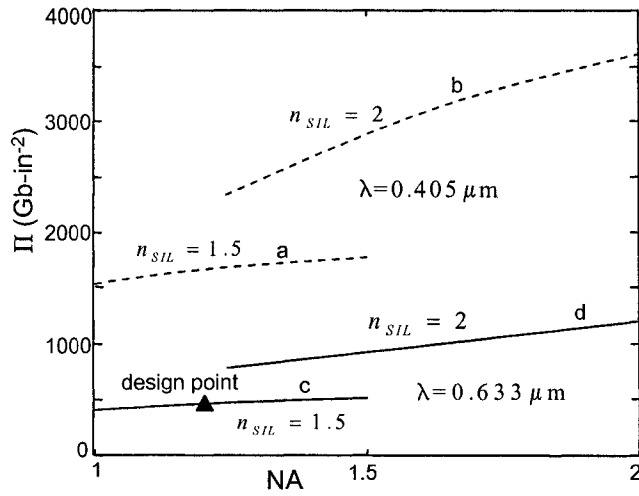


Figure 5.4 Effective surface density Π of Near-Field System III (optimum near-field system) versus NA when (a) $\lambda=0.405 \mu\text{m}$, $n=1.5$; (b) $\lambda=0.405 \mu\text{m}$, $n=2.0$; (c) $\lambda=0.633 \mu\text{m}$, $n=1.5$; (d) $\lambda=0.633 \mu\text{m}$, $n=2.0$. In the simulation, $(\Delta W_{040}|_{c^-} - \Delta W_{040}|_c)/\lambda = -5.1$, $(\Delta W_{040}|_{c^+} - \Delta W_{040}|_c)/\lambda = -2.5$. Focus range is $(\Delta t_z)_{\max} = |l_{c^+} - l_c| + |l_{c^-} - l_c|$. At the design point, $\lambda=0.633 \mu\text{m}$, $NA=1.2$ and $\Pi=470 \text{ Gb-in}^{-2}$.

the largest data capacity. Table 5.2 summarizes relationships developed in Sections 5.1 and 5.2. Π is determined as a closed-form relationship for all but Near-Field System III.

Table 5.1 Important parameters: NA, N , Π , and $(\Delta t_z)_{\max}$ for far-field system, Near-Field System I, Near-Field System II and Near-Field System III at $\lambda = 0.633\mu\text{m}$ under the assumption of low medium absorption.

Optical System	NA	N (Maximum number of layers)	$(\Delta t_z)_{\max}$ (mm)	Π (Gb-in ⁻²)
Far-field system	0.6	1233	4.20	718
Near-field System I	1	81	0.10	132
Near-field System II	1.35	39	0.026	113
Near-field System III	1.2	200	0.17	470

Table 5.2 $(\Delta t_z)_{\max}$ and effective surface density in closed form for the far-field system, Near-Field System I, Near-Field System II under the assumption of low media absorption. $(\Delta t_z)_{\max}$ and effective surface density of the Near-Field System III can only be calculated numerically. $\gamma = 1.35$ for all calculations.

Optical System	ΔW_{040} (waves)	$(\Delta t_z)_{\max}$ (mm)	Π (Gb-in ⁻²)
Far-field	$-\frac{1}{8} \left[\frac{n^2 - 1}{n^3} \right] NA^4 \Delta t$	$\frac{8(\Delta W_{040})_{\max} n^3}{(n^2 - 1) NA^4}$	$\frac{8(\Delta W_{040})_{\max} n^2}{\gamma \lambda^3 (n^2 - 1)}$
Near-field (I)	$-\frac{(n-1)}{8rn^3} NA^4 \Delta t^2$	$4 \sqrt{\frac{2rn^3 (\Delta W_{040})_{\max}}{(n-1) NA^4}}$	$\frac{NA^2}{\gamma \lambda^3} \sqrt{8 \frac{nr}{n-1} (\Delta W_{040})_{\max}}$
Near-field (II)	$-\frac{(n^2 - 1)}{8n^2} NA^4 \Delta t$	$\frac{8(\Delta W_{040})_{\max} n^2}{(n^2 - 1) NA^4}$	$\frac{8(\Delta W_{040})_{\max} \cdot n}{\gamma (n^2 - 1) \lambda^3}$
Near-field (III)	*	*	*

* by numerical solution

5.4 Effective surface density for media with significant absorption

In media with significant absorption, N is not only limited by the lens design and system aberration compensation range. Instead, it is limited by the power of the laser P_L used in the writing process, the threshold irradiance I_{th} required to write a data mark and the transmission rate τ of each layer. The laser power reaching the j^{th} layer P_j is

$$P_j = P_L \tau^j. \quad (5.11)$$

The irradiance of the laser focus spot has to exceed I_{th} . Mathematically,

$$\frac{P_j}{s^2} \geq I_{th}, \quad (5.12)$$

where $s = \frac{\lambda}{NA}$ as describe in Chapter 3. At maximum depth, $j = N$. By substitution of

Eq. (5.11) into Eq. (5.12), N is

$$N = \frac{\log_{10} \left(\frac{I_{th} s^2}{P_L} \right)}{\log_{10} \tau}. \quad (5.13)$$

Hence, the effective surface density Π is

$$\Pi = \frac{N}{s^2}. \quad (5.14)$$

By substitution of Eq. (5.13) into Eq. (5.14) and after some mathematical manipulation,

Π becomes

$$\Pi = \frac{1}{s^2 \log_{10} \tau} [\log_{10} I_{th} + 2 \log_{10} s - \log_{10} P_L]. \quad (5.15)$$

Assume $P_L = 100 \text{ mW}$, $\lambda = 0.405 \mu\text{m}$, and $I_{th} = 5 \text{ mW}/\mu\text{m}^2$, Fig. 5.5 (a) and (b) shows N and Π versus τ . The dashed and solid curves in Fig. 5.5 (a) and (b) refer to $NA = 0.6$, and 1.2 , respectively. It shows that the maximum number of layers N and the effective surface density Π increases as NA increases. For a far-field system ($NA = 0.6$), the effective surface density reaches 100 Gb-in^{-2} with an almost transparent material ($\tau = 0.95$). If the material has a moderate transmission coefficient ($\tau = 0.8$), the far-field system processes the surface density of 27 Gb-in^{-2} . On the other hand, the effective surface densities of a near-field system ($NA = 1.2$) are 570 Gb-in^{-2} and 150 Gb-in^{-2} for

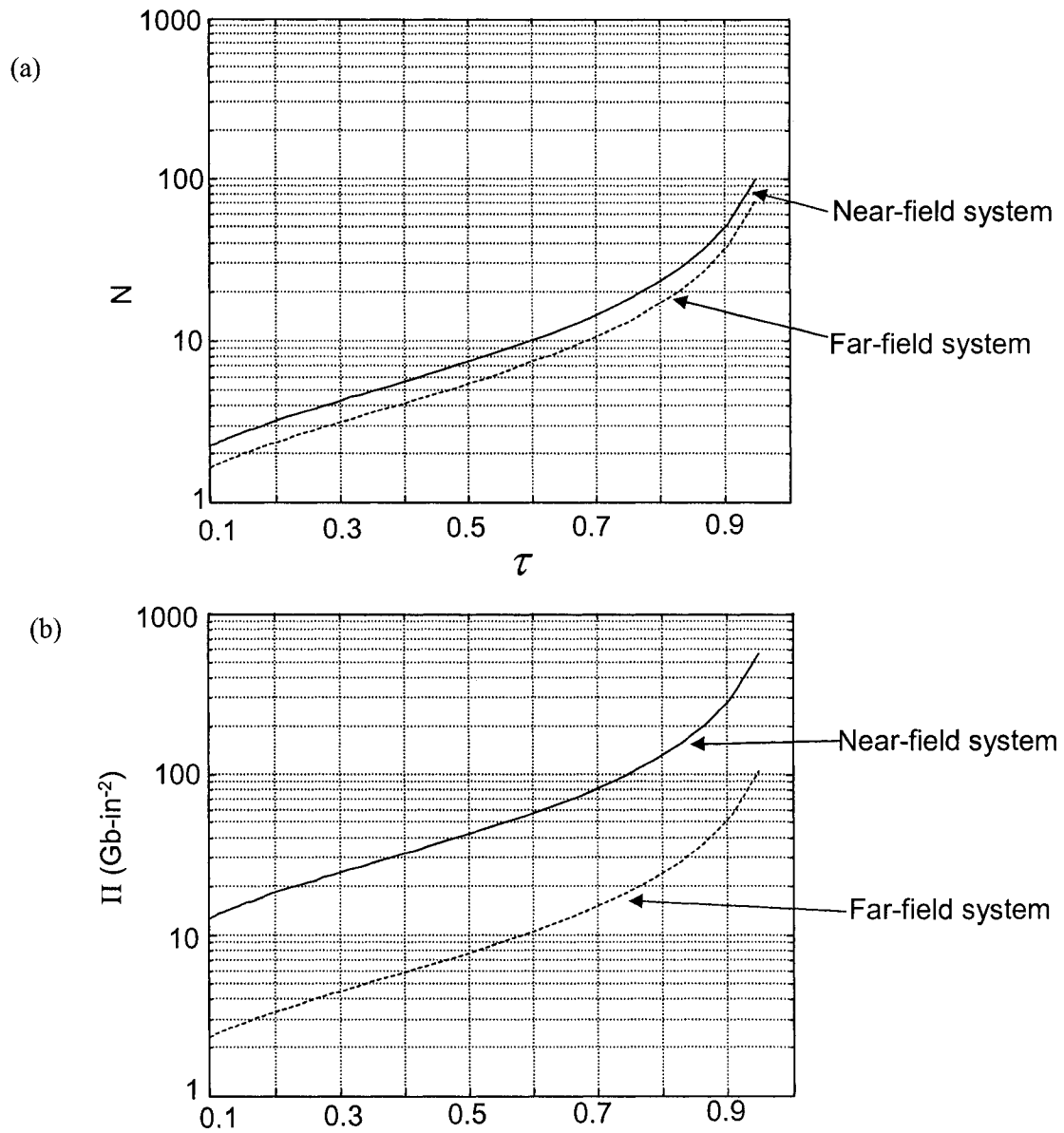


Figure 5.5 (a) N versus τ for both far-field system and near-field system at $\lambda=0.405 \mu\text{m}$; (b) Π versus τ for both far-field system and near-field system at $\lambda=0.405 \mu\text{m}$.

$\tau = 0.95$ and 0.8 , respectively. Hence, the transmission rate τ has a huge impact on the effective surface density. This calculation demonstrates that media with extremely high transmission rate are needed in the volumetric bit-wise optical data storage technology.

5.5 Summary

The maximum effective surface densities of the far-field and near-field systems are determined in terms of closed-form relationships, where possible. In the case of media with low absorption, the effective surface density Π is limited by $(\Delta t_z)_{\max}$, the maximum depth range over which spherical aberration is adequately compensated. Simulations indicate that an optimized far-field system achieves $\Pi = 718 \text{ Gb-in}^{-2}$ for a 633nm laser with over 1200 layers. Near-Field System III (optimum design) achieves 1.65 Tb-in^{-2} if a blue laser is used when $\text{NA}=1.2$ with 273 layers. Overall, the optimum near-field system promises higher effective surface density compared to the optimized far-field system, except that the compensation of ΔW_{040} is harder to achieve. Systems exhibiting over $\Pi=2 \text{ Tb-in}^{-2}$ are possible with near-field designs that incorporate blue laser, $n_{\text{SIL}} = 2.0$ and $\text{NA} \geq 1.5$. For media with significant absorption, the effective surface density is limited by P_L , I_{th} , and τ . The simulation shows that Π is increased by 3.7 times in both far-field and near-field systems if the medium transmission rate τ is increased from 0.8 to 0.95 . It also demonstrates that Π of a near-field system ($\text{NA}=1.2$) is 5.5 times higher than Π of a far-field system ($\text{NA}=0.6$).

Chapter 6

DYNAMIC TEST STAND FOR FLUORESCENT MATERIAL (ARTS-1)

This chapter presents experimental results of testing fluorescent material for a simulated space environment using a custom test stand.

6.1 Test stand description

A dynamic test stand, which is called Arizona Readout Test Stand-1 (ARTS-1), is built as a read-out system for fluorescent media. A system schematic is shown in Fig. 6.1. A diode laser with wavelength $0.638 \mu\text{m}$ is reflected 90° by a dichroic beamplate. This laser beam is then delivered through a relay telescope to a biaspheric molded glass lens mounted on a voice-coil actuator. The beam is focused into a disk sample. The disk is mounted on a miniature tip-tilt-x-y stage that aligns written data mark planes inside the disk in the focus of the biaspheric lens. The data marks inside the disk absorb energy and emit the fluorescent light, the spectrum of which ranges from $0.65 \mu\text{m}$ to $0.70 \mu\text{m}$. The dichroic beam plate combined with a high pass filter ($0.65 \mu\text{m}$ cutoff wavelength) is used to separate the reflected laser beam and the fluorescent beam. A flip mirror is used to direct the fluorescent beam into two different paths. In the first path, the fluorescent beam is focused onto a CCD camera. In the second path, a lens is used to focus the fluorescence onto a knife-edge prism, which splits the beam into two parts, A and B. Two PMTs are used to collect beams, and they are labeled PMT A and PMT B. The carrier-to-noise (CNR) is measured from the A+B signal and with a spectrum analyzer over a 500 kHz bandwidth.

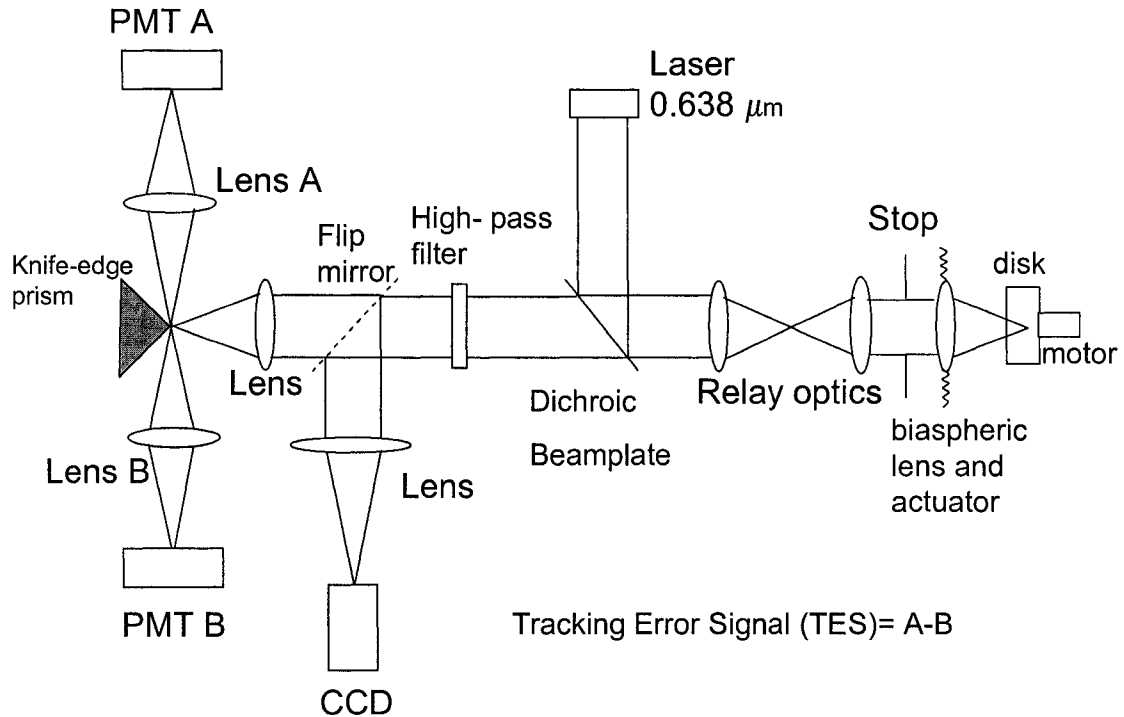


Figure 6.1 The schematic description of the Arizona Readout Test Stand 1 (ARTS-1) dynamic test stand. The optical components are mounted on a semi-kinematic rail structure. A knife-edge prism is used to split the fluorescence and the difference between the two signals is used as a track error signal (TES).

The main purpose of splitting this fluorescent beam is as a tracking servo. Careful alignment produces a tracking error signal when the laser illumination is not directly centered over the data bits. The error signal is used in a feedback control loop to correctly reposition the actuator. Because of the extreme sensitivity of the PMT, a $50 \mu\text{m}$ diameter pinhole is used to let only the fluorescence from the bits inside the disk pass through ($\nu_d = 6$). The size of the pinhole is determined by the size of the image of a data mark at

the pinhole plane. The PMT/pinhole combination is mounted on a xyz stage, which enables precise adjustment of the position of the PMT and achieves the best signal quality. Figure 6.2 is a photo of ARTS-1.

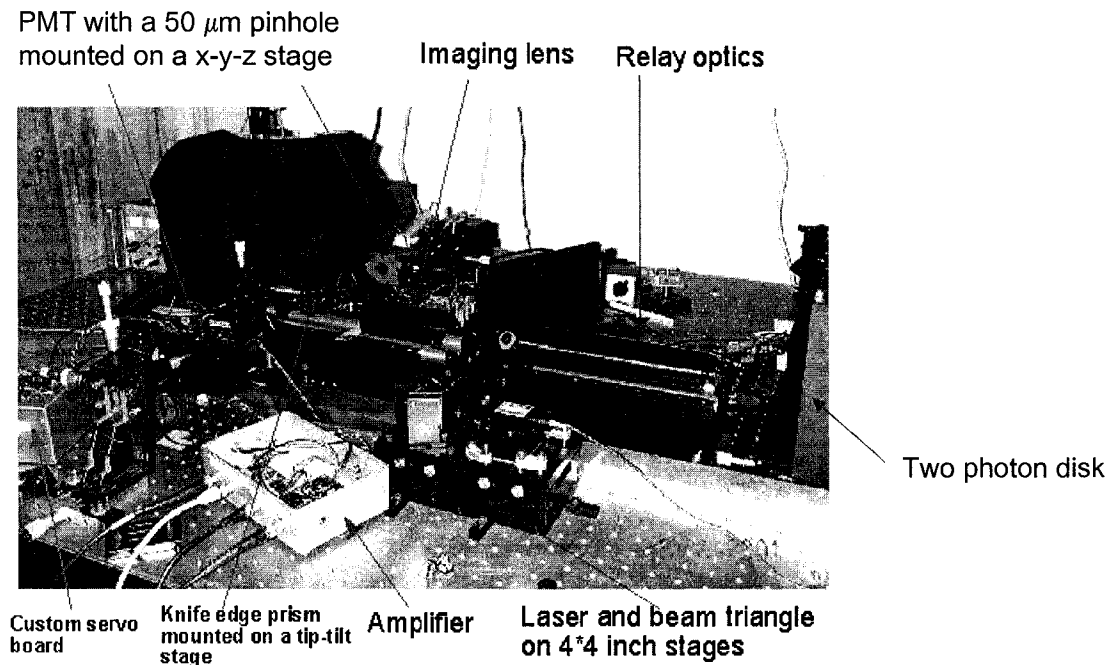


Figure 6.2 The photo of ARTS-1.

Figure 6.3 shows a read back signal from the disk displayed on an oscilloscope from a 175 kHz data pattern. The carrier-to-noise (CNR) of this signal is 37 dB and associated spectrum analyzer output is shown in Fig. 6.4. The CNR is determined by measuring the difference between signal levels at S1 and S2 in Fig. 6.4. The resolution

bandwidth of the spectrum analyzer is set to 3 KHz. The second harmonic peak is also observed in Fig. 6.4. The jitter of this signal, which is defined as the standard deviation of the lengths of all pulses in the data signal, is $1.7 \mu\text{sec}$. Since the modulated fluorescence is used as the read out signal, the primary noise component is shot noise.

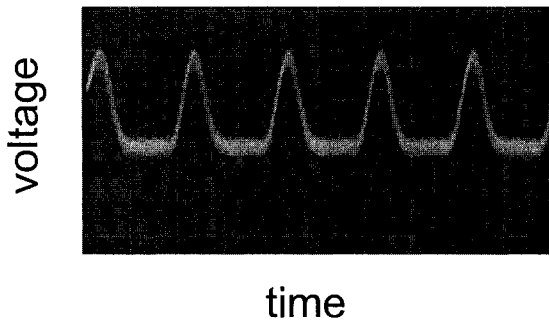


Figure 6.3 The read out signal from ARTS displayed on a oscilloscope.

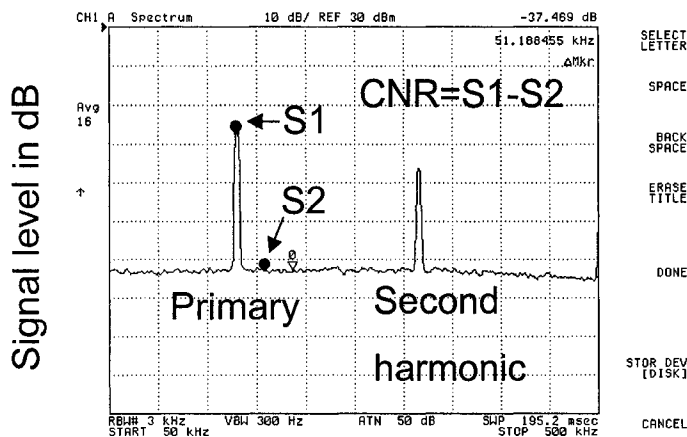


Figure 6.4 The read out signal from ARTS displayed on a spectrum analyzer. The resolution bandwidth is 3 kHz, the video bandwidth is 300 Hz and the CNR is 37 dB.

6.2 Introduction to space environment

To test the system and medium robustness in a low-orbit space environment, disk samples, which are provided by Call-Recall Inc. in San Diego, are exposed to temperature cycles and certain radiation environments defined by NASA.

The temperature in a low orbit satellite is controlled from -20°C to 50°C [Spot 4]. This medium melts in a short period when the temperature reaches 90°C . Therefore, the temperature range in this study is set to for 50°C to 90°C .

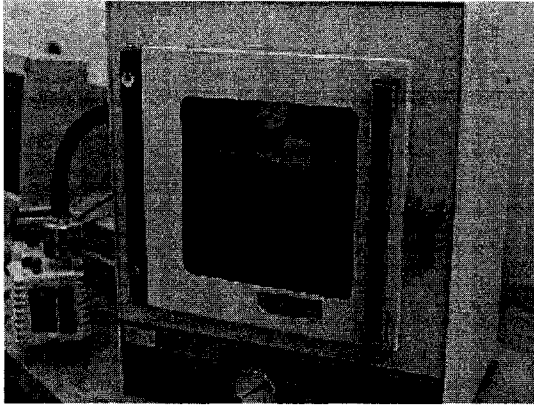
The main sources of radiation in a low-orbit satellite are from protons and electrons trapped in the Van Allen belts, heavy ions trapped in the magnetosphere, cosmic ray protons and heavy ions, and protons and heavy ions from solar flares [Barth 1997]. The energy level and the fluence of the proton and heavy ion in a low-orbit satellite suggested by NASA are 30-60 Mev, 1×10^7 - 1×10^{11} p/ cm^2 and 140-350 Mev, 1 - 2×10^7 p/ cm^2 , respectively [Miyahira, 1999].

6.3 Test results of the fluorescent medium under temperature cycles

The temperature range in this study is from 50°C to 90°C . Firstly, pre-written disk substrates are baked in the vacuum chamber shown in Fig. 6.5 for a certain amount of time at a specific temperature. After being removed from the oven and allowed to cool, readout signals are evaluated on ARTS-1. If the jitter of a disk after exposure is twice or higher than the jitter of the same disk before exposure, it is defined as a failure event. The failure rate is defined as¹

¹ Here λ is not a wavelength.

$$\lambda = \text{Sum of failures} / \sum (\text{Quantity} \times \text{Time to failure}) \frac{1}{\text{hours}}. \quad (6.1)$$



Vacuum oven

Figure 6.5 The vacuum oven used in the temperature cycle experiment.

The test results are shown in Table 6.1. The temperature dependence of the failure rate is described by the Arrhenius model [Arrhenius, 1995]

$$\lambda(T_2) = \lambda(T_1) \times \exp\left[\left(\frac{E_A}{K}\right) \times \left(\frac{1}{T_1} - \frac{1}{T_2}\right)\right], \quad (6.2)$$

where T_1 and T_2 are two temperatures that disks are exposed to in the vacuum environment and k is Boltzmann's constant. E_A is the activation energy found by fitting experimental failure rates $\lambda(T_1)$ and $\lambda(T_2)$ in Eq.(6.2).

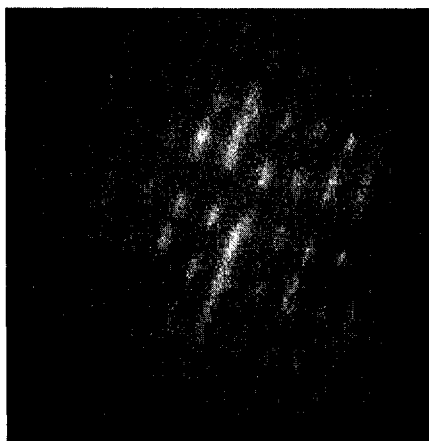
Table 6.1 The percentage of disks failed versus temperature and heating period

Temperature	50	60	60	70	70	70	70	80	80	80	90
(C)											
Heating	16	1	2	0.5	1	1.5	2	0.5	1	1.5	0.3
time (hours)											
Number of	2	3	2	2	3	10	2	2	10	2	2
disks heated											
Failure rate	0%	0%	0%	0%	0%	40%	100%	0%	70%	100%	100%

A critical temperature envelope of 1.5 hours at 70C and 1.0 hour at 80C exhibited 40% and 70% disk failures, respectively. E_A determined from these results is 0.5 eV. The long term failure rate at 50° C and a 3 year mission is expected to be unacceptably high at 21%.

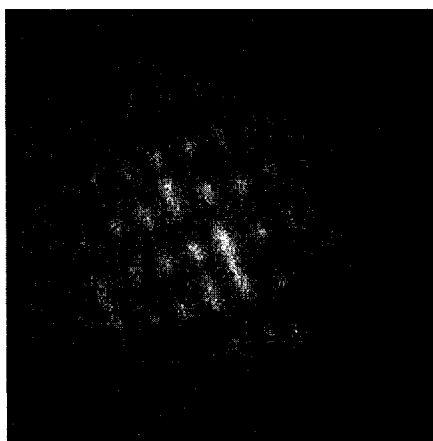
Interestingly, disk failure is not due to intrinsic photochromic damage. For example, Fig. 6.6(a) shows a CCD image of data marks inside the disk before heating, and Fig. 6.6(b) shows a typical image of marks inside the disk after heating. There is no visible degradation of fluorescence between Figs. 6.6(a) and 6.6(b). Instead, the disk failure is caused by a servo error.

a)



Before heating

b)



After heating

Figure 6.6 (a) CCD image of fluorescent bits before heating. (b) CCD image of fluorescent bits after heating. No apparent change is observed compared to (a).

Figure 6.7(a) shows the time-domain readout signal before heating, which exhibits a straight baseline and large signal amplitude. Figure 6.7(b) shows the time-

domain readout signal after heating, which exhibits a strongly curved baseline without a significant reduction in signal amplitude. Disk readout failure occurs when the servo circuit becomes unstable and unable to lock track when the track error signal has a curved baseline, as shown in Fig. 6.7(b). ARTS-1 is not able to follow the data track of the exposed disk sufficiently well. CCD images in Fig. 6.6 and signal amplitudes in Fig. 6.7 indicate that the intrinsic photochromic properties of the medium are not significantly affected in this temperature range.

In order to identify cause of the servo error, the front surface of the disk is examined with a Ronchi test [Malacara, 1992]. Figure 6.8(a) shows the front surface of the disk before heating. Ronchi lines are patterns of dark fringes covering the surface. If the surface is perfectly flat, Ronchi lines are straight and equally spaced. Magnitude of surface departure is proportional to displacement of fringes from the straight pattern. In Fig. 6.8(a), fringes are mostly straight, except near edges and near the center mounting hole. In Fig. 6.8(b), which shows the disk surface after heating, a significant distortion of the surface is apparent. The magnitude of the surface departure is estimated to be tens of microns.

We conclude that disk failure is due to a servo error caused by deformation of the molded PMMA disk substrate. The fluorescent molecules inside the disk are not damaged within the tested temperature range.

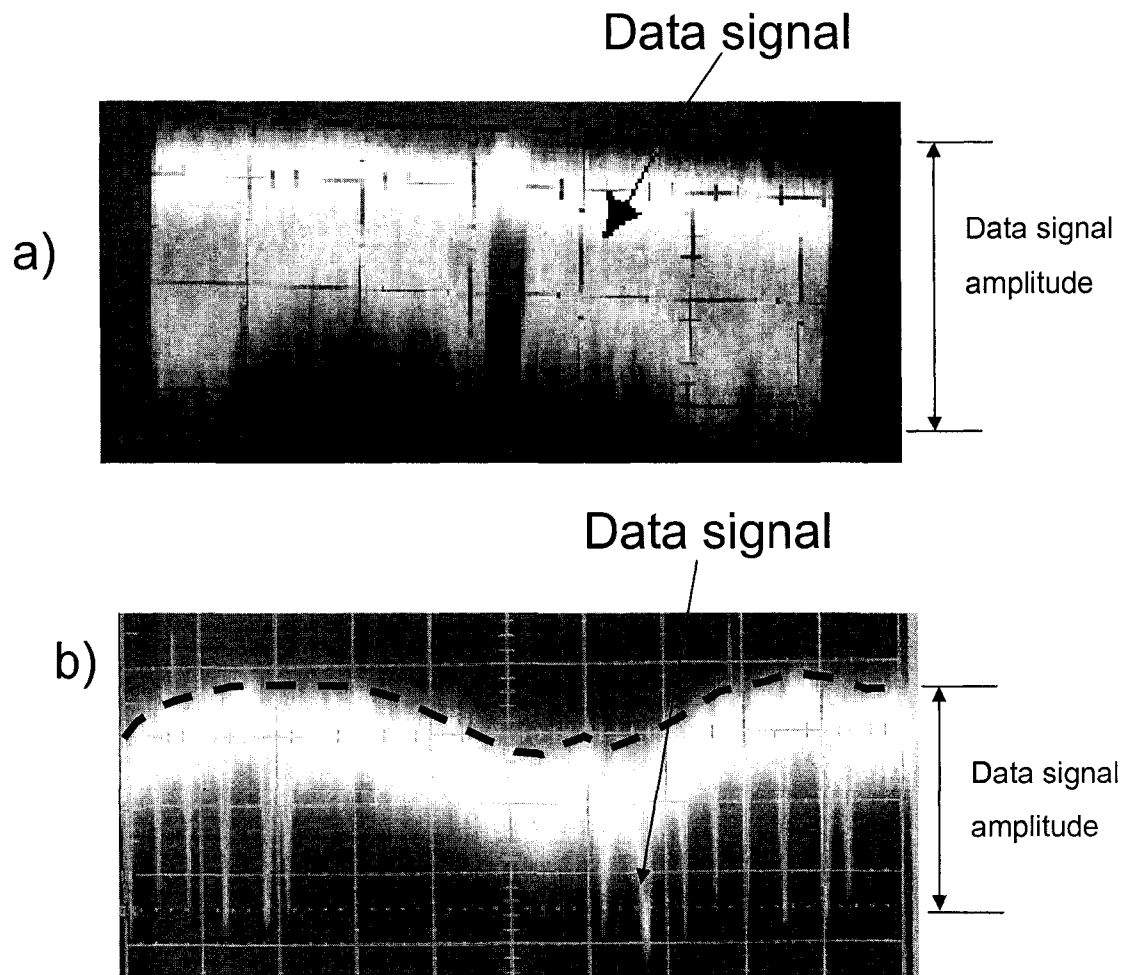
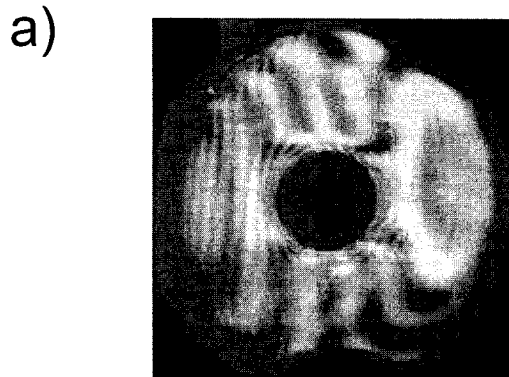
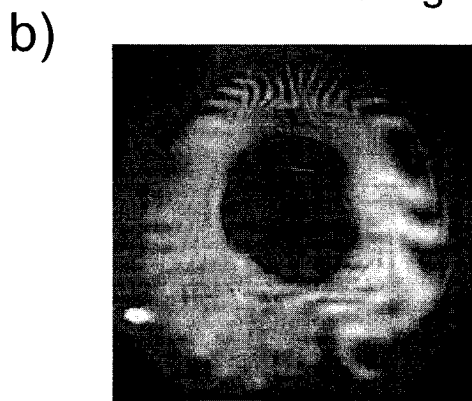


Figure 6.7 (a) Time domain readout signal before heating exhibits a straight baseline and large signal amplitude. (b) Time domain readout signal after heating exhibits a strongly curved baseline, without a significant reduction in signal amplitude.



Before heating



After heating

Figure 6.8 (a) Ronchi test interferogram of the disk front surface before heating. Straight lines indicate a relatively flat surface. (b) Ronchi test interferogram of the disk surface after heating. Complex line patterns indicate a deformed surface.

6.4 Test results of the fluorescent medium under heavy ion radiation

In this test, photo-chromic disks are exposed to six different heavy ions: I-126 (350 Mev), Br-81 (290 Mev), Ni-58 (260 Mev), Cl-35 (210 Mev), Mg-24 (170 Mev), F-19 (140 Mev). The radiation exposure is conducted under contract at Brookhaven National Lab's Tandem Van de Graaff accelerator facility. The selections of these

particles and their corresponding energy levels are based on previous research done by NASA on the topic of heavy ion radiation effects on semiconductor chips [Miyahira, 1999]. The interactions between particles and photo-chromic material are highly non-linear processes. One important characteristic to describe these interactions is penetration range, which is maximum depth that a particle can travel into the medium. Beyond this penetration range, no heavy ions are found. Simulation suggests that the penetration range of these particles in PMMA is between 45 μm and 200 μm [LETCalc, 2000]. Since the data-mark planes are 1.2 mm below the front surface of a disk, it is obvious that no heavy-ion particles reach those planes. Therefore, heavy ions have no effect on the disk performance. Table 6.2 lists the detailed experimental results.

Table 6.2 Test results of the photo-chromic disks after they are exposed to heavy ion radiation.

Particles	Flux (p/cm ² -s)	Fluence (p/cm ²)	Total dose (krad)	Incident Angle	Energy (Mev)	Range (μm)	Failure rate
I-127	1.5×10^5	2×10^7	224	0°,45°	350	48.62	0%
Br-81	2.5×10^4	5×10^6	46	0°,45°	290	56.57	0%
Ni-58	3×10^4	1×10^7	83	0°,45°	260	64.41	0%
Cl-35	1×10^5	2×10^7	134	0°,45°	210	102.8	0%
Mg-24	2×10^5	2×10^7	109	0°,45°	170	149.2	0%
F-19	1.2×10^5	2×10^7	90	0°,45°	140	200.8	0%

6.5 Test results of the fluorescent medium under proton radiation

Twenty-four disks are tested after exposure to 30 Mev and 60 Mev proton radiation. Radiation flux is 10^6 p/cm²-s and 10^9 p/cm²-s, and the total radiation period is 10 s, 50 s and 100 s. The radiation is conducted under contract at UC Davis Crocker Nuclear Laboratory. The selections of energy levels and radiation fluxes are based on previous research done by NASA on the topic of proton radiation effects on semiconductor detectors and chips [Guertin, 1999]. Test results are shown in Table 6.3. This experiment shows that high radiation flux (>20,000 krad) exposes all dye molecules inside the disk, hence the information in a disk is lost. We conclude that the 30 Mev and 60 Mev proton beam at $1e9$ p/cm²-s flux rate erases data in a short amount of time. However, the krad exposure leading to destruction in these tests is much higher than what is typically tested for in space environments, with a more typical value being 1000 krad. Proper shielding material could be installed in order to prevent disk failure in a high-energy proton radiation environment, or a less sensitive storage material needs to be found. Table 6.4 is a list of metals and the minimal thickness, which is defined as the thickness of a piece of metal needed to totally block a certain amount of proton radiation, necessary to shield 60 Mev protons. Since storage devices are commonly deep inside the satellite, it is possible that the satellite itself can provide some shielding for the photochromic disk.

Table 6.3 Test results of the photo-chromic disks after they are exposed to proton radiation.

Energy (Mev)	Flux (p/ cm ² -s)	Total dose (krad)	Radiation period (s)	Failure rate
30	10 ⁶	9.6	10	0%
30	10 ⁶	48	50	0%
30	10 ⁶	96	100	0%
30	10 ⁹	9.6×10 ³	10	100%
30	10 ⁹	4.8×10 ⁴	50	100%
30	10 ⁹	9.6×10 ⁴	100	100%
60	10 ⁶	19.2	10	0%
60	10 ⁶	9.6	50	0%
60	10 ⁶	192	100	0%
60	10 ⁹	1.92×10 ⁴	10	100%
60	10 ⁹	9.6×10 ⁴	50	100%
60	10 ⁹	1.92×10 ⁵	100	100%

Table 6.4 Minimum thickness for shielding metal when the proton energy is 60 Mev.

Shield material	Minimal thickness (mm)
Al	15
Gold	3.6
Lead	6
Stainless steel	5.8
Titanium –Tungsten alloy	4.5

6.6 Summary

The play-back performance of disks made of the fluorescent medium are tested after they are exposed to temperature cycles, heavy-ions and proton radiation. Results suggest that the current two-photon disk is not an ideal candidate for data storage on a low-orbit satellite because of the unacceptably high long-term failure rate at 50°C. An improved servo system and temperature-tolerant substrates are required to improve performance at high temperatures. Heavy ion radiation has no effect on the disk performance, due to poor penetration range. Protons with high flux (10^9 p/cm²-s) erase the bits inside a disk in a short amount of time, while protons with relatively low flux (10^6 p/cm²-s) have no effect on the disk.

Chapter 7

DYNAMIC TEST STAND FOR SUPER-RENS MATERIAL (ARTS-2)

This chapter presents the experimental results of testing Super-Rens material with a custom test stand.

7.1 Test stand description

A new dynamic test stand (Arizona Readout Test Stand 2 – ARTS-2), in which the spinning part is the objective lens, is built to test the the coupon sample made of Super-Rens material. Instead of spinning as in a conventional test stand, the coupon sample remains static in ARTS-2. A unique engineering challenge surfaces with this special arrangement of the objective lens and coupon sample. An actuator can't function normally if it is mounted on a fast-rotating spindle. To overcome this difficulty, a “passive” focus servo technique is developed, in which the focused servo is achieved by a pair of aspheric lenses. Figure 7.1 shows this test stand setup, which is designed to perform both writing and reading on coupon samples. The laser wavelength is $0.65 \mu\text{m}$, although other lasers are easily incorporated. The collimated linear-polarized laser beam first passes through a polarizing beam splitter (PBS) and relay telescope 1, which is made of two 100mm focal length achromatic lenses. Relay telescope 2 is made of two aspheric lenses, one of which is mounted on an actuator, so that it has the ability to move in the direction of optical axis. Since both aspheric lenses have $\text{NA}=0.6$, alignment is critical to make sure that no additional spherical aberration or coma are introduced to the system. The polarization of the beam is changed to circular after it passes through a quarter-wave

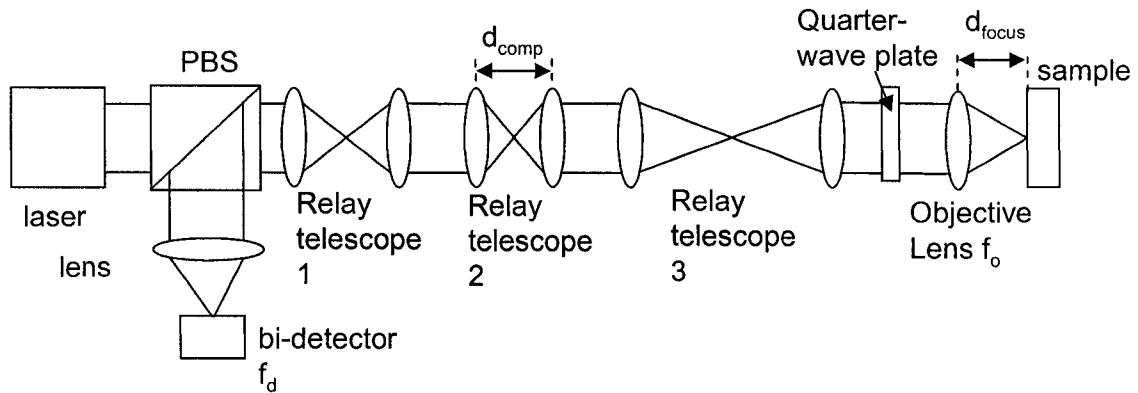


Figure 7.1 Schematic layout of the test stand.

plate. Then, relay telescope 3, which is made of two 200 mm focal length achromatic lenses, delivers the beam to a glass biaspheric lens with $NA=0.68$. This objective lens serves as system stop and focuses the laser beam onto the coupon sample. A coupon sample was first attached to a micro slide and tested on ARTS-2 in an open-loop configuration. The experimental results are presented in Section 7.2. Then, the coupon sample is mounted against the cylindrical surface of a custom designed mount, as shown in Figure 7.2 (a). The radius of the cylindrical surface R is

$$R = f_o + r, \quad (7.1)$$

where f_o is the focal length of the objective lens and r is the distance between the center of the spindle and the objective lens. Figure 7.2(b) is a picture taken while the optical head is spinning. In the reading process, the reflected laser beam from the sample is

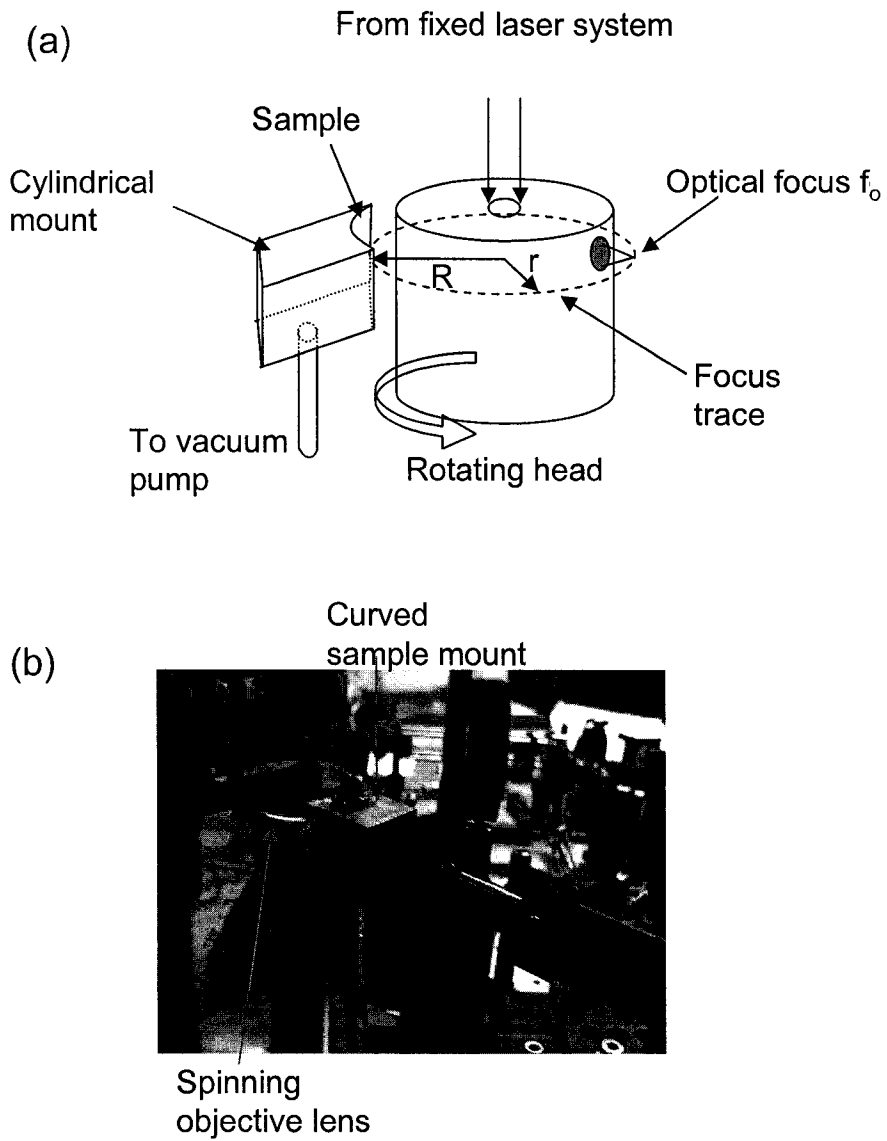


Figure 7.2 (a) Schematic diagram of the combination of the rotating head and the coupon sample; (b) Picture taken in the experiment about the rotating head and coupon sample mount.

focused by a detector lens $f_d = 150\text{ mm}$, as shown in Fig. 7.1. The distance between the detector, which is a bi-detector, and the lens is $L=122\text{ mm}$, as shown in Fig. 7.3.

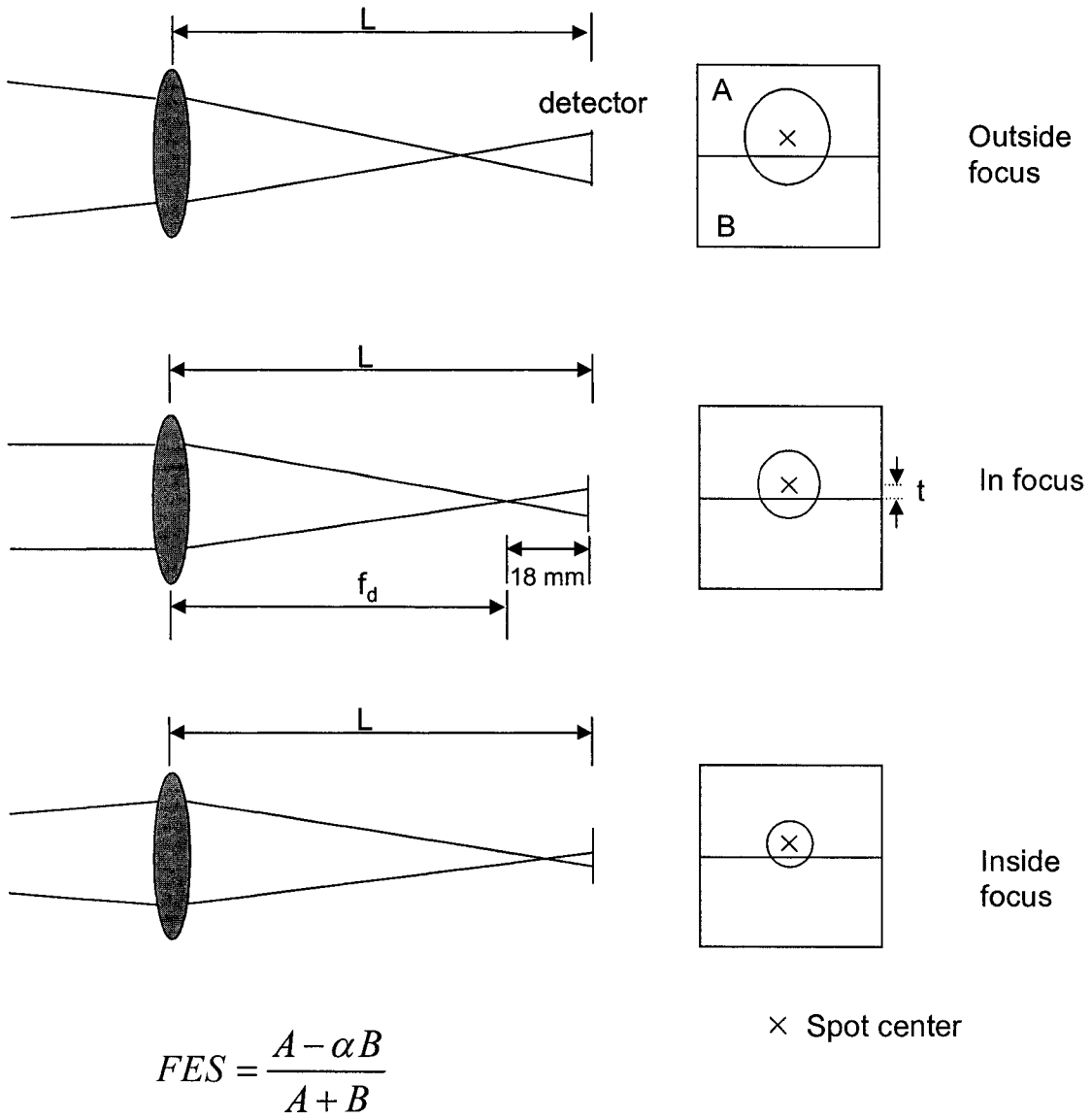


Figure 7.3 Spot sizes on the detector varies at various focus position.

As the optical head spins, the distance between the objective lens and the sample varies due to the non-uniformity and geometry of the sample, which leads to defocus

introduced to the reflected beam. A custom circuit is designed to provide closed-loop control for compensation of this defocus. The circuit, combined with a Wax-Wane focus sensor, is modeled after a system described by Wang [Wang *et al.* 1993]. The focus servo signal FES is

$$FES = \frac{A - \alpha B}{A + B}, \quad (7.2)$$

where α equals to 2. At best focus, where the sample is in the center of the objective lens depth-of-focus, the detector is placed approximately 28 mm from the focus of the detector lens. Detector offset t is adjusted so that $FES = 0$ when the objective lens is in focus. If the sample is out of focus in the direction away from the objective lens, the focus spot becomes larger and leads to a positive FES signal. The focus spots shrinks when the sample is inside focus toward the objective lens, which leads to a negative FES signal. A custom electronic circuit processes the FES signal and controls the movement of the actuator accordingly. That is, the distance d_{comp} is adjusted by moving one of the lenses in relay telescope 2. The movable lens is mounted in a voice-coil actuator. A change in d_{comp} changes the conjugate on the objective lens in order to affect a shift in the axial location of the focus spot.

The Wax-Wane servo has several advantages compared to the traditional servo made of an astigmatic lens and a quad-detector. The quad-detector is mounted on a xyz tip-tilt stage, since its position is critical to the FES signal. Even tiny vibrations of the optical table can degrade the FES signal quality. Therefore, the alignment of the traditional servo is difficult and lengthy. On the other hand, the detector in the Wax-Wane servo only needs to be mounted on a one-axis stage, which leads to significant

reduction of the alignment work. The other advantage of a Wax-Wane servo is that it is not affected by the focus spot drifting as the optical head spins. The orientation of the bi-detector used in the Wax-Wane servo is parallel to the focus spot drifting direction, so that α remains a constant at any time. The traditional servo, on the other hand, can't function normally in the case of focus spot drift.

Zemax is used to analyze the focus range of this system. Table 7.1 lists d_{comp} , d_{focus} and corresponding system Strehl ratio, which suggests that a 60 μm focus range at the sample is achieved with Strehl ratio higher than 90%. The limited focus range is due to the fact that all the optical elements in this setup are the off-the-shelf products. Those elements are not optimized to achieve the best optical system performance. In the future, an optical system with custom designed lenses should be used to achieve much longer focus range.

Table 7.1: d_{comp} , d_{focus} and corresponding system Strehl ratio simulated by Zemax.

d_{comp} (mm)	d_{focus} (mm)	Δd_{focus} (mm)	Strehl ratio
5.4551	1.495	0.000	90%
5.4317	1.505	0.010	94%
5.4085	1.515	0.020	97%
5.3857	1.525	0.030	99%
5.3631	1.535	0.040	99%
5.3409	1.545	0.050	96%
5.3189	1.555	0.060	91%

7.2 Experiment results

Coupon samples with a single layer of Super-Rens material are tested on an open loop ARTS-2. Experimental results show that the minimal powers P_{\min} required to write data marks on the samples are 11 mW and 12 mW when the focus spot speed is 1 m/s at 125 KHz and 250 KHz data rates, respectively. The data mark sizes are $1\mu\text{m}\times 4\mu\text{m}$ and $1\mu\text{m}\times 2\mu\text{m}$ at 125 KHz and 250 KHz, respectively. As the focus spot speed increases to 2 m/s, P_{\min} increases to 15.5 mW at 250 KHz and 500 KHz data rate. With the further increase of the focus spot speed, P_{\min} is beyond the maximum output power of the diode laser used in ARTS-2. The threshold irradiance I_{th} at each focus speed and data rate is derived as

$$I_{th} = \frac{P_{\min}}{s} \quad , \quad (7.3)$$

where $s = \frac{\lambda}{NA}$. Hence, I_{th} equals to $9.4 \text{ mW}/\mu\text{m}^2$ at 1 m/s focus spot speed and 125 KHz.

By substituting $P_L = 100 \text{ mW}$, $\lambda = 0.650 \mu\text{m}$, $\tau = 0.78$ and $I_{th} = 9.4 \text{ mW}/\mu\text{m}^2$ into Eq. 5.13 and 5.14, the maximum number of layers possible N and the effective surface density Π with the current Super-Rens material is $N = 9$ and $\Pi = 6 \text{ Gb}/\text{in}^2$. This suggests that the storage capability of current Super-Rens material is limited by its low transmission rate τ , instead of the optical design. Figure 7.4 shows the data marks written on a coupon sample at at 1 m/s focus spot speed, 125 KHz data rate and 12 mW laser power. Table 7.2 summaries the experimental results of the coupon sample tested on the open-loop ARTS-2.

Table 7.2 Focus spot speed versus data rate versus P_{\min} and I_{th} for Super-Rens material.

Focus spot speed (m/s)	Data rate (KHz)	P_{\min} (mW)	I_{th} (mW/ μm^2)
1	250	12	10.2
	125	11	9.4
2	500	15.5	13.2
	250	15.5	13.2
3	750	*	
	375	*	
4	1000	*	
	500	*	

* beyond the maximum output power of the laser used in this test stand

Great efforts have been invested to finish implementing the Wax-Wane servo in ARTS-2 and achieving a solid focus lock as the objective lens scanning through the Super-Rens material mounted on the curved surface of a coupon-sample holder. However, focus is only locked along a relatively short distance on the sample, where the objective lens scans 1 mm across the material at 0.4 m/s. This partial focus lock difficulty is due to two reasons. The first reason is that the optical path is too long and too many optical components are used in ARTS-2. These components introduce too many uncertain

factors into the system, such as low frequency vibration. To overcome this difficulty, a new test stand needs to be designed so that the optical path is shortened and much fewer optical components are involved. The second reason is that all the lenses in ARTS-2 are the off-shelf components, which leads to the short compensation range. Therefore, one or two custom designed lenses need to be used so that a much longer compensation range is achieved.

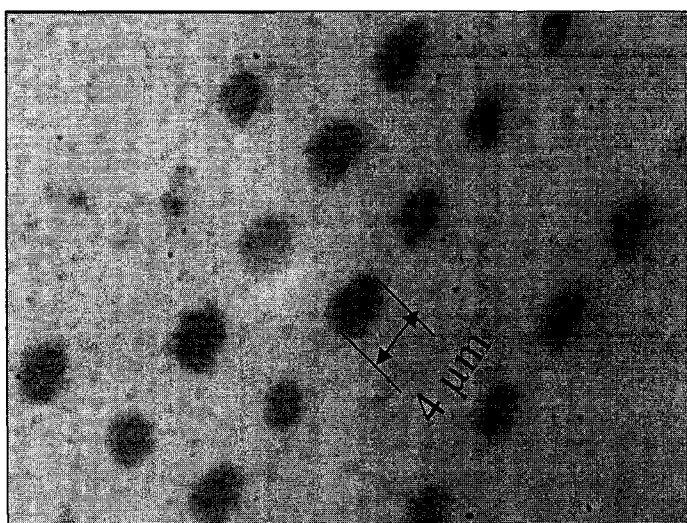


Figure 7.4 Data marks written on a coupon sample made from Super-Rens material at 1 m/s focus spot speed, 125 KHz data rate and 12 mW laser power.

7.3 Summary

A new closed-loop cylinder shape media dynamic test stand is built. Conventional focus servo techniques can not be applied to this test stand because of the nature of the

spinning objective lens. A new passive focus servo technique is developed, which can provide 60 μm focus range. A single layer thin film with Super-Rens structure is tested on the test stand. Experimental results show that I_{th} at 125 KHz data rate and 1 m/s focus spot speed is $9.4 \text{ mW}/\mu\text{m}^2$, which leads to the conclusion that the maximum number of data layers N is 9 for a 100 mW laser diode. N is significant because it suggests that the maximum surface density $\Pi = 9 \text{ Gb-in}^{-2}$ of an optical data storage system using Super-Rens material is limited by the material itself instead of the limitation on the optical system design. Hence, a new Super-Rens material with higher transmission rate and non-linear coefficient needs to be developed for volumetric bit-wise optical data storage. The implementation of the Wax-Wane focus servo is a partial success. A new optical design with much shorter optical path and much fewer optical components is needed to achieve a full solid focus lock.

Chapter 8

CONCLUSIONS, SUMMARY AND FUTURE WORK

8.1 Summary

The endless desire for higher disk capacity results in developing multiple-layer optical disks. Volumetric bit-wise optical data storage technologies using fluorescent and Super-Rens materials show great potential to be the next generation optical storage techniques. This dissertation studies system and material aspects of this technology via theoretical modeling and experiments.

In the modeling, three modeling methods are used to simulate interlayer crosstalk of optical systems using fluorescent and Super-Rens materials. A spacing factor γ is defined to characterize the relationship between interlayer crosstalk level and the data layer spacing, which is found to have a universal value $\gamma = 1.3$ to suppress the crosstalk level to under -30 dB in a confocal system for both materials. Simulations also suggest that an optimum design point for the detector size is $v_d = 3.5$ and $\gamma = 1.66$, where the inter-layer crosstalk is below -30 dB and the penalty on the CNR is about 1 dB compared to the CNR from a non-confocal system.

Far-field and near-field optical systems are designed for volumetric bit-wise optical storage technology. In the far-field system, a combination of a Galilean telescope spherical aberration compensator and a customized far-field aspherical objective lens achieves 4.2 mm compensation range in the recording material with Strehl ratio higher than 90%, which corresponds to 36 waves of spherical aberration. This far-field system has the potential to achieve $\Pi = 718 \text{ Gb-in}^{-2}$ for $0.633 \mu\text{m}$ laser with over 1200 layers. A

optimum near field system using a SIL designed around point C in Fig. 4.4. This optimum near-field system achieves 1.65 Tb-in^{-2} if a blue laser is used when NA is 1.2 and the number of data layers N is 273. Simulation suggests that the optimum near-field system promises higher effective surface storage density compared to far-field systems, except that the compensation of ΔW_{040} is harder to achieve. Systems exhibiting over $\Pi=2 \text{ Tb-in}^{-2}$ are also possible with near-field designs that incorporate blue laser, $n_{SIL} = 2.0$ and $\text{NA} \geq 1.5$.

The playback performance of fluorescent media are tested on a dynamic test stand (ARTS-1) after they are exposed to a simulated space environment. Results show that the current fluorescent medium is not an ideal candidate for data storage on a low-orbit satellite due to its unacceptably high long-term failure rate at 50°C . An improved servo system and temperature-tolerant substrates are required to improve performance at high temperatures. Heavy ion radiation has no effect on the disk performance, due to poor penetration range. Protons with high flux ($10^9 \text{ p/cm}^2\text{-s}$) erase the bits inside a disk in a short amount of time, while protons with relatively low flux ($10^6 \text{ p/cm}^2\text{-s}$) have no effect on the disk.

Super-Rens material is tested on a closed-loop dynamic test stand (ARTS-2), with a new passive focus servo technique. This passive servo provides $60 \mu\text{m}$ focus range. Experimental results show that the minimal power required for 125 KHz data rate at 1m/s is 11 mW, which leads to the conclusion that the maximum number of data layers N is 9 for a high power laser diode $P_{laser} = 100\text{mw}$ used in a DVD-RW.

Overall, the answer to the fundamental question “*How much data storage capacity can a volumetric storage system have?*” is that it depends on the storage medium. For the fluorescent medium, it is the maximum focus range Δt_z that limits Π . Hence, the maximum surface densities of the custom designed far-field and near-field system that use fluorescent material are 718 Gb-in^{-2} and 470 Gb-in^{-2} , respectively. For the Super-Rens material, it is the transmission rate τ that limits Π . Therefore, the maximum surface densities of the custom designed far-field and near-field system that use current Super-Rens material are 6 Gb-in^{-2} and 23.5 Gb-in^{-2} , respectively.

8.2 Future work

Additional works are required to improve the performance of a volumetric bit-wise optical data storage device in both system and material aspects. Suggestions for future work include:

- 1) Continue developing a robust servo for the fluorescent medium. Since the dynamic test on the fluorescent material shows that the disk failure in a space environment is due the failure of the servo, a more robust servo is needed. One promising solution is the master-slave servo concept, which has demonstrated great potential to servo an optical disk with hundreds of data layers.
- 2) Develop next generation Super-Rens material. It is clear that the transmission rate and non-linear coefficient of current Super-Rens

material limits the maximum surface density. The next generation Super-Rens material should have transmission rate higher than 95%.

- 3) Continue developing the passive focus and tracking servo. The current passive focus servo on ARTS-2 has a small compensation range, which is not sufficient. The next generation passive focus servo should use customized optical components, so that a much larger compensation range in a much compact system is achieved. On the other hand, the wavelength domain tracking servo concept [Choi *et al.* 2004] has shown great potential to be an excellent passive tracking servo technique.

REFERENCES

Arrhenius model and the failure rate, http://www.vishay.com/docs/rect_reliabilty.pdf

Barth, J., "Ionizing Radiation Environment Concerns" conference of Single Event Effect Criticality Analysis, <http://radhome.gsfc.nasa.gov/radhome/papers/seeca3.htm>

Chen, F. S., Lamacchia, J. T., and Fraser D. B., "Holographic storage in lithium niobate," *Appl. Phys. Lett.* 13, 223-225 (1968).

Choi, T., and Milster, T. D., "Wavelength-domain tracking in multiple-beam optical storage systems" ODS 2004, California, USA.

Dereniak, E. L., and Boreman, G. D., "Infrared detectors and systems" Wiley Series in Pure and Applied Optics, Wiley, John and Sons, Inc. 1996.

Fuji, H., Tominaga, J., Men, L., Nakano, T., Katayama, H., and Atoda, N., "A near-field recording and readout technology using a metallic probe in an optical disk," *Jpn. J. Appl. Phys.*, Part 1, 39, pp. 980-981 2000.

Gabor, D., 1948, "A new microscopic principle," *Nature*, 161, 777-778.

Gauderon, R., and Sheppard, J. R., "Effect of a finite-size pinhole on noise performance in single-, two-, and three-photon confocal fluorescence microscopy" *Applied Optics* Vol 38 No. 16 June 1 pp. 3562-3565, 1999.

Gu, M., Sheppard, C., and Gan, X., "Image formation in a fiber-optical confocal scanning microscope," *J. Opt. Soc. Am. A.* Vol. 8, No. 11, Nov. 1991, pp. 1755-1761.

Guertin, S., "Single-Event Upset Test Results for the Xilinx XQ1701L PROM," 1999 IEEE Radiation Effects Data Workshop, pp. 14-21.

http://radnet.jpl.nasa.gov/reports/1/ReportFiles/Xilinx_R1701L.pdf

Haskal, H. M., "Laser recording with truncated Gaussian beam," *Appl. Opt.* 18, 2143-2146 (1979)

REFERENCES-*Continued*

Heanue J. F., Bashaw M. C., and Hesselink L., "Volume holographic storage and retrieval of digital data," *Science* 265 (5173), pp. 749-752, 1994.

Hisaka, M., Ishitobi, H., and Kawata, S., "Optical recording of reversed domains in a Ce-doped SBN:75 crystal for bit-oriented three-dimensional optical memory," *Journal of the Optical Society of America B* 17 (3) pp. 422-426 2000.

Ishikawa, M., Kawata, Y., Egami, C., Sugihara, O., and Okamoto, N., "Reflection-type confocal readout for multilayered optical memory," *Optics Letters*, Vol. 23, No. 22, pp. 1781-1783, 1998.

Kawata, Y., Ueki, H., Hashimoto, Y., and Kawata, S., "Three-dimensional optical memory with a photorefractive crystal," *Appl. Opt.* Vol. 34, No. 20 pp. 4105-4109, 1995

Kikukawa, T., Tachibana, A., Fuji, H., and Tominaga, J., "Recording and readout mechanisms of Super-Resolution Near-Field Structure disk with silver-oxide layer", *Jpn. J. Appl. Phys.* 42 No. 2B, (2003).

LETCalc can be found in <http://tvdg10.phy.bnl.gov/LETCalc.html>, 2000.

Malacara, D., "Optical Shop Testing" Wiley series in pure and applied optics, 2nd edition, 1992

Mansfield, S. M., and Kino, G. S., "Solid immersion microscope," *Appl. Phys. Lett.*, vol. 57, no. 24, pp. 2615-2616, 1990

McCormick, F. B., Zhang, H., Dvornikov, A. S., Walker, E., Chapman, C., Kim, N., Costa, J., Esener, S. C., and Rentzepis, P. M., "Parallel access 3D multilayer optical storage using 2-photon recording" *Proc. SPIE* Vol 3802, pp. 173-182 2000.

Miller, T., Butz, J., and Milster, T. D., "Novel method for tracking in homogeneous volumetric media," *ODS 2003* pp. 187-189.

REFERENCES-Continued

Milster, T. D., J. S. Jo, and K. Hirota, "Roles of propagating and evanescent waves in solid immersion lens systems," *Appl. Opt.* 38, 5046-5057 (1999)

Milster, T. D., Upton, R. S., and Luo, H., "Objective lens design for multiple-layer optical data storage," *Optical Engineering* 38(2) p. 295-300, 1999.

Milster T. D., Zhang, Y., Butz, J., Miller, T., and Walker, E. P., "Volumetric Bit-Wise Memories" Proceedings of the NASA Office of Earth Science (OES) Advanced Information Systems Technology (AIST) Program workshop on projections for future spacecraft needs, Jan 9-10, 2002, Jet Propulsion Laboratories, Pasadena, California.

Miyahira, T., "Summary of SEE test results from BNL heavy ion test" <http://radnet.jpl.nasa.gov/reports/1/ReportFiles/9902bnl.PDF>, 1999

Mizuno, T., Hitosugi, T., Kojima, N., and Watanabe, K., "An optical flying head for a near-field recording system," *ODS 2001*, pp. 268-270.

Olkkonen, J., Kataja, K., Aikio, J., and Howe, D. G., "Study of high throughput aperture for near field optical data storage," *ODS 2003*, pp. 126-128.

Orlov, S. S., and Hesselink, L., "Holographic shift multiplexing in thin volumetric media," *J. Opt. Soc. Am. B*, Vol. 20, No. 9, pp. 1912-1927, 2003.

Parthenopoulos, D. A., and Rentzepis, P. M., "Three-dimensional optical storage memory," *Science* 245 (0), pp. 843-845, 1989.

Rakuljic, G. A., Leyva, V., and Yariv, A., "Optical data storage by using orthogonal wavelength-multiplexed volume holograms," *Optics Letters*, Vol. 17, No. 20 pp. 1471-1473, 1992.

Sheppard, J. R., and Cogswell, C. J., "Confocal microscopy with detector arrays" *Journal of Modern Optics*, 1990, vol 37 No2 267-279.

REFERENCES-Continued

Spot 4 satellite thermal control, http://spot4.cnes.fr/spot4_gb/thermic.htm.

Strickler J. H., and Webb, W. W., "3-D optical data storage by two-photon point excitation," *Advanced Materials* 5 (6) pp. 479-481, 1993.

Suzuki, M. A., Hashida, T., Hibino, J., and Kishimoto Y., "Multiple optical memory using photochromic spiropyran aggregates," *Molecular Crystals and Liquid Crystals* 246 pp. 389-396 1994.

Taflove, A., and Hagness, S., "Computational electrodynamics," Artech house publishers, 2000.

Terris, B. D., H. J. Mamin, D. Rugar, W. R. Studenmund, and G. S. Kino, "Near-field optical data storage using a solid immersion lens," *Appl. Phys. Lett.* 65, 388-390 (1994).

Tieke, B, M.Dekker, N. Pfeffer, R. van Woudenberg, G. Zhou, and I. Ubbens, "High data-rate phase-change media for the digital video recording system," in *Proc. SPIE joint Int. Symp. Optical Memory and Optical Data Storage*, 3864, 200-202 (1999).

Tominaga, J., Nakano, T., and Atoda, N., "An approach for recording and readout beyond the diffraction limit with an Sb thin film," *Appl. Phys. Lett.* 73, 2078 (1998).

Toriumi, A., Kawata, S., and Gu., M., "Reflection confocal microscope readout system for three dimensional photochromic optical data storage," *Optics letters*, 23(24), pp. 1924-1926, 1998.

Upton, R. S., and Milster, T. D., "Detector patterns from optical disks" *Optical Engineering*, vol 40 No 6 June 2001 pp. 1030-1044

Walker, E. P., Zheng, X., McCormick, F. B., Zhang, H., Kim, N., Costa, J., and Dvornikov, A. S., "Servo error signal generation for 2-photon recorded monolithic multilayer optical data storage," *SPIE Proc.* 4090 pp. 179-183 (2000).

REFERENCES-Continued

Walker, E. P., Feng, W., Zheng, Y., Zhang, H., McCormick, F. B., and Esener, S., "3-D parallel readout in a 3-D multilayer optical data storage system," ODS 2002, pp. 147-149.

Wang, M. and Milster, T. D., "Crosstalk cancellation using differential Wax-Wane focus servo technique," Jpn. J. Appl. Phys. Vol. 32 1993 pp. 5277-5283.

Wang, W. W., Esener, S. C., McCormick, F. B., Cokgor, I., Dvornikov, A. S., and Rentzepis, P. M., "Experimental characterization of two-photon memory," Optics Letters, Vol. 22, No. 8, pp. 558-560, 1997.

Wilson, T., Kawata, Y., and Kawata, S., "Readout of three dimensional optical memories," Optics Letters, Vol. 21, No. 13, 1003-1005, 1996.

Wu, F. H., Shieh, H., "Thermochromism of silver oxide for optical switching layers in volumetric optical disks," Japanese Journal of Applied Physics, Part 1, Feb. 2003, 42(2B), pp. 820-823.

Wu, F. H., Rambabu, U., Milster, T. D., and Shieh, H., "Optical nonlinearity of silver oxide super resolution structure as a function of oxygen content," ODS 2003, pp.27-29.

Wu, F. H., Milster, T. D., and Shieh, H., "Write-once multilayer optical disk using transparent recordable material with an optical switching layer," ISOM 2003 pp. 274-275.

Zhang H., Walker E. P., Feng W., Zhang Y., Dvornikov A. S., Esener S. and Rentzepis P. M., "Multi-layer optical data storage based on two-photon recordable fluorescent disk media," Eighteenth IEEE Symposium on Mass Storage System, 2000 pp 225-236 (2000)

Zhang, Y., Dvornikov, A., Taketomi, Y., Walker, E., Rentzepis, P., Esener, S., "Towards ultra high density multi-layer disk recording by two-photon absorption," SPIE Proc. vol. 5362 pp. 170-180, 2004.